A Microfabricated Liquid Mixer for Biomedical Applications

by

Joel Voldman

B.S. Electrical Engineering
University of Massachusetts at Amherst, 1995

Submitted to the Department of Electrical Engineering and Computer Science in partial fulfillment of the requirements for the degree of

Master of Science in Electrical Engineering
at the
MASSACHUSETTS INSTITUTE OF TECHNOLOGY

June 1997

Author ____
Department of Electrical Engineering and Computer Science
May 22, 1997

Certified by ____
Martin A. Schmidt
Associate Professor
Thesis Supervisor

Certified by ____
Martha L. Gray
J. W. Kieckhefer Associate Professor of Electrical Engineering
Thesis Supervisor

Accepted by ____
Arthur C. Smith
Chairman, Department Committee on Graduate Students

A Microfabricated Liquid Mixer for Biomedical Applications

by

Joel Voldman

Submitted to the Department of Electrical Engineering and Computer Science on May 22,
1997 in partial fulfillment of the requirements for the degree of
Master of Science in Electrical Engineering

Abstract

As the biomedical and biological sciences continue to merge with micromachining, interesting applications result. One area of continuing interest is in the area of automating sample preparation before running assays. A micromachined sample preparation system would offer many advantages unrealizable in macroscopic systems. To this end, a microfabricated liquid mixer is described which would be used for sample preparation for the biomedical industry. The liquid mixer consists of a cantilever-plate flapper valve defined in a silicon wafer. This wafer also includes port holes to allow fluid access. This silicon wafer is bonded to a glass wafer which has channels etched in it to complete the liquid mixer. The liquid mixer is capable of mixing small volumes (<microliters) of liquids in a fast, controllable manner. The design and fabrication of the liquid mixer are described, including the development of a glass-etching process. The devices are characterized in terms of their pressure-flow relationships. Mixing length studies are also undertaken using a pH sensitive fluorescent marker. The devices are shown to work and mix, although suffering from several shortcomings which can be remedied in a next design.

Thesis Supervisor: Martin A. Schmidt
Title: Associate Professor of Electrical Engineering

Thesis Supervisor: Martha L. Gray
Title: J. W. Kieckhefer Associate Professor of Electrical Engineering

Acknowledgements

Many people have helped me and given me guidance in the two years that I have been at MIT. Of special importance are my advisors, Marty and Martha. To Marty I owe much thanks for guiding me and pushing me along in the directions that I needed to go, often without my knowing. Martha I thank for giving me an understanding of the right questions to ask and the right problems to solve.

I owe much to my research group, who have been full of ideas and knowledge. They have been an invaluable resource both when I needed information and when I needed to vent. Specifically, I must thank my office mates, who've had to endure with my mannerisms and interesting noises: Lalitha, to whom thanks is quite an understatement, Roberto, for frightening me with his last month, and Albert, for getting me to appreciate Catalan (not Catalonian). Then there's Samara, who has been with me from the start here at MIT, going through the same classes and crunches. I'd like to thank Mark, both for his "interesting" political and scientific views and for giving me an understanding of the complexity of problems. And then there's the rest of the crew: Aravind, Errol, Ravi (who never gets stressed out), Jo-Ey, CC (who definitely works too hard), Arturo, Charles, and Reza.

Outside the group, I would like to thank the people at the Shriners Burns Institute for letting me use their microscopy facilities, especially Martin Yarmush, Mehmet Toner, Octo, and Sangeeta. A special thanks goes to Will, who answered all my annoying microscopy questions time and again. I would also like to thank the MTL staff, who helped me get through my processing, especially Tom Takacs for the CMP work (and the legal advice).

I would also like to thank the National Science Foundation for my Graduate Research Fellowship and for the Presidential Young Investigator award, both of which funded this research.

Finally, I would like to thank my parents and family for giving me support forever, and my friends for helping get through the stressful times. And I would like to thank Jenny for helping me get through the last few months.

Contents

List of Figures

List of Tables

Chapter 1

Introduction

In recent years, the intersection of micromachining and the biological and biomedical sciences has netted several powerful and enabling technologies. In retrospect, this seems natural as the two fields deal with many of the same physical scales. Applications as diverse as micromachined pressure sensors for blood pressure measurement [1], micromachined sensors for measurement of extracellular pH [2], and integrated chambers for polymerase chain reaction [3] span the full range of the medical, biological, and biochemical sciences.

As the intersection between the two disciplines matures, there is a growing need to deepen the level of interaction in order to develop more complex, but also more enabling, technologies. Areas now being researched include microfabricated analysis systems and the sample preparation that accompanies. This thesis reports on a device to be used for sample preparation in the biomedical sciences. Such a device may be a valuable addition to the field.

1.1 Sample Preparation

In biology and medicine, researchers and clinicians perform millions of tests (assays) annually. An important step prior to performing any assay is to prepare the samples which will be used in the assay. This action is called sample preparation and is vital to the biological and biomedical industries.

Many assays involve the use of cells or cellular constituents (RNA, DNA, small cellular molecules, etc.). For these cellular assays, sample preparation often consists of one or more of the following steps, explained below and in Figure 1-1.

Lysing - disintegrating the sample (cells) into its constituent components
Staining - selectively marking sections of the sample
Diluting - reducing the concentration of the sample

Incubation - increasing or decreasing reaction times according to temperature

Centrifugation - sorting the sample by density

Three of the five steps outlined above - lysing, staining, diluting - involve mixing one liquid with another. Since many assays involve one or more of these mixing steps, and since many assays involve repeated preparation sequences, it is evident that mixing liquids together is prevalent in sample preparation.

Conventionally, mixing two liquids for sample preparation is performed manually. This means that preparers pipette liquid A into liquid B and repeat the process several times with different liquids to prepare the sample. This has several drawbacks. First, unless the preparers use highly sophisticated instruments, they often need to use relatively large total volumes (>100 µl). This volume is often larger than that needed for a deterministic assay which increases assay cost because reagents can be quite expensive. Second, preparers (humans) introduce time and volume variability into the process. These variations add more unknowns to an already complex biological system. Third, sample preparation can often take a long time (> 30 min), consuming valuable person-hours and diverting researchers and clinicians away from analysis. Lastly, manual preparation necessarily introduces a time lag between sample preparation and sample analysis. Since there are instances when the kinetics of a reaction are important, being able to prepare and analyze samples on a small and repeatable timescale would give valuable information.

In order to address these problems, several companies have successfully built apparatus to automate sample preparation. These commercial solutions usually use robotics workstations that micropipette given volumes of two liquids into sample wells. This approach suffers from three disadvantages. First, the robotics workstations are expensive. Second, the minimum liquid handling volume is approximately 1 µl. Third, there is still a time lag between preparation and analysis.

Microfabrication has the potential to address the problems with manual sample preparation while not succumbing to the problems that robotic autosamplers suffer from. With microfabrication it is: one, easy to work with small volumes (< µl), due to the accuracy with which small structures can be built. This reduces sample and reagent consumption, which is a major cost in running assays. Two, microfabrication can take advantage of mass production to produce many units with small inter-unit variability. This reduces assay variability and cost. Three, a microfabricated sample preparation system can be attached to (or fabricated with) a sample analysis system, thus reducing (and controlling) the lag time between preparation and analysis, enabling kinetic assays.

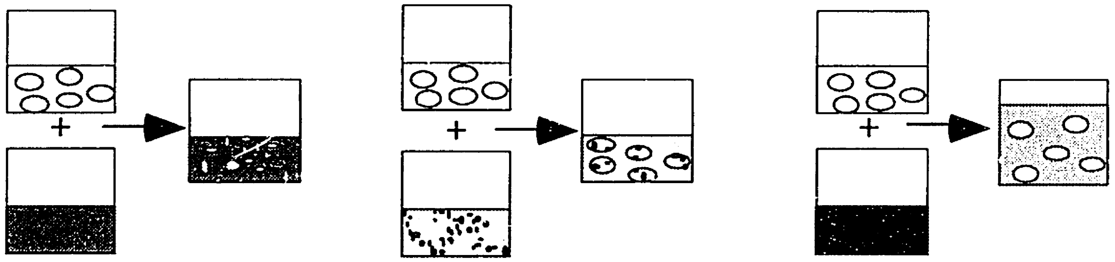

a) lysing

b) staining

c) diluting

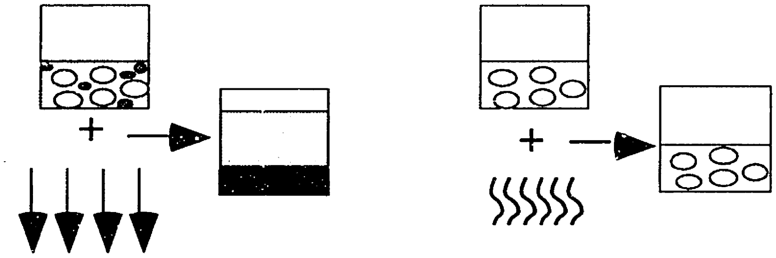

d) centrifugation

e) incubation

Figure 1-1: Common steps in sample preparation

In light of these advantages, the author proposes a microfabricated sample preparation system consisting of a microfabricated cantilever-plate flapper valve used to mix two liquids. This liquid mixer is comprised of two structures bonded together (Figure 1-2). The bottom layer is a silicon wafer which contains the cantilever-plate flapper valve over a valve seat (Figure 1-3) and ports. A flapper valve is used to allow for non-continuous sample mixing. The top layer is a glass wafer which contains the fluidic channels. The two sections are bonded together to create the liquid mixer. The top structure is made of silicon because of the excellent mechanical properties of silicon and the ease with which it can be isotropically and anisotropically etched. Glass is used for the bottom structure because it allows for visual observation of the mixing in the channel.

The schematic operation of the liquid mixer is shown in Figure 1-4. At time zero, sample flows down the channel (Figure 1-4a). When it is time to mix a reagent with the sample, the reagent is injected into the sample stream (Figure 1-4b), and the two mix diffusively in a few seconds (Figure 1-4c). After the desired section of sample is prepared, the reagent is shut off (Figure 1-4d) and the mixed sample and reagent flow down the channel and out of the liquid mixer.

The liquid mixer is controlled by varying the reagent and sample flow rates. The relative flow rates (and whether they are actually flowing) in turn determine the mixing ratio and the pressures at the reagent and sample ports; the cantilever plate aligns itself accordingly. This means that the liquid mixer is passively pressure-actuated.

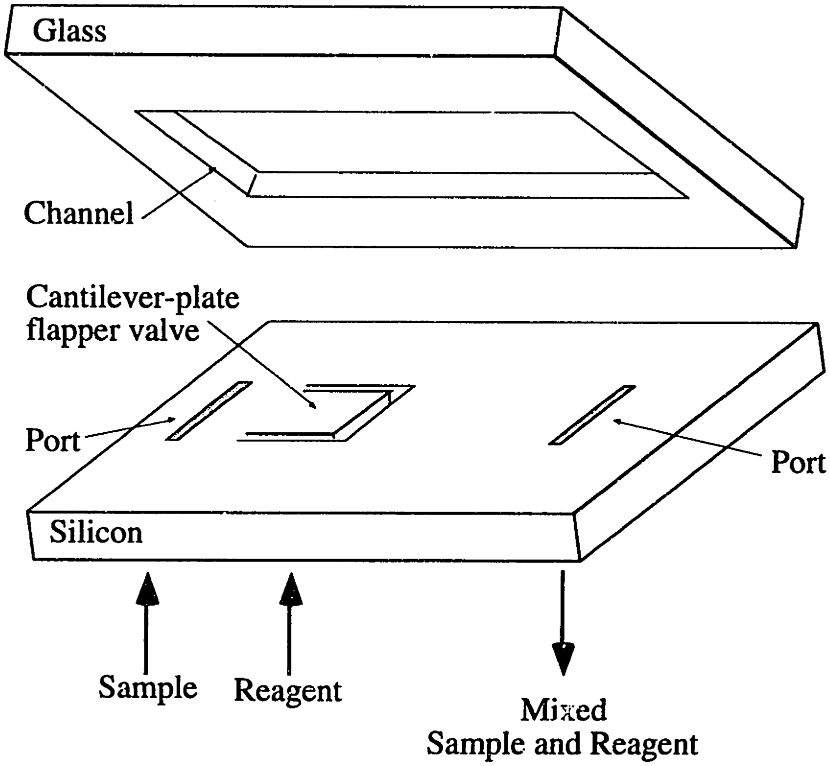

Figure 1-2: Schematic of liquid mixer

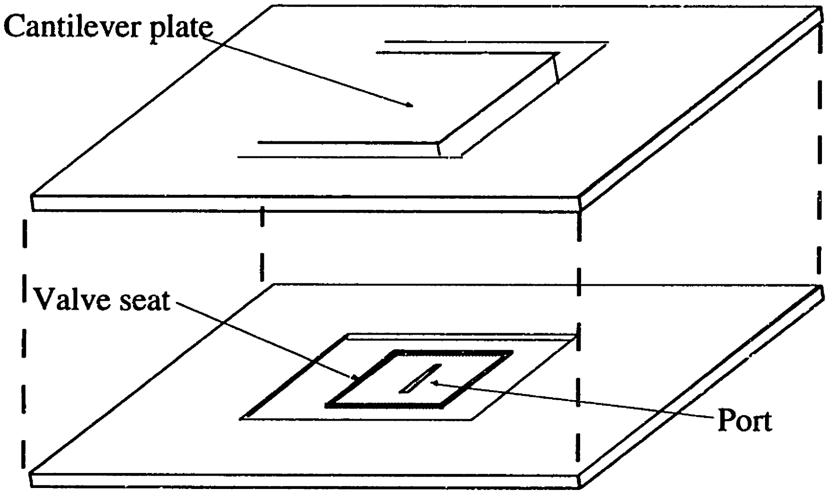

Figure 1-3: Cantilever-plate flapper valve

1.2 Flow Cytometry

To be able to determine specifications for the liquid mixer, the author has chosen flow cytometry as a model analysis system. Flow cytometry [4] is an analysis method in which a stream of particles (usually cells) are analyzed sequentially for a given piece of information, but at high enough rates that large (statistically significant) populations can be analyzed in a short time. A schematic flow cytometric system is shown in Figure 1-5. The particles flow single-file past a beam of light. The scattered light is detected to determine the physical characteristics of the particles (usually cell size and shape). The fluorescence signal is used to determine whether the particle has been successfully tagged with a stain (usually an immunological agent). Flow cytometry has many applications in the clinical and research realm, most often in immunology.

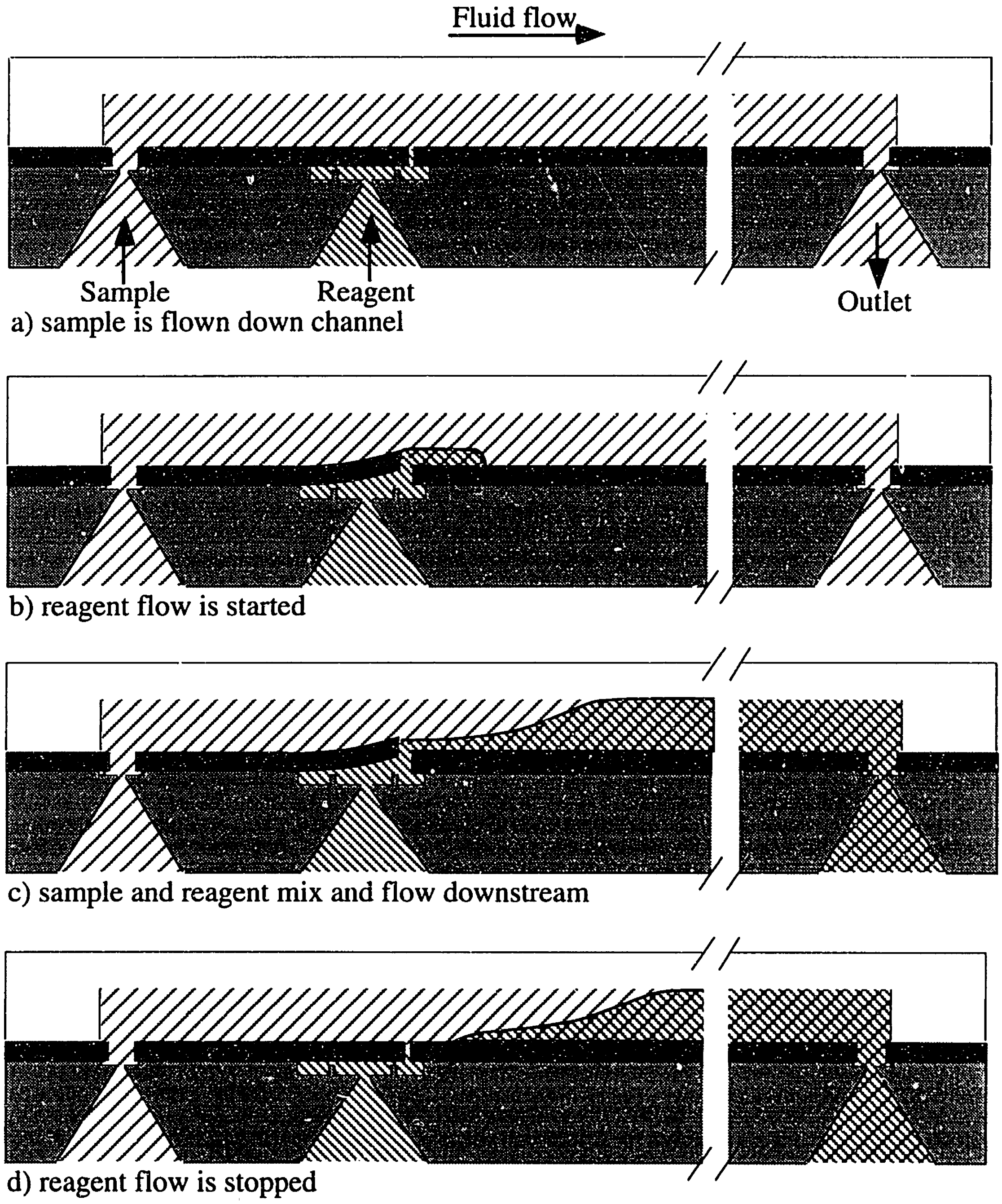

a) sample is flown down channel

b) reagent flow is started

c) sample and reagent mix and flow downstream

d) reagent flow is stopped

Figure 1-4: Liquid mixer operation

Flow cytometry is chosen as the model system for several reasons. First, it almost always uses whole cells, which gives important design constraints for the liquid mixer. Second, there are several simplified approaches to sample preparation for flow cytometry [5,6] which leads to the possibility that they may be applied here with only minor alteration. Third, attempts have been made to microfabricate flow cytometric cells [7,8,9,10]. Most notably, Sobek, et. al., at MIT has microfabricated flow chambers for flow cytometry out of fused silica [11,12]. The opportunity exists then, to realize an integrated device consisting of a microfabricated sample preparation system (the liquid mixer) with a microfabricated analysis system (the microfabricated flow cytometer).

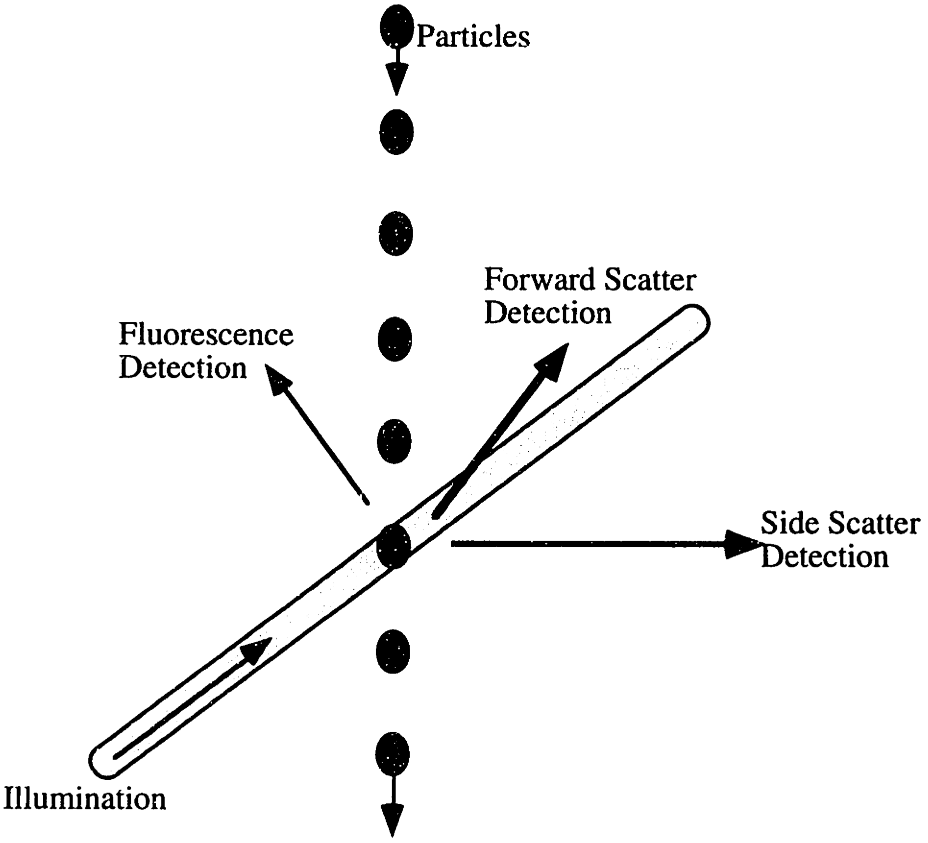

Figure 1-5: Flow cytometric system

There have been several previous attempts to incorporate automated sample preparation into flow cytometry by modifying existing flow cytometers. Finney, et. al., first modified a flow cytometer by adding an extra syringe and valve to allow for on-line mixing [13], similar to the proposed design. The main difference is that their design used milliliter volumes, as opposed to the microliter volumes used here, and the valve was manually operated. That group [13] introduced a second design [14] incorporating temperature control and a magnetic stirrer for mixing, but it still used milliliter volumes. Several groups also utilized stirrers to accomplish mixing [15,16,17]. Dunne [18] used diffusional mixing in small diameter tubes to study cellular kinetics. His approach did not yield complete mixing, though, as he was concerned with controlling the time of analysis, not mixing reagents. Finally, a group at the University of Washington constructed an automated sample preparation system using multi-port valves [19,20,21]. Their system was more general than the proposed liquid mixer, but used larger sample volumes (30-100 μl). All the sample preparation systems outlined above were macroscopic additions to macroscopic flow cytometers, and thus needed larger volumes and flow rates for operation. In contrast, the microfabricated liquid mixer works with well-defined small volumes of sample and reagent and can be integrated with a microfabricated flow cytometer.

1.3 Other Work

In addition to flow cytometry, there exist several other areas where sample preparation has intersected microfabrication to produce useful technologies. One area is the burgeoning field of microfabricated biochemical and chemical analysis systems [22]. These systems are billed as "total analysis systems", and as such they aim to incorporate sample preparation and analysis. Integrated biochemical and chemical analysis systems were first proposed and fabricated around 1991 [23,24,25]. Most of the early work in the field [26,27,28] was in the analysis regime, using electroosmotic and electrophoretic effects to move samples and separate mixtures of analytes. Recent work by Harrison's group at the University of Alberta [29,30,31] has incorporated sample preparation in the form of on-line immunochemical reactions. In addition, Manz's group used free-flow electrophoresis to separate analytcs as a sample pretreatment system [32], although the distinction between sample preparation and sample analysis gets blurred in this case.

Besides the "total analysis systems", several attempts have been made to microfabricate sample preparation systems, either alone or in conjunction with analysis systems. Verpoorte, et. al., used a many-layered stack of silicon wafers to integrate mixers, valves, pumps, and a detector for biochemical analyses [33]. Northrup, et. al., microfabricated a chamber capable of performing polymerase chain reaction (PCR) on-chip [34], which is often used in sample preparation for molecular biology assays. Finally, Miyake's group incorporated their microfabricated mixer [36] with an analysis chamber to make an absorptiometer [35].

Other work has concentrated on microfabricated liquid mixers. Several approaches have been tried. Miyake's micromixer [36] used a plate with holes to break the reagent stream into fluid jets, thus shortening the diffusive mixing time. N. Schwesinger, et. al., [37] and J. Branebjerg, et. al., [38] repeatedly separated and rejoined the fluid streams, layering them each time and thus cutting the diffusion time needed for mixing. Recently, a group at the University of California at Berkeley [39] used laminar chaotic advection, which mixes two liquids by constructing a flow field whereby small differences in a fluid particle's initial location may lead to large differences in its final location. This causes a chaotic rearrangement of the fluid particles which mixes the two liquids, although no results have been shown to date. While all of these designs work, they cannot be used for the application this thesis is concerned with because they are continuous-mixing devices, whereas the microfabricated liquid mixer has a cantilever-plate flapper to allow discrete mixing of two fluids.

While the microfabricated liquid mixer is a mixer, it uses a cantilever-plate flapper valve to achieve this. It is thus useful to investigate some of the previous work on flapper valves. The first "traditional" cantilever-plate flapper valve over an anisotropically etched cavity was demonstrated by Tirén, et. al., in 1989 [40]. In 1990, Ohnstein, et. al, fabricated an electrically actuated flapper valve for gas handling [41]. Emmer, et. al., used cantilever-plate flapper valves for chromatography [42]. Finally, two groups have performed coupled hydro-mechanical simulations of cantilever-plate flapper valves to determine their performance [43,44,45].

1.4 Thesis Overview

The remaining chapters in this thesis describe the design, fabrication, and testing of the liquid mixer. The next chapter delves into the design of the liquid mixer, designing the channel, the cantilever-plate, and all the peripheral parts. The third chapter details its fabrication, going through the process development and execution. The fourth chapter concerns testing and validation. It includes a discussion of the test setup and results on the operation of the liquid mixer. The thesis finishes with conclusions and directions for further work.

Chapter 2

Design

This chapter details the design of the liquid mixer using specifications which will be described in the next section. The liquid mixer involves a coupling between two physical domains, fluid mechanics and structural mechanics. This is illustrated in the following example: when there is flow in the channel, the pressure distribution (from the fluid) applied to the cantilever plate causes it to bend, which changes the boundary conditions for the fluid mechanics. This in turn changes the pressure distribution, which changes the bending, until the system reaches an equilibrium between the two forces. A proper analysis of this system would include the coupling between the two domains and the full three-dimensionality of the situation. In addition, since fluid mechanics and plate mechanics are inherently non-linear, the problem involves a set of coupled non-linear differential equations. Such an analysis is beyond the scope of this thesis, although other groups attempt this [43,44,45].

In order to make the problem more tractable, the coupling between the fluid mechanics and the structural mechanics needs to be broken. This allows a design around each domain independently, which means that the channel and the cantilever plate can be analyzed separately.

The first step is to determine the specifications for the liquid mixer. Once this is done, the channel in which the fluid flows is designed. This is accomplished by stating the assumptions used in the design and then using simulations and analytical models to determine the proper channel dimensions. Using a similar method, the cantilever plate dimensions, the valve seat dimensions, and finally the port dimensions and overall chip size are determined.

2.1 Specifications

The specifications govern the overall action of the liquid mixer. As stated earlier, they are determined with flow cytometry as the model system. First, the sample volume needs to be minimized to reduce reagent consumption. Since different flow cytometric assays involve widely varying percentages of positively labeled cells, a specific protocol needs to be considered to obtain a sample size specification. For this thesis, a protocol for immunophenotyping (determining various different cell subpopulations) white blood cells is used to set a limit [46]. The protocol calls for 10,000 events, where each event is defined as a particle (white blood cell, red blood cell remnant, etc.) passing through the flow cytometer. Since there are approximately 10,000 white blood cells in each microliter of blood, a sample size of one microliter should give a sufficient number of events. Second, the time needed to completely run the assay (assay run time) should be relatively short, so 30 seconds is chosen. Note that this is not the sample and reagent mixing time, which is much shorter. The assay run time is the time needed to inject (and mix) the full volume of sample and reagent, while the mixing time is the time needed to mix the sample with the reagent as it flows downstream. Third, the liquid mixer should be able to mix widely varying ratios of sample and reagent in a short time. Mixing ratios of 1:1 (sample:reagent) to 10:1 are chosen. Finally, the liquid mixer should not need much pressure to actuate it. Ten pounds per square inch (psi) is chosen as this limit. The specifications for the liquid mixer are repeated below in Table 2-1.

Table 2-1: Liquid Mixer Specifications

Specification	Symbol	Value
Sample Volume	V_S	1 µL
Assay Run Time	T	30 sec
Mixing Ratio	R	1:1 to 10:1
External Pressure Load	P	<10 psi

2.2 Channel Design

Table 2-2 lists the three parameters that must be determined for the channel. Figure 2-1 gives a pictorial representation.

Table 2-2: Channel design parameters

Parameter	Symbol
Channel Height	h
Channel Width, Plate Width	w

Channel Length	l_c

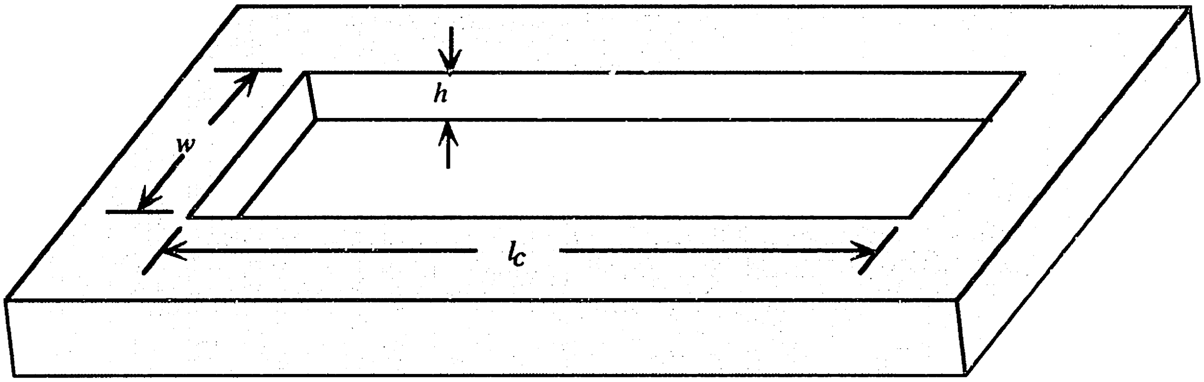

Figure 2-1: Channel dimensions

2.2.1 Assumptions

The fluid mechanics of the problem are governed by the Navier-Stokes equations, which can be used to solve for the velocity (v) and pressure (p) distribution in a fluid. For an incompressible fluid they are given as [47]

$$\rho \frac{D\mathbf{v}}{Dt} = -\nabla \mathrm{P} + \eta \nabla^2 \mathbf{v} \tag{2.1}$$

where ρ is the density of the fluid and η is the fluid viscosity. This first assumption of incompressibility is valid for water and other biologically relevant fluids at the pressures of interest. The derivative with time refers to the substantial derivative of the velocity, which is the derivative with time of the flow velocity with respect to a moving fluid particle. It is given by

$$\frac{D\mathbf{v}}{Dt} = \frac{\partial \mathbf{v}}{\partial t} + (\mathbf{v} \bullet \nabla)\mathbf{v} \tag{2.2}$$

The pressure P refers to the equivalent pressure, and includes the static pressure, the dynamic pressure, and the equivalent pressure due to the weight of the fluid. It is

$$\mathrm{P} = p - \frac{1}{3}\eta \nabla \bullet \mathbf{v} + \rho g h \tag{2.3}$$

where g is the acceleration of gravity and h is the relative height difference between the fluid and an arbitrary zero reference.

These equations, with the conservation of mass, can be used to determined the flow parameters (pressure and velocity) in a flow field for given boundary conditions and initial conditions.

A second assumption concerns the relative contributions of the inertial and viscous terms in the Navier-Stokes equations. These can be estimated by nondimensionalizing the Navier-Stokes equations, giving

$$Re\left(\frac{\partial \tilde{v}}{\partial \tilde{t}} + \tilde{\mathbf{v}} \bullet \tilde{\nabla}\tilde{\mathbf{v}}\right) = -\tilde{\nabla}\tilde{\mathrm{P}} + \tilde{\nabla}^2\tilde{\mathbf{v}} \tag{2.4}$$

where *Re* is the Reynolds number, defined as

$$Re = \frac{LV\rho}{\eta} \tag{2.5}$$

Here L is a characteristic physical length, V is a characteristic fluid velocity, and ρ and η are the aforementioned fluid properties. This nondimensional quantity is used to typify the flow situation. When the Reynolds number is small ($\ll 1$), the viscous terms (right side of equation 2.4) dominate the inertial terms (left side), and the inertial terms can be excluded from the Navier-Stokes equations, giving, in dimensionalized form

$$\nabla P = \eta \nabla^2 \mathbf{v} \tag{2.6}$$

This is a linear form of the Navier-Stokes equations known as creeping flow or Stokes flow, which is much easier to solve. Since the dimensions involved in micromachined structures are small, since the flow velocities used are small, and since the viscosity of water is relatively large (compared to gases), the Reynolds number will be small, and the linearized form can thus be assumed. It is very important to note, though, that the characteristic velocities and lengths may change dramatically within a physical domain, and so the linearized form of the Navier-Stokes equations may only be applicable in certain regimes of the problem. This is especially true around corners and where dimensional scales are changing rapidly.

The major consequence of this assumption is that there is no turbulence, and thus the major mixing mechanism will be diffusional mixing. Instabilities and vorticity, though, are not forbidden in the linearized Navier-Stokes equations, and one can induce flow instabilities and vorticity to enhance mixing. The liquid mixer does not incorporate these effects into the design but they may nonetheless occur, reducing mixing times.

The other assumption made in the design is that the channel will be perfectly rectangular. This simplifies the math greatly and is taken for convenience.

2.2.2 Diffusion simulations

As the reagent flows into the channel, it will mix with the sample stream, as shown in Figure 1-4. This mixing can be modeled by assuming diffusion as the mixing mechanism and solving the relevant equations. A simplified analysis of the situation is given in Appendix A, with the following assumptions:

1. There is no convection.
2. The concentrations of the sample and reagent are low.
3. The channel is perfectly rectangular.
4. There are no concentration variations along the width of the channel.
5. The sample and reagent initially exist as two layers in the channel.

The two important results from this analysis are

$$\begin{aligned} C(x,t) &= \sum_{n=1}^{\infty} \frac{2}{n\pi} C_0 \sin\left(\frac{n\pi d}{h}\right) \cos\left(\frac{n\pi x}{h}\right) e^{-\left(\frac{n\pi}{h}\right)^2 Dt} \\ T_m &= \frac{h^2}{\pi^2 D} \ln\left[\frac{400C_0}{\pi} \sin\left(\frac{\pi d}{h}\right)\right] \end{aligned} \tag{2.7}$$

Here $C(x,t)$ is the concentration of the reagent in the channel for all time, x is the height above the channel floor, C_0 is the initial concentration of the reagent, d is the initial height of the reagent (determined by the mixing ratio), h is the height of the channel, D is the diffusivity of the reagent in the sample and T_m is the mixing time. The top equation gives the instantaneous concentration of the reagent and the bottom equation gives the mixing time needed for a less than 1% reagent variation in the channel cross-section. Several solutions for the concentration profile with different mixing ratios are given in Figure 2-2 to 2-4.

Several things can be learned from these formulas. First, the mixing time is largest for a mixing ratio of 1:1 and decreases as the mixing ratio increases. Second, the equations are symmetrical around mixing ratio, which means that a 1:4 mixing ratio will mix as fast as a 4:1 mixing ratio (Figure 2-5). Third, the mixing time is less than that predicted for diffusion into an infinite domain. This is due to the fact that the boundaries at the top and bottom of the channel reflect the diffusing species.

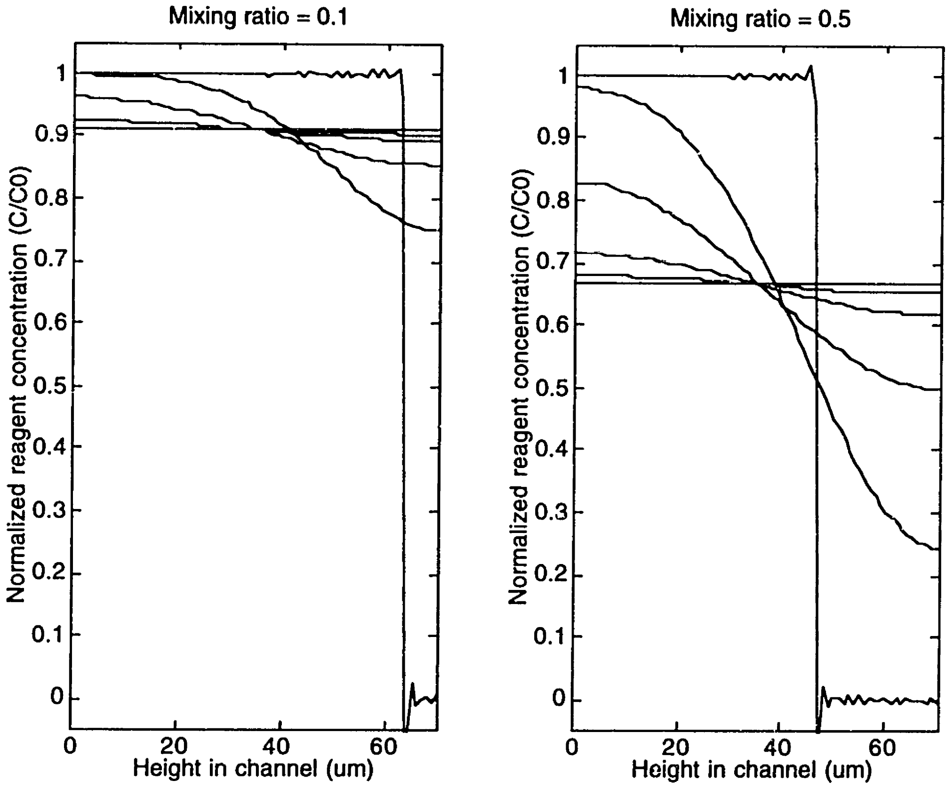
Mixing ratio = 0.1

Mixing ratio = 0.5

Figure 2-2: Concentration profiles for a mixing ratio of 0.1 and 0.5

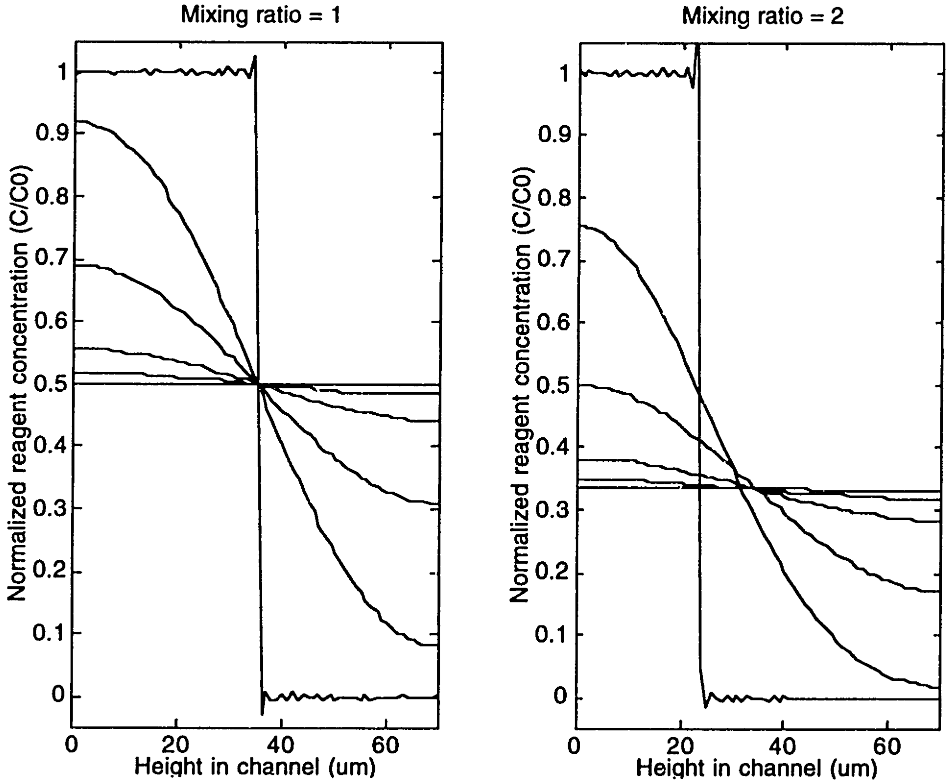
Mixing ratio = 1

Mixing ratio = 2

Figure 2-3: Concentration profiles for a mixing ratio of 1 and 2

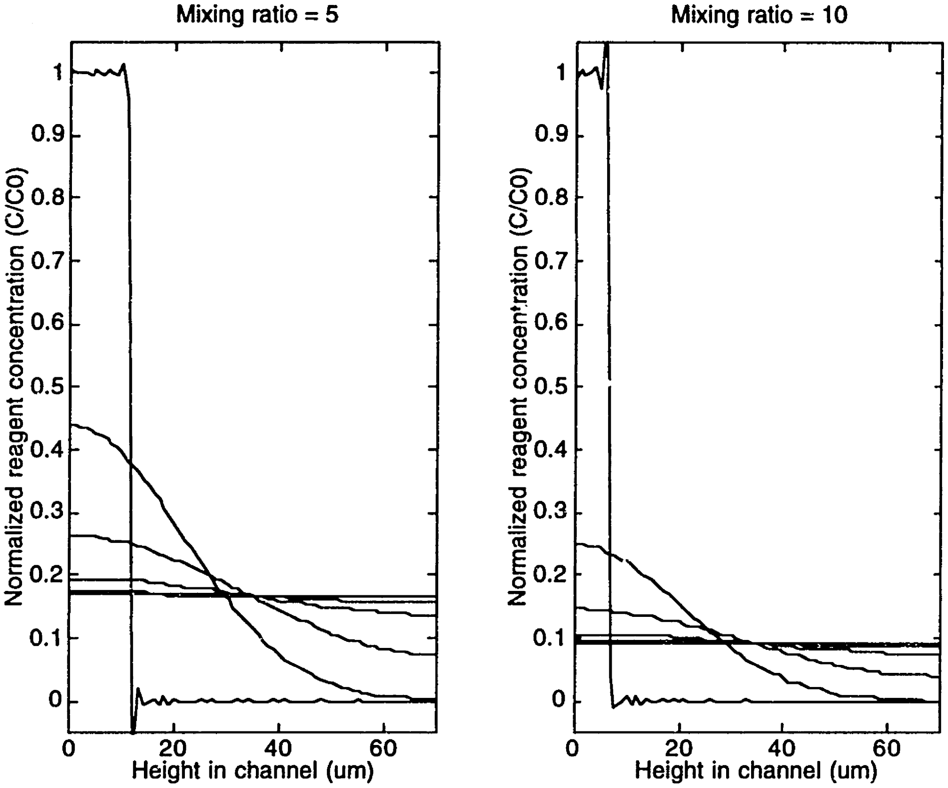

Figure 2-4: Concentration profiles for a mixing ratio of 5 and 10

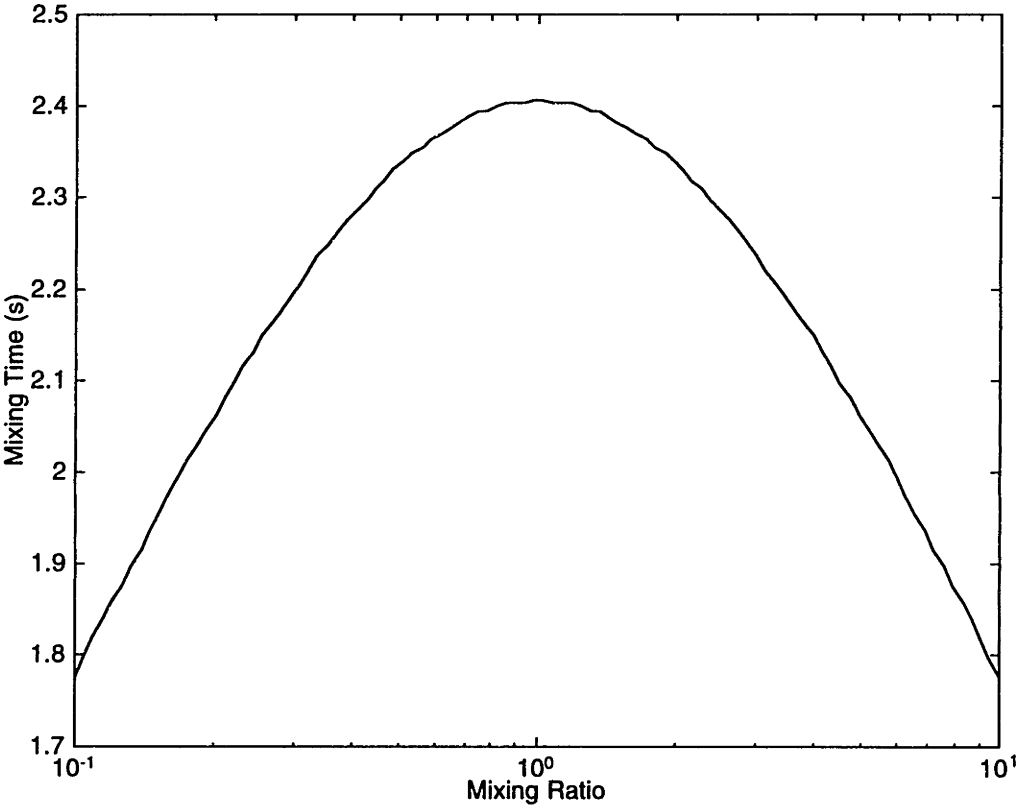

Figure 2-5: Mixing times for different mixing ratios

2.2.3 Analytical model

Using the mixing time derived in the previous section, the mixing length is given by the following formula.

$$L_m = v \cdot T_m \tag{2.8}$$

where L_m is the mixing length and v is the average linear flowrate. This is an approximation, since the velocity profile in the channel is not constant in x or y, and since the mixing time is itself a function of the velocity.

To determine the mixing length using equation 2.8, the average linear flowrate in the channel must be known. This can be derived as follows:

The reagent volume (V_R) consumed during an assay in terms of the sample volume (V_s) and the mixing ratio (R) is

$$V_R = \frac{1}{R} V_S \tag{2.9}$$

Thus, the total volume of liquids (V_T) consumed during an assay is

$$\begin{aligned} V_T &= V_S + V_R \\ &= V_S(1 + \frac{1}{R}) \end{aligned} \tag{2.10}$$

The volume flow rate (Q) of sample and reagent in the channel is

$$\begin{aligned} Q &= \frac{V_T}{T} \\ &= \frac{V_S}{T}(1 + \frac{1}{R}) \end{aligned} \tag{2.11}$$

Assuming a rectangular channel, this gives an average linear flow rate (v) of

$$\begin{aligned} v &= \frac{Q}{wh} \\ &= \frac{V_S}{whT}(1 + \frac{1}{R}) \end{aligned} \tag{2.12}$$

Thus, the mixing length is

$$L_m = \frac{V_S}{whT}(1 + \frac{1}{R})T_m \tag{2.13}$$

Inserting the result of equation 2.7 for the mixing time, the mixing length is

$$L_m = v \cdot T_m$$

$$L_m = \frac{V_S}{wT}(1+\frac{1}{R}) \cdot \frac{h}{\pi^2 D} \ln\left[\frac{400}{\pi}\sin\left(\pi\frac{R}{R+1}\right)\right] \tag{2.14}$$

So, while the mixing time is quadratic in *h*, the mixing length is only linearly dependent on the channel height.

To ensure adequate mixing given the assumptions and simplifications made in the design process, the channel length l_c should be much larger than the mixing length *L*. This leads to

$$l_c\left(\frac{w}{h}\right) >> (1+\frac{1}{R}) \cdot \frac{V_s}{\pi^2 TD} \ln\left[\frac{400}{\pi}\sin\left(\pi\frac{R}{R+1}\right)\right] \tag{2.15}$$

where the unknown quantities (l_c, *h,* and *w*) are grouped on one side.

To reduce the parameter space even more, conditions can be imposed on the channel height. First, since cells are often 20 to 30 μm in size, the channel height has to be larger than 50 μm to allow them to pass through unimpeded, as shown in Figure 2-6. Second, the maximum channel height is imposed by processing constraints, and by the fact that the mixing time is quadratically dependent on the channel height. A channel height of 70 μm is chosen as a compromise between the two requirements.

With the channel height fixed, two different channel geometries are chosen which meet the specifications of section 2.1. They are shown below in Table 2-3, along with the mixing time and mixing length for 1:1 mixing ratios.

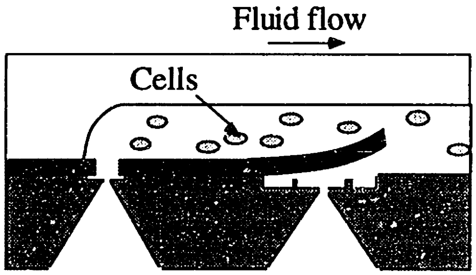

Figure 2-6: Minimum height requirement for channel

Table 2-3: Channel dimensions

Parameter	Design 1	Design 2
Channel width	800 μm	1000 μm
Channel height	70 μm	70 μm
Channel length	15 mm	15 mm
Mixing Time	2.4 s	2.4 s
Mixing Length	2.9 mm	2.3 mm

2.3 Cantilever Plate Design

The cantilever plate design involves determining the dimensions of the plate that will allow activation at the required pressures (< 10 psi). Since the plate will be the same width as the channel (to ensure one-dimensional mixing) the two parameters necessary to find are the length of the plate and the thickness of the plate. They are shown in the table below, and in Figure 2-7.

Table 2-4: Cantilever plate design parameters

Parameter	Symbol
Plate Thickness	*a*
Plate Length	*l*

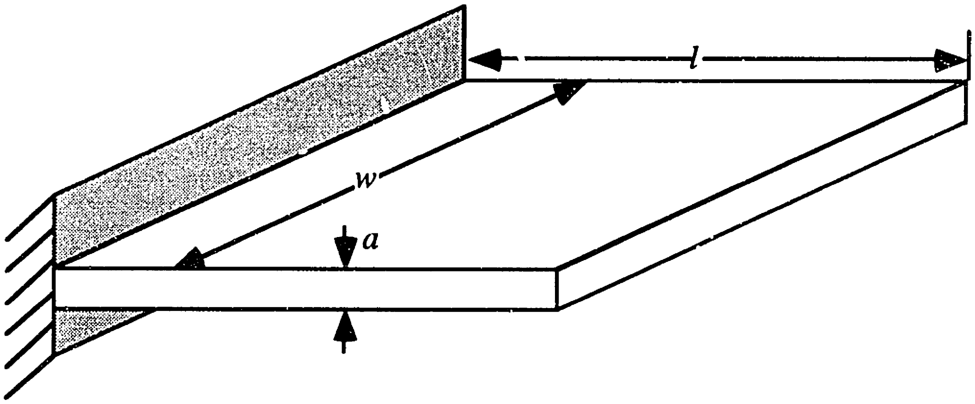

Figure 2-7: Cantilever plate dimensions

2.3.1 Assumptions

The main assumption surrounding the cantilever-plate design is that the linear differential equations can be used, and thus the maximum deflection is linearly related to pressure. This assumption will be validated later in this section. The other assumption in the plate design is that the pressure distribution under the plate is constant, which will not be the case when flow is impinging on the plate. This should not affect the design greatly because the plate will be flexible enough that substantially different pressure distributions will still result in successful mixer operation.

2.3.2 Analytical model

The deflection of the plate is governed by plate mechanics. Neglecting nonlinear terms, the differential equation governing the deflection of a plate under an arbitrary pressure distribution is [48]

$$\frac{\partial^4 w}{\partial x^4} + 2\frac{\partial^4 w}{\partial x^2 \partial y^2} + \frac{\partial^4 w}{\partial y^4} = \frac{q(x,y)}{D} \tag{2.16}$$

where q is the applied pressure, w is the deflection, and D is the flexural rigidity, which for a wide cantilever plate is given by

$$D = \frac{Ea^3}{12(1-v^2)} \tag{2.17}$$

where E is the modulus of elasticity of the material (169 Gpa for silicon), a is the thickness of the plate, and ν is Poisson's ratio (0.25 for silicon).

For a cantilever-plate subject to a uniform load, the variations in y (along the width) can be removed, and the problem can be treated as one-dimensional, giving the following differential equation

$$\frac{\partial^4 w}{\partial x^4} = \frac{q(x)}{D} \tag{2.18}$$

This gives a maximum deflection of

$$w_{\max} = \frac{Pl^4}{8D} \tag{2.19}$$

where P is the pressure applied.

The thickness of the cantilever beam is chosen to be 10 μm, as this corresponds to the available processing material (see Chapter 3). Since the maximum deflection at 10 psi should be at least 35 μm, this constrains the plate lengths.

Two different plate lengths are chosen, and incorporating them with the two different channel designs gives the following four designs.

Table 2-5: Plate dimensions

Parameter	Design 1	Design 2	Design 3	Design 4
width (μm)	800	1000	800	1000
height (μm)	10	10	10	10
length (μm)	500	500	600	600
pressure needed for 35 μm deflection (psi)	9.8	9.8	4.7	4.7

Since the deflections that the cantilever beam will undergo may be quite large, the small-deflection (linear) theory may not apply in this case. Several analyses exist of cantilever beams undergoing large deflections [49, 50, 51]. Rohde [49] approximates the deflections by using a series of tangential circular arcs. By making the arcs small enough, she arrives at a reasonable approximate solution to the nonlinear differential equations. The paper includes a nondimensionalized plot of deflection versus pressure for a uniform load. Using this plot, the deflections of the cantilever-plate are seen to still be in the linear regime, even though they are "large". This is not unreasonable, since the definition of a "large" deflection is radically different for a clamped-clamped beam than for a cantilever beam, and since the ratio of the deflection (for the full channel height) to the plate length is a maximum of 0.14.

2.4 Valve seat and Port design

This final section details the design of the remaining aspects of the liquid mixer. While the constraints on these aspects of the liquid mixer are not very stringent, there are issues to deal with when designing them.

2.4.1 Valve Seat

The valve seat is used to seal the plate to prevent leakage. There are two constraints governing its design. The first is squeeze-film damping, which is an effect encountered when two objects move towards each other with a fluid in-between. Squeeze-film damping essentially slows the approach of the two plates because the fluid between them must be removed. This slows dynamic response. Even though the liquid mixer will operate in a steady-state regime, the valve seat should not be too shallow or this effect could make the response time of the plate too long (see Figure 2-8). The functional dependence of squeeze film damping is [52]

$$time \propto \frac{1}{height^2} \tag{2.20}$$

This means that as the distance (height) between two plates decreases, the time necessary to bring them closer together increases dramatically. Thus, increasing the clearance between the plate and the bottom of the valve seat will decrease the time required for the plate to move up and down.

The other constraints imposed on the valve seat design are processing constraints. In order to facilitate this first-round processing, the minimum linewidth and alignment tolerance is chosen to be 5 μm. Given these constraints, the valve seat design is shown in Figure 2-9.

2.4.2 Ports

The ports allow fluid to enter and leave the liquid mixer. There are three ports in the liquid mixer - the reagent inlet port, the sample inlet port, and the mixed sample+reagent outlet port. The constraints governing their design come from total applied pressure specifications and processing constraints.

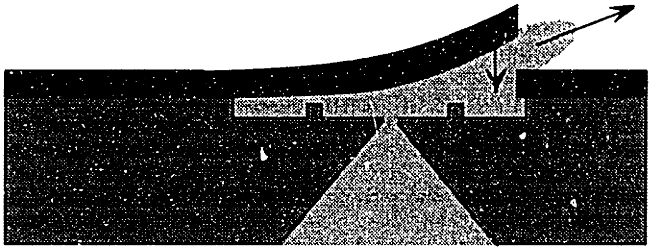

Figure 2-8: Squeeze film effect for flapper-valve

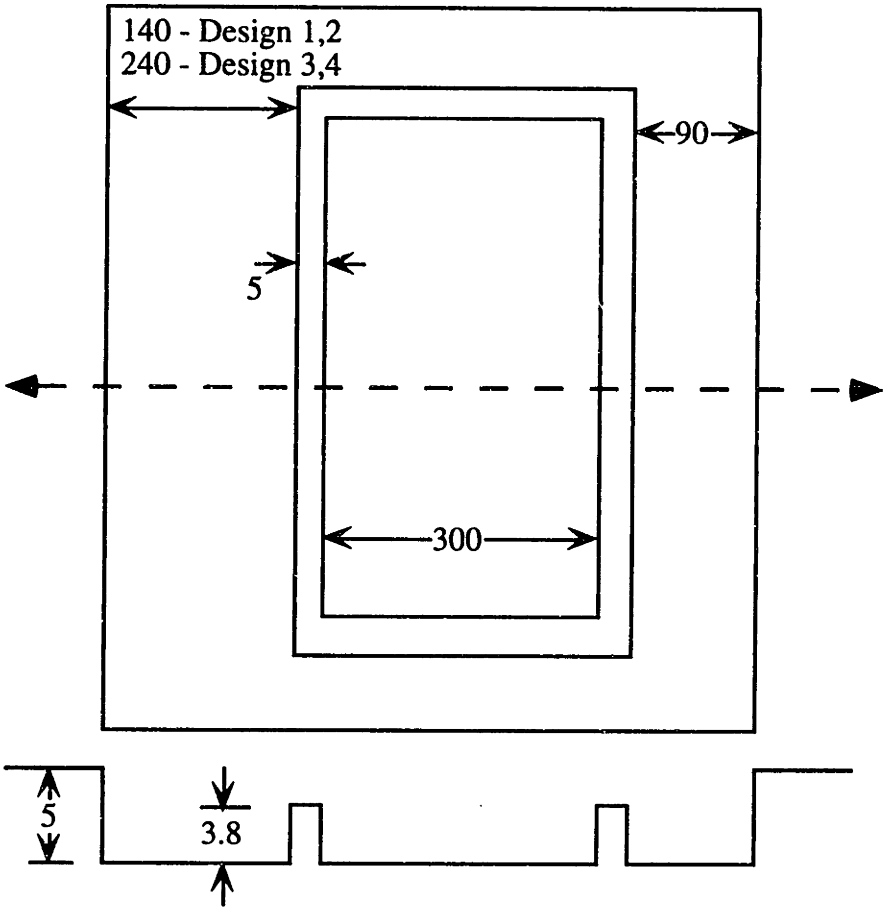

Figure 2-9: Valve seat dimensions (all dimensions in microns)

First, it is necessary to minimize the pressure drop across the port, as this will increase the pressure being applied across the plate to actuate it. The pressure-flow relation for a converging/diverging channel in creeping flow is [53]

$$\Delta P = \left[A \frac{1}{48} \frac{D_h^2}{t\mu} \frac{{D_h^3}/{D_{h'}^3} - 1}{1 - {D_{h'}}/{D_h}} \right]^{-1} Q \tag{2.21}$$

where A is the area at the top of the wafer, D_h is the hydraulic diameter at the top of the wafer, $D_{h'}$ is the hydraulic diameter at the bottom of the wafer, t is the thickness of the wafer, and Q and ΔP are the flow rate and pressure drop, respectively. The dimensions are illustrated in Figure 2-10. The hydraulic diameter for a rectangular cross section is

$$D_h = 2\left(\frac{1}{l} + \frac{1}{w}\right)^{-1} \tag{2.22}$$

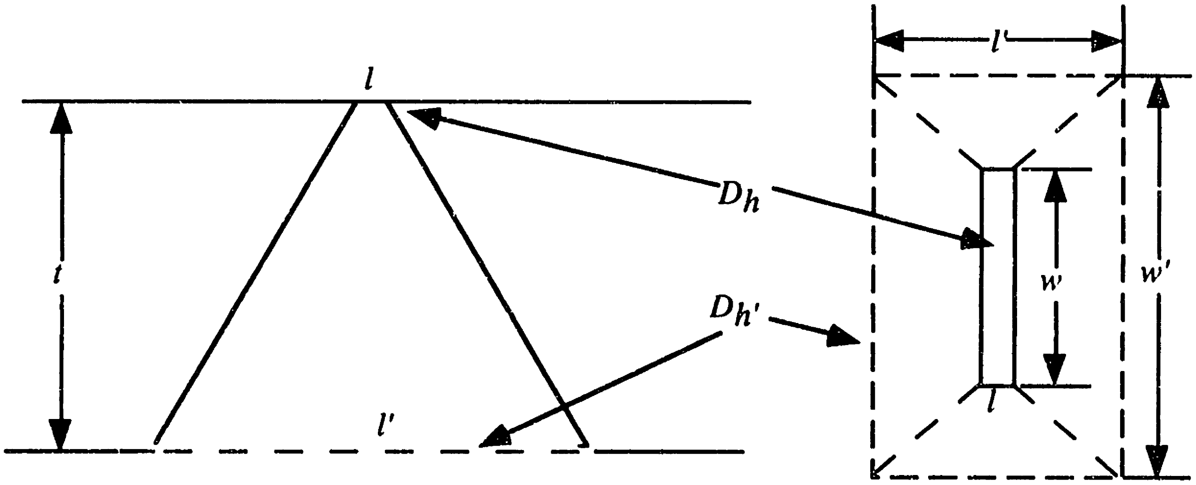

a) side view

b) top view

Figure 2-10: Port hole dimensions

From equation 2.21, it is evident that the pressure drop will increase dramatically as the hydraulic diameter is reduced. Since the hydraulic diameter is dominated by the port length (*l*), this should not be made too small.

The second constraint is that wafer thickness is not constant across the wafer or between wafers, and this will lead to differences in etched port dimensions. The port dimensions on the top of the wafer are related to the wafer thickness by

$$l = l' - 2\frac{t}{\tan(54.7°)} \tag{2. 23}$$

Thus, wafer thickness variations can severely impact port dimensions. Taking into account this variation, the finite etch rate of the <111> sidewalls KOH, and possible angular misalignment (which increases <111> etch rate), the port dimensions are chosen to be (for a wafer thickness of 480 μm)

Table 2-6: Port Dimensions

Parameter	Design 1	Design 2
w'	1480	1280
l'	690	690
w (calculated)	810	610
l (calculated	20	20

2.4.3 Chip Dimensions

The chip dimensions are chosen to be as small as possible, to maximize the number of chips on each wafer, but large enough to be able to package the chip. The first constraint is that the reagent inlet port and sample inlet port cannot be too close together or they will hamper packaging. This distance must also be larger than the entrance length needed to fully develop the flow coming out of the sample inlet port. For these low Reynolds number flows, this length is much less than that imposed by packaging constraints.

The second issue is the size of the chip itself. A chip size of 5 mm x 20 mm is chosen as it allows for a long channel (to study different flows) and adequate packaging area. The port hole placement is shown in Figure 2-11.

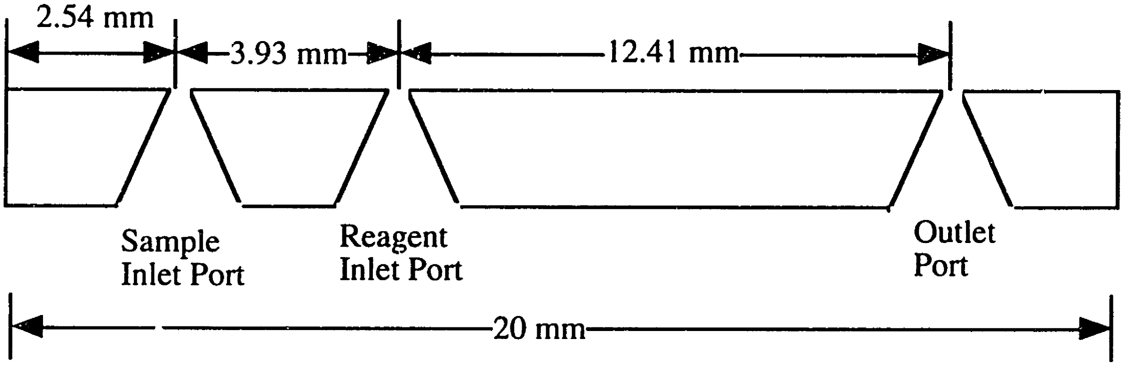

Figure 2-11: Port placements

Chapter 3

Fabrication

This chapter describes the detailed fabrication sequence used to fabricate the liquid mixer. A complete process flow is included in Appendix A. First, an overview of the fabrication sequence is given, followed by a description of the mask set. This is in turn followed by a detailed description of the processing sequence, including process development and experimental observations.

3.1 Overall Process Sequence

There are three distinct overall parts to the fabrication process. The first is the formation of the cantilever-plate flapper valve structure on a silicon substrate. The second is the formation of the flow channels in a glass substrate. The third is the bringing together of the glass and the silicon into one unit and cutting the wafer to make the chips.

In the context of the three parts of the fabrication process, two different processes were attempted, version 1 and version 2. Process version 1 did not result in any completed devices, for reasons that will be discussed below. It is still worthy of discussion as many lessons were learned during its execution.

A pictorial process flow for version 1 is shown in Figure 3-1. All the pictorial process flows in this chapter show only the flapper valve and sample port hole. The mixed outlet port hole is identical to the sample port hole and so is not displayed. The process commenced by forming the valve seat in an n-type silicon handle wafer (Figure 3-1a). A layer of thermal oxide was then grown to serve as an etch stop in a later step (Figure 3-1b). The wafer was fusion bonded (in oxygen) to a p-type wafer which had previously had an n+ layer defined on it by implantation and drive-in (Figure 3-1c). The bonded pair was then annealed. The device (top) wafer was thinned using an electrochemical etch stop technique which stopped on the n-type layer in the p-type wafer, leaving a silicon overlayer (Figure 3-1d). Following the thin-back, the wafer was subjected to a chemo-mechanical polish (CMP) [54,55], which smoothed the roughness caused during the thin-back etch (Figure 3-1e). Next, the port holes were etched through the wafer (Figure 3-1f). A silicon nitride layer was used as a mask for the etch around the majority of the wafer, while the thermal oxide previously grown was used as an etch stop in the valve seat and ports. Next, the silicon overlayer was defined and etched to produce the cantilever plate (Figure 3-1g). Finally, the silicon wafer was anodically bonded to a glass wafer with channels etched in it (Figure 3-1h), completing the device.

a) define valve seat

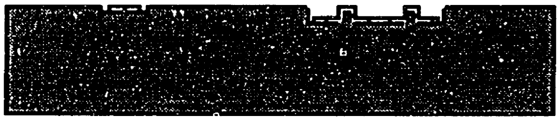

b) grow and pattern thermal oxide

c) fusion bond p-type wafer w/ n-type layer

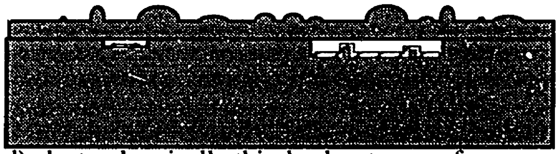

d) electrochemically thin-back p-type wafer

e) chemo-mechanically polish to smooth surface

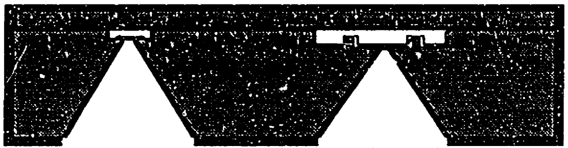

f) etch port holes using nitride etch mask

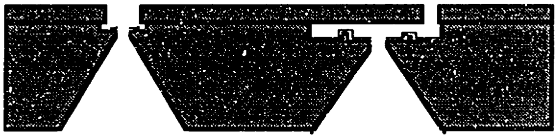

g) define and etch plate

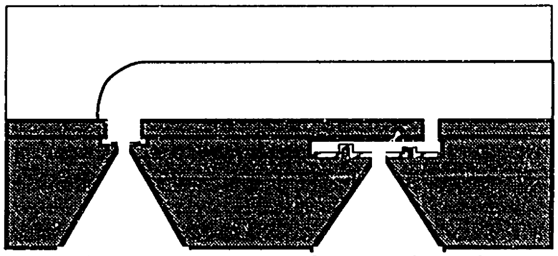

h) anodically bond glass wafer with channels

Figure 3-1: Liquid mixer version 1 process flow

Five processing challenges were encountered with version 1. First, it was very important to pattern the thermal oxide layer (Figure 3-1b) such that no oxide was left in the field (outside the valve seat). Any piece of oxide left in the field from a mask defect would have caused a void during subsequent fusion bonding (Figure 3-1c). This necessitated a process whereby the photolithographic exposure was done with two masks; any defect in the first mask was unlikely to appear in the exact same place on the second mask, giving some redundancy to the process. The second processing challenge involved patterning the photoresist in the valve seat trenches during this step. This necessitated a three-layer photoresist process which was able to conformally coat all the topography on the wafer. The third processing challenge involved a problem with the fusion bonding. For some (still unresolved) reason, the two wafers would not bond at all after the thermal oxide had been patterned and etched. The reason for the problem was not isolated, although possible causes include process-induced surface contamination or higher-than-average surface roughness randomly distributed among the wafers. This problem was overcome by performing a CMP before the bonding step to remove the surface layer. The fourth challenge encountered in the process was that the bonded pair was very rough following the thin-back electrochemical etch in potassium hydroxide (KOH). A CMP process was developed which was able to reduce this roughness from several microns to several nanometers, allowing anodic bonding to take place. The fifth process challenge involved the port hole etch. The etch was a "blind etch", whereby the etch had to stop on a buried thermal oxide. Unfortunately, for many of the same reasons described in Section 3.2.3, the port holes emerged on the top wafer surface much larger than calculated and blew out the thermal oxide. This removed the top layer, destroying the wafer. Because of this problem, and to ease the processing challenges encountered during the rest of the fabrication sequence, a version 2 process was developed. This process removed all the CMP steps and the difficult patterning of the thermal oxide while moving all the "critical" (KOH) etches to the beginning of the process, thereby making it more robust. Given more time to work out the problems, though, the version 1 process would have been a success. The rest of the chapter will only discuss the version 2 process.

As stated before, the process comprises of three key elements, which will be discussed in detail. The first element is the formation of the cantilever-plate flapper valve. It is comprised of four subsequences, which are shown in Figure 3-2a-d. The first subsequence is the definition of the valve seat in the handle wafer (Figure 3-2a). The valve seat is fabricated via standard lithography and plasma etching. Next, the port holes are anisotropically etched in the silicon (Figure 3-2b). A silicon-on-insulator (SOI) device wafer is then fusion bonded to the handle wafer and thinned back in KOH to define the top layer (Figure 3-2c). Finally, holes are plasma etched through the top layer to define the cantilever plate and open the port holes (Figure 3-2d). This completes the formation of the cantilever-plate flapper valve.

The formation of the glass channels for fluid flow is comprised of one basic process, illustrated in the fifth panel of Figure 3-2. The glass used is Corning 7740 glass, commonly known as Pyrex®. A protective mask is deposited on the glass. Holes corresponding to the channels are defined on the mask. This layer is then used as a mask during a subsequent wet etch step to define the fluid channels. Finally, the mask is removed, leaving channels in the bare glass.

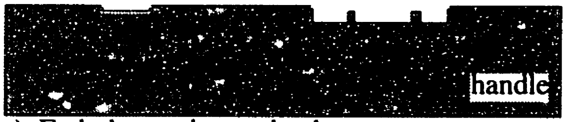

a) Etch depression and valve seat

b) Etch port holes

c) Bond and thin back SOI wafer

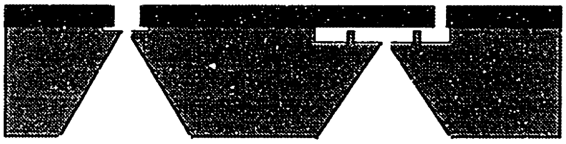

d) Etch cantilever plate

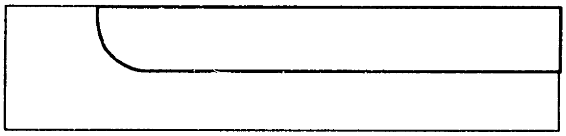

e) Etch channels in glass wafer

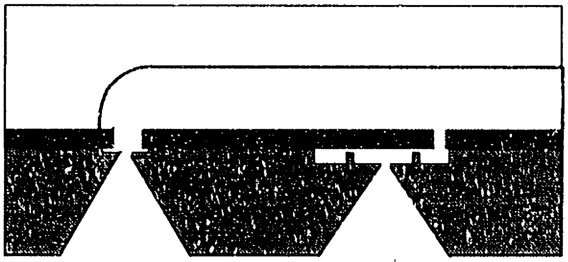

f) Anodically bond glass wafer to silicon wafer

Figure 3-2: Liquid mixer process overview

The third and final element of the liquid mixer process is to complete the device by bringing the two parts together. First, the silicon and glass wafers are aligned and anodically bonded (Figure 3-2f). Then, the wafer is diced into chips. This completes the fabrication of the liquid mixer.

3.2 Process Sequence - Flapper valve

3.2.1 Starting Material

The starting material for the handle wafer is 100 mm <100> single-crystal prime n-type silicon. Since no electrical devices are being fabricated - only a mechanical structure - the dopant and resistivity are of little importance. 0.5-2.0 Ω-cm wafers are used for this process.

The starting material for the device wafer is an SOI wafer. A 10 μm SIMOX SOI wafer is used, with <100> single-crystal prime p-type surface layer and bulk. The implanted oxide is 4 kÅ thick.

Since an infrared alignment step is used in the process, it is crucial that the both sides of the wafer be polished to reduce light scattering, thereby maximizing contrast. Thus, a pre-step in the process is to have the handle wafers' backsides polished. This is done through a local polishing service [56], yielding double-polished wafers.

3.2.2 Valve Seat Definition

Defining the valve seat is the first subsequence of the liquid mixer fabrication. Comprising of four steps, it is detailed in Figure 3-3. The first step in the process is to perform a Piranha clean (3:1 H_2SO_4:H_2O_2) of the wafers (Figure 3-3a) to remove organics and gross particulates incurred in the backside polishing process. Then a standard lithography step is used to define the trenches. The purpose of this first mask is to recess the valve seat from the top surface of the silicon, thus preventing the valve seat from bonding to the SOI wafer.

Next, the photolithographically defined depressions are anisotropically etched in the silicon in an SF_6/CCl_4 plasma using a standard recipe (see Appendix A) to a depth of 1.2 μm (Figure 3-3b).

The photoresist is removed with a Piranha clean, and a new photoresist layer is spun for the second mask, which defines the valve seat itself. This new photoresist layer is actually a double layer of photoresist, each spun using the standard recipe with a prebake in-between. Since the wafer surface is no longer planar, the double layer ensures that a conformal coat is achieved. The second mask is patterned, using longer exposure and develop times (see Appendix A).

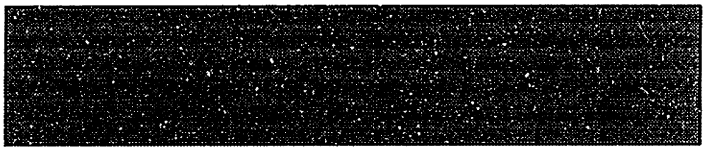
a) clean double-polished n-type wafer

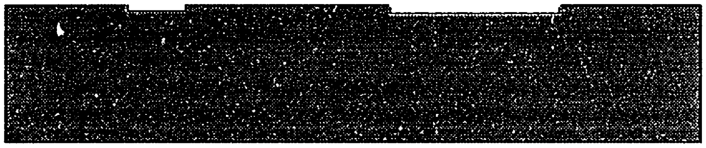
b) pattern and etch 1.2um depression

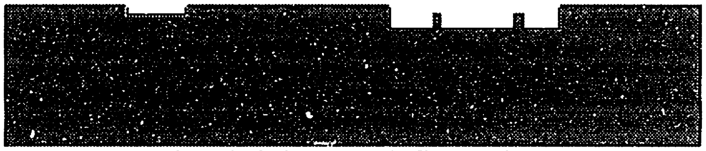
c) pattern and etch 3.8um to define valve seat

Figure 3-3: Valve seat definition

Finally, the valve seat is anisotropically etched in the silicon (Figure 3-3c) using the same recipe as above but at a higher power (100 W instead of 50 W) to decrease the etch time. The photoresist is again removed in a Piranha solution. The completed valve seat is shown in Figure 3-4 and Figure 3-5.

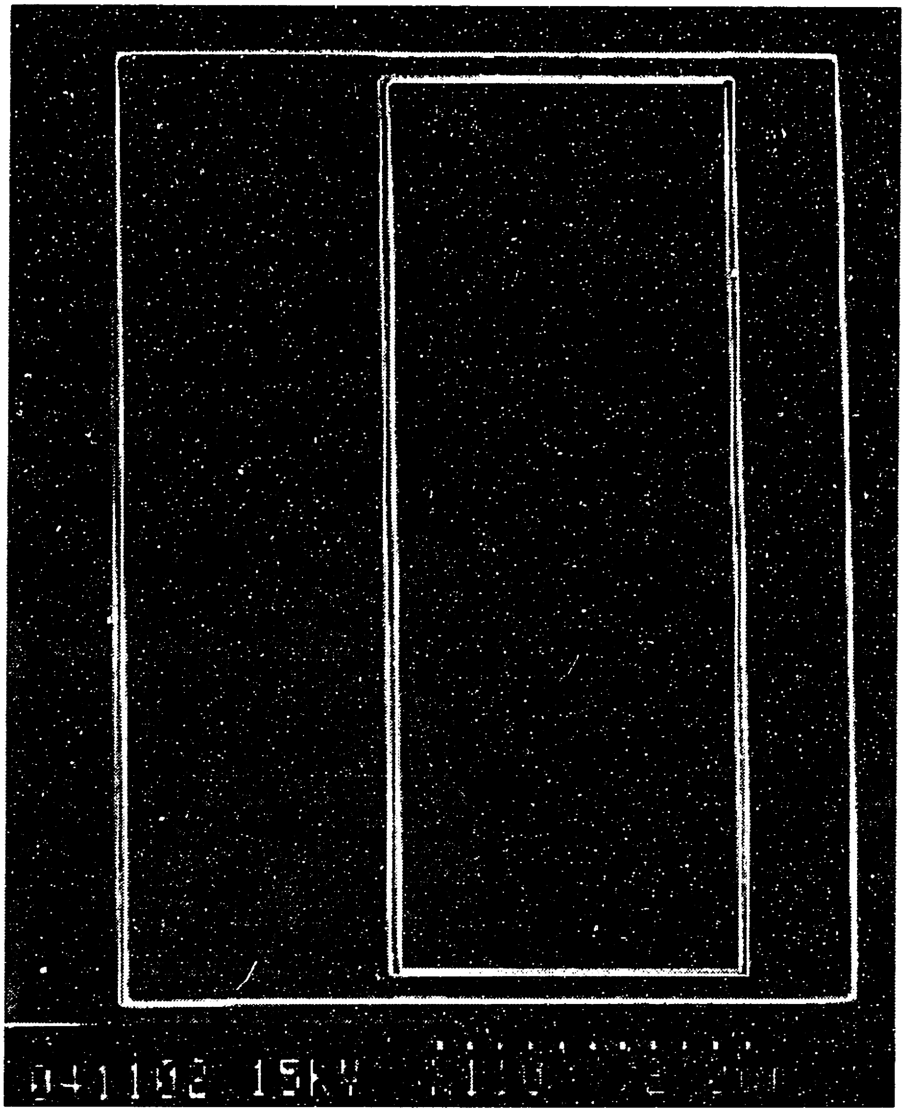

Figure 3-4: Valve seat - top view

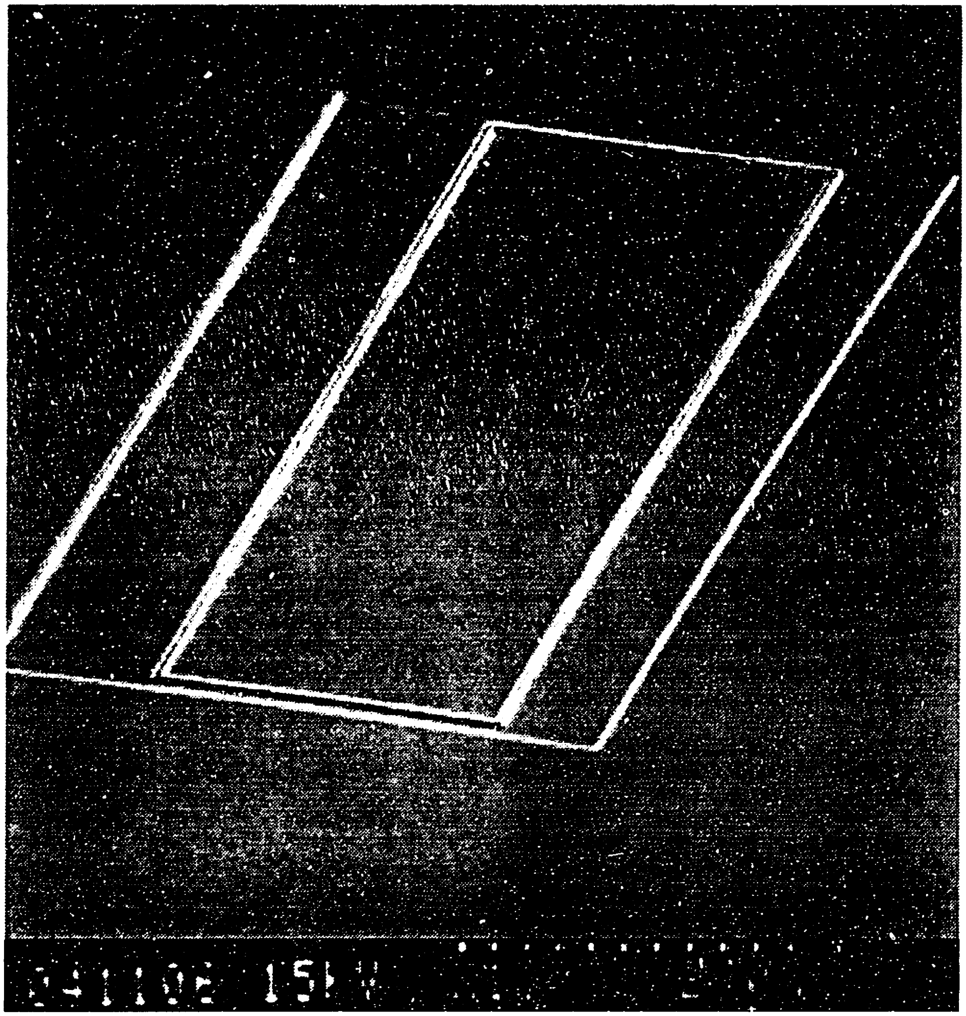

Figure 3-5: Valve seat - angled view

3.2.3 Port Hole Etch

This next process subsequence involves the use of KOH to etch the port holes. The process sequence is shown in Figure 3-6. KOH is an anisotropic etchant that etches the <111> crystallographic plane much slower than the <100> plane. It is used because it provides a nice balance between <111>/<100> selectivity, <100> etch rate, and Si/SiO_2 selectivity [57]. In addition, KOH has a perfect mask in SiN, which has no detectable etch rate in KOH. For all the following etches, a 20 % (by weight) solution of KOH in deionized water is used, with a small amount of surfactant (3M Corp.), typically 4 drops per liter, added to reduce the roughness of the etched surface. All etches are performed in a double bath configuration, with the KOH:H_2O solution being indirectly heated in a water bath.

The first step of this subsequence involves depositing 1500 Å of SiN (Figure 3-6a). Two different forms of SiN can be used, each with identical results. The first form is a stoichiometric LPCVD nitride. The second is a Si-rich low-stress nitride deposited in the presence of excess silane. Each nitride performs adequately, with a small pinhole density. Occasionally, a thin stress-relief oxide (SRO) is grown under the stoichiometric nitride to act as a stress-relief layer and as an etch stop during the nitride etch, but this is not necessary for process success.

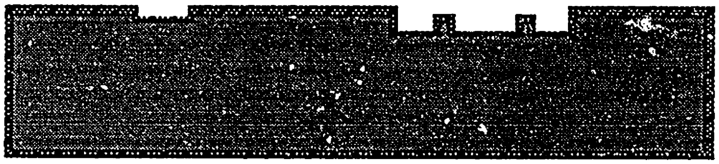

a) deposit with silicon nitride etch mask

b) pattern nitride to define port holes

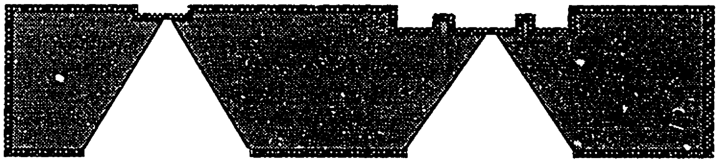

c) KOH etch port holes

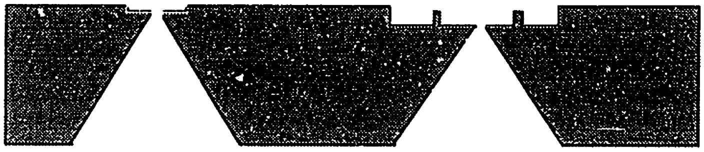

d) remove nitride mask in hot phosphoric acid

Figure 3-6: Port hole definition

After the nitride is deposited, a lithography step is used to define the port holes. This lithography step consists of first spinning a protective layer of standard photoresist on the frontside and then prebaking it for 10 min at 90 °C. This is followed by spinning a coat of AZ5214 (Hoechst) photoresist on the backside. This photoresist has the ability to perform an image-reversal process, whereby the photoresist changes from positive-tone to negative-tone via some processing steps [58] and without the mutagenic qualities of negative-tone photoresists. During the spinning, extra photoresist is applied to the edges of the wafer using a cotton swap to ensure that the edges are coated. The importance of this will be explained below. After the resist is spun and prebaked, the wafer is aligned and developed using the image-reversal process combined with infrared (IR) alignment. Infrared alignment utilizes the relative transparency of silicon at infrared wavelengths to allow imaging (and hence registration) of features on both sides of the wafer. This is accomplished with a simple IR light source and a IR-sensitive video camera. The image-reversal is used because it allows for the utilization of a clear-field mask with a positive-tone photoresist. This is vital because infrared alignment is a low-contrast process, and being able to see large parts of the wafer (a dark-field chrome mask would reflect most of the IR radiation) dramatically reduces alignment time. Using this technique alignment tolerances of approximately 5 μm are realizable. After alignment, the photoresist is developed in AZ 422 MIF developer and postbaked.

The port holes are etched through the SiN using an SF_6 plasma. A timed etch is used (as opposed to endpointing) because the total etched area is too small (~ 2% of the wafer) for endpointing and because overetching into the silicon is allowable; the silicon will itself be etched away in the very next step. The express coating of the edge of the wafer during the coating process (described in the previous paragraph) is used to diminish the occurrence of etched SiN on the edges, thereby preventing future etching of the silicon at the edge. Following this, the photoresist is stripped in a Piranha solution, leaving the device shown in Figure 3-6b.

The port holes are etched in the aforementioned KOH solution at 80 °C - 90 °C (Figure 3-6c). A 1.5 L solution is used and the wafers are etched in a one-sided etch jig, as shown in Figure 3-7. The one-sided jig is used to ensure the integrity of the frontside (by preventing pinhole-induced etch pits) and to protect the edges. Even though special care is taken to protect the edge, it is very difficult to maintain nitride coverage around the whole wafer. Any exposed silicon on the edge will be etched, causing "bites" to be taken from the edges, weakening the wafer dramatically. The one-sided etch jig is probably not needed to ensure process success, but it adds a safety measure to the process. The etch takes approximately four (90 °C) to eight (80 °C) hours. Prior to etching, the wafers are dipped in a dilute (~ 50:1) solution of H_2O:HF to clear the native oxide and the oxide grown from the Piranha solution used to strip the photoresist. An SEM of a port hole is shown in Figure 3-8.

A problem was observed with this process step. The port hole dimensions on the top of the wafer were significantly larger than expected. The calculated etched length and width for the reagent port holes on a 480 μm thick wafer (reprinted from Table 2-6), including a finite <111> etch rate, are given in Table 3-1.

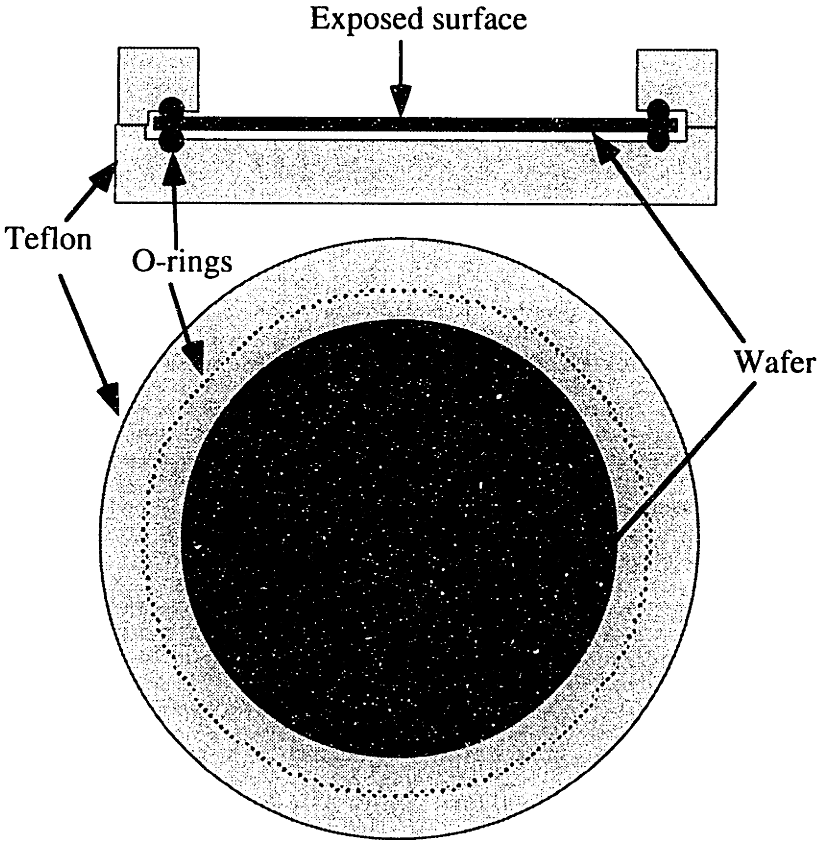

Figure 3-7: One-sided etch jig

Table 3-1: Calculated etched port hole dimensions

Design	L (μm)	W (μm)
1,2	610	20
3,4	810	20

The observed wafer thickness, measured using a calibrated z-stage and a differential interference objective was 480 μm. The measured port hole widths (measured with a calibrated x-y stage) were 69 μm, which is more than three times the calculated dimension.

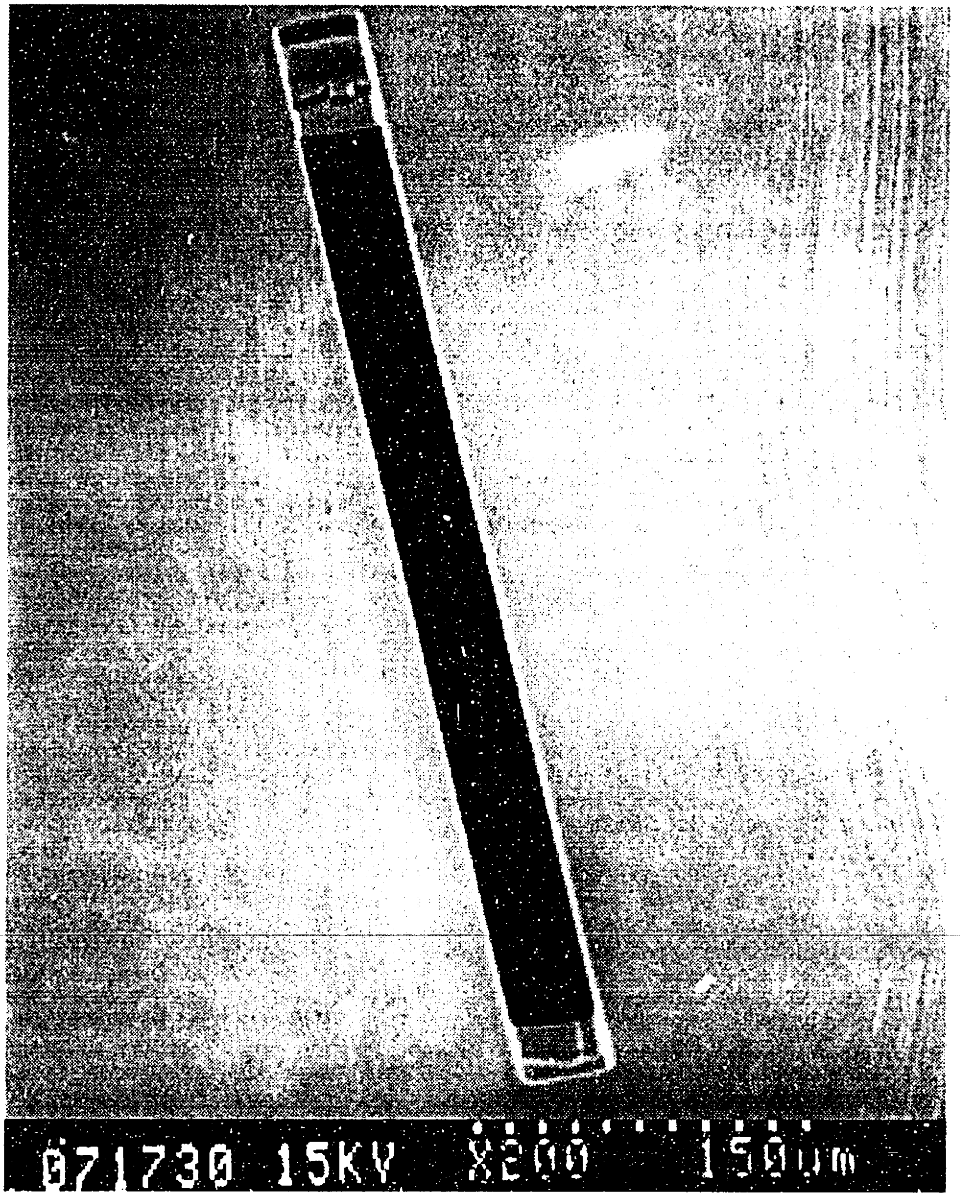

Figure 3-8: Port hole, angled view

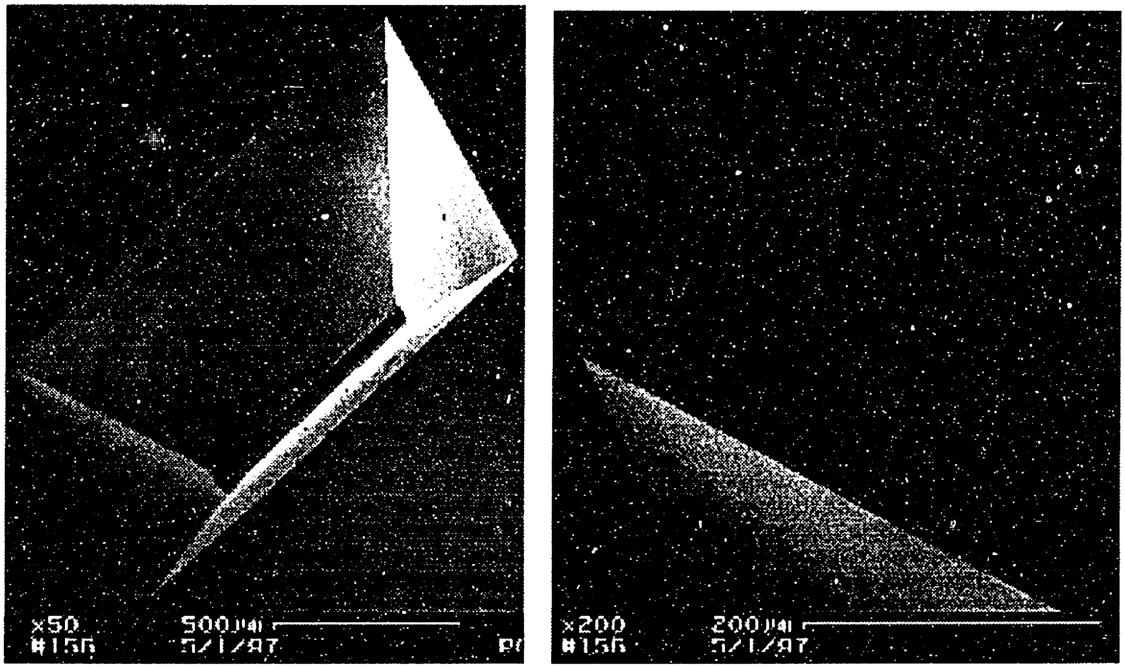

a) full port

b) closeup of corner

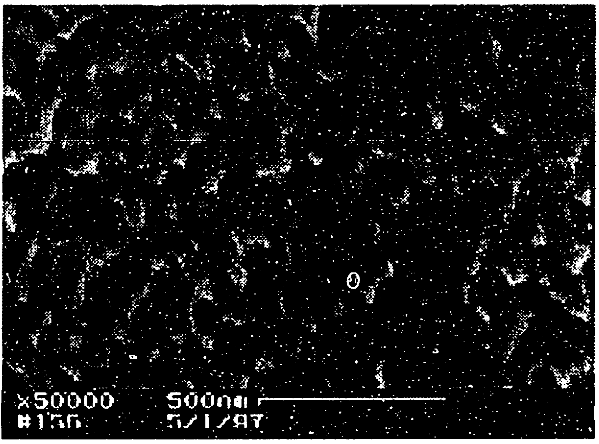

c) surface roughness

Figure 3-9: Backside of Port hole

The angle between the port holes and the valve seat was less than one degree, which means that a rotational misalignment is not to blame. The mask was also not at fault, since its dimensions are exactly as calculated. Another possible cause for the large features are oxidation-induced stacking faults (OISFs) [59], which result from oxygen impurities precipitating out of the silicon during high-temperature processing steps, causing defects in the silicon. If there were a great number present in the wafer then they would cause the KOH to preferentially etch them, irrespective of crystallographic orientation. The net result would be that the etch rate in all directions would increase, thereby reducing the selectivity between <111> and <100> and increasing the port hole dimensions. A consequence of OISFs would be that the surface of the etched sample would appear rough because of the etch pits produced. SEMs of the underside of a port hole are shown in Figure 3-9. The pictures show that the roughness of the sidewalls following the etch is approximately 100 nm, which is fairly smooth. While this points away from OISFs as the cause of the problem, it is by no means a definitive test. This is because the wafers are overetched approximately 5 to 10 minutes during the KOH etch which would smooth the OISF-induced roughness, thereby hiding the cause.

Following the KOH etch, the wafers are reintroduced to the cleanroom environment and the ionic contaminants (K^+, Na^+, etc.) encountered during KOH etching are removed in a multi-part cleaning procedure (see Appendix A). This clean allows the wafers to be introduced into high-temperature apparatus (diffusion furnaces) without fear of contamination.

The SiN is next removed from the wafer using a hot (180 °C) phosphoric acid bath for 40 minutes (Figure 3-6d).

3.2.4 Fusion Bond and Thin Back

The next step in the process is to fusion bond the handle wafer to the device wafer (Figure 3-10). The wafer pairs are prepared using an RCA clean. They are cleaned with the sides to be bonded facing each other. This helps protect the surfaces from particulates. The clean leaves the wafers particulate free with hydrophilic surfaces. The wafer pairs are contacted and the clean hydrophilic surfaces spontaneously bond. Viewing the wafers with an infrared camera, the wafers appear bonded and there are very few if any voids larger than 5 μm, which is the resolution of the camera system (Figure 3-11). This validates that the surfaces were particulate free during bonding. Following bonding, the wafers are annealed in an oxidizing ambient at 1100 °C for 70 minutes to complete the formation of the wafer bond. During this anneal, 1.1 μm of wet oxide is grown (Figure 3-10a).

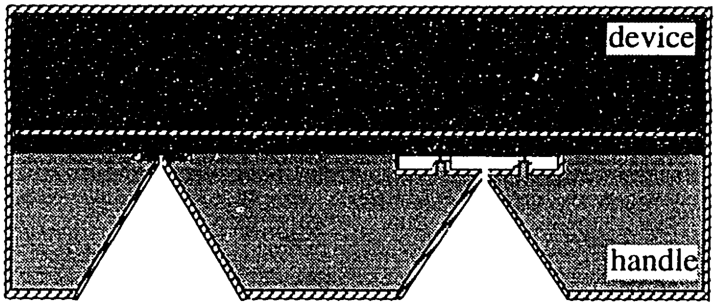

a) fusion bond and anneal

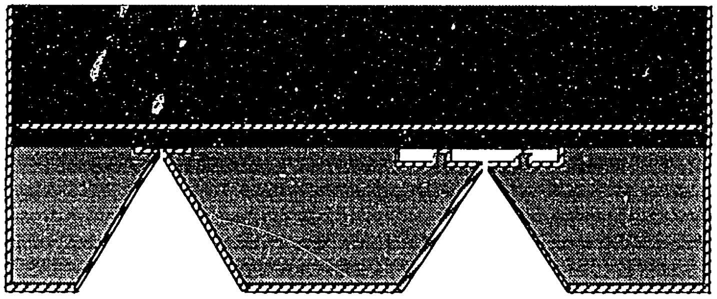

b) strip oxide off front of bonded pair

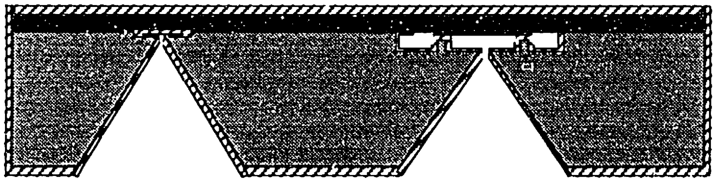

c) thin top wafer in KOH

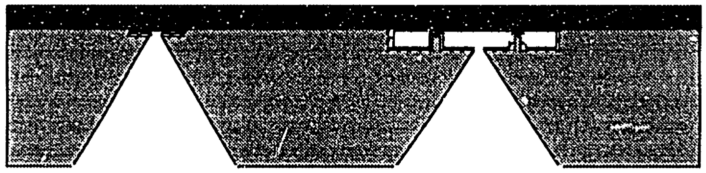

d) strip oxide from bonded pair

Figure 3-10: Bond and thin back:

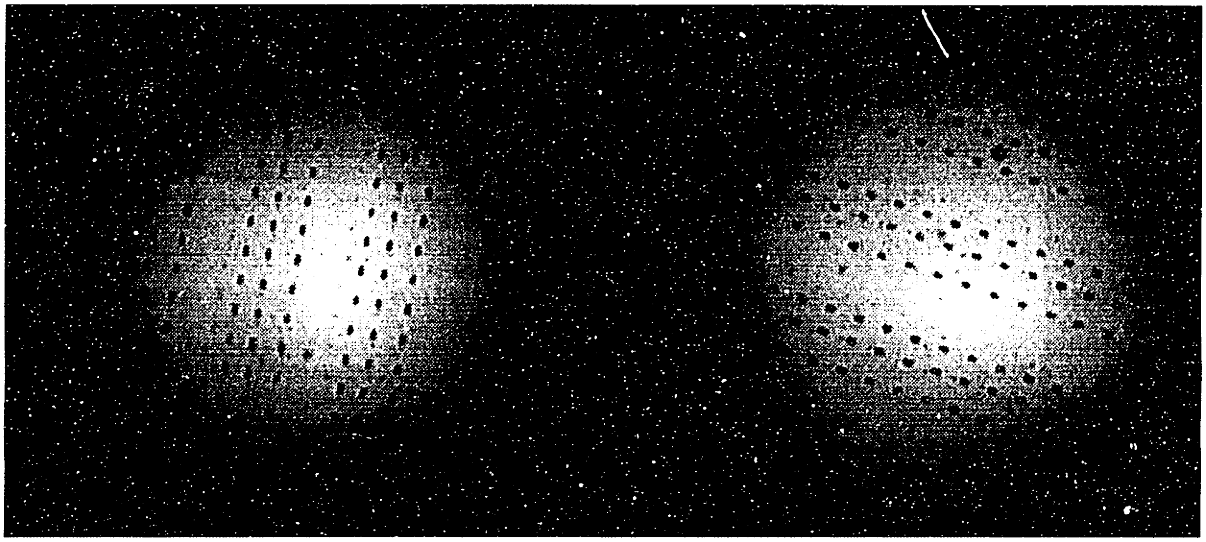

Figure 3-11: Bonding view

The next step is to remove the oxide from the exposed side of the device wafer (Figure 3-10b). This will allow the device wafer to be thinned in KOH. Since the exposed side of the handle wafer has port holes etched in it, it is not possible to use a normal photolithographic step to remove the device wafer oxide; this would introduce photoresist into the port holes, which would be very difficult (if not impossible) to remove, thus clogging the liquid mixer. Therefore, an HF vapor etch is performed. First, the edge and part of the bottom of the bonded pair are coated with standard photoresist using a cotton swab. The edge is coated for the same reason as it was prior to the SiN dry etch, and the bottom is coated to protect it from HF vapor. The photoresist is baked for 20 minutes at 120 °C to harden it. The bonded pairs are then place on top of a plastic beaker with approximately 200 mL of concentrated (49 %) HF, as shown in Figure 3-12. The wafer sits in the beaker so as to expose only one side to the etching vapor. The other side is not visibly etched in the apparatus, as evidenced by a lack of change in the oxide color. When the HF vapor has etched through the oxide, the surface dewets, thus terminating the etch. Etch times for removing the oxide are approximately 18 minutes. The photoresist is removed with a piranha clean.

Following the wafer thinning, the next step is to thin the device wafer to the buried oxide (Figure 3-10c), leaving a 10 μm thick silicon layer. Even though the 1.1 μm of oxide on the handle wafer should protect it during the thin-back step in KOH, a precautionary measure is adopted to ensure this. The one-sided etch jig cannot be used for this step, as it would leave a 500 μm thick ring of silicon around the edge of the wafer, preventing the completion of the process. A different one-sided etch process is used to circumvent this. The wafer is mounted on a glass mask plate (~ 3 mm thick) using caranuba wax. As depicted in Figure 3-13, the wax allows the wafer to adhere to the glass on one side, thus preventing that side from being exposed to the etching solution. In addition, the wax allows the other side to be fully exposed to the solution, thus preventing a silicon ring from forming. The wax is also viscous enough that is does not enter the port holes on the bottom side of the handle wafer.

After the wafer pair is attached to the glass, the pair is thinned in the KOH solution. Since the melting temperature of the caranuba wax is approximately 70 °C, the etching temperature is limited to around 60 °C. Hence, a (3L) bath of KOH at 60 °C is used. At this temperature, it takes approximately 20 - 24 hours to etch through the top wafer. Etch completion if verified by exposure of the buried oxide, which appears different than silicon.

Two wafers were sent sequentially through this step. The first wafer appeared to be etching correctly in the beginning (the wafer surface was bubbling), but after approximately 20 hours it became evident that only selected portions of the wafer were indeed etching. This left huge mesas covering approximately 50 percent of the wafer surface. The mesas were a dull grayish color, unlike anything expected in a silicon etch such as this. Upon closer examination, the mesas appeared to be composed primarily of <111> and higher-order planes. It was hypothesized that there was an electrochemical effect occurring between the silicon surface and the metal bath causing the silicon surface to passivate.

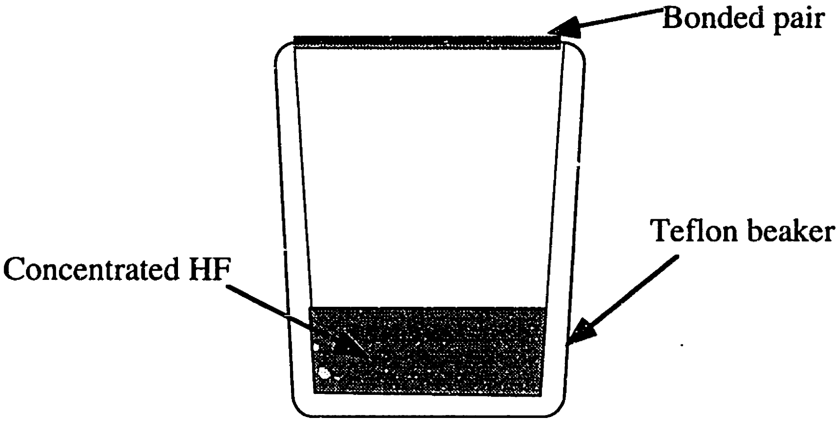

Figure 3-12: HF vapor etch jig

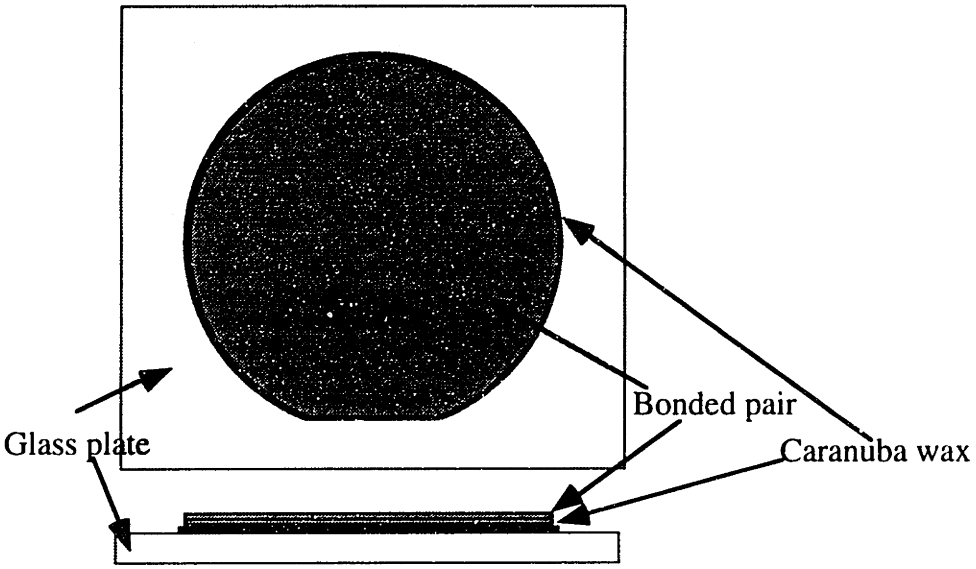

Figure 3-13: Caranuba wax one-sided etch jig

To counter this, the second wafer was etched in a plastic bath to electrically isolate it from interactions. After an hour of etching, the silicon surface started turning a dull gray again and etching stopped near the edges. This led to the hypothesis that there was something on the silicon surface that was masking the etch. To counteract this possible phenomenon, a Piranha clean was performed to remove any organics from the surface. This was followed by a dilute HF dip until the front dewetted (to indicate removal of all surface oxide). This was itself followed by pre-etching of the surface with a solution of 20:1:1 HNO_3:HF:HAc silicon etchant [60,61] four times for one minute each to remove the top layer of silicon. After reimmersal of the wafer into the KOH bath, etching seemed to proceed uniformly over the wafer surface. After approximately 20 hours, the majority of the wafer had cleared, except for two small ridges approximately 60 μm high near the edge of the wafer. These were removed by repeated etching of the ridges with the aforementioned silicon etchant and using the buried oxide as a mask to protect the rest of the wafer. After this was complete, there was one ridge approximately 10 μm high remaining.

Following the thin back, a clean is undertaken to reintroduce the wafers to the cleanroom environment. Lastly, a 12 minute buffered oxide etch (BOE) is performed (Figure 3-10d) to remove the implanted oxide remaining and to remove the masking oxide on the handle wafer.

3.2.5 Cantilever-Plate Definition

The final process subsequence for the silicon bonded pair is to define and etch the plate and open the port holes to the top surface (Figure 3-14). First, an infrared alignment (IR) lithography step is used to define the plate and port holes. IR alignment is needed to be able to register the alignment marks from the top of the handle wafer to the top of the silicon overlayer. The second step is a silicon plasma etch (Figure 3-14a) similar to the valve seat etch, again at 100 W (see Appendix A). Due to area-dependent etch rates, the silicon etches faster at the end of the plate (40 μm wide) compared to the edges of the plate (10 μm wide). This prevents the etch from terminating uniformly, leaving the end of the plate free with the edges still attached. Luckily, the BOE etch performed earlier (Figure 3-10d) did not remove the oxide under the plate, due to either bubble formation or etchant loading effects. This means that it is possible to overetch without fear of ruining the underlying silicon because the oxide will protect it. Released plates can be identified under Nomarski differential-interference contrast (DIC) microscopy, as the stress induced by the oxide underneath causes the plates to bend upwards. At this point, the yield is approximately 73 %, with yield being defined as the percentage of released plates. SEMs of the released plates are shown Figure 3-15 and Figure 3-16. Oxide can be seen hanging from the underside of the plates.

The remaining oxide is removed with an 11 minute BOE etch (Figure 3-14). SEMs of the completed plates are shown in Figure 3-17 and Figure 3-18. The oxide lip is gone from the edge of the plate. The plate is still upturned slightly (~ 5-10 μm), meaning that some oxide is left near the underside of the plate. This should not impair the function of the mixer.

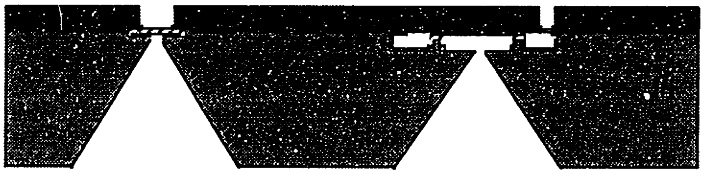

a) etch cantilever plate and open thru-holes

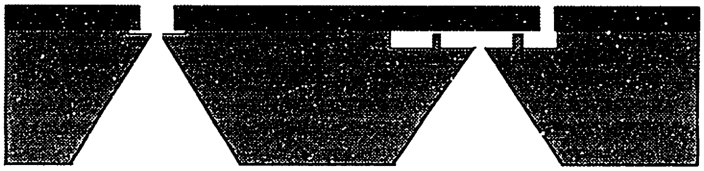

b) strip remaining oxide

Figure 3-14: Cantilever-plate definition

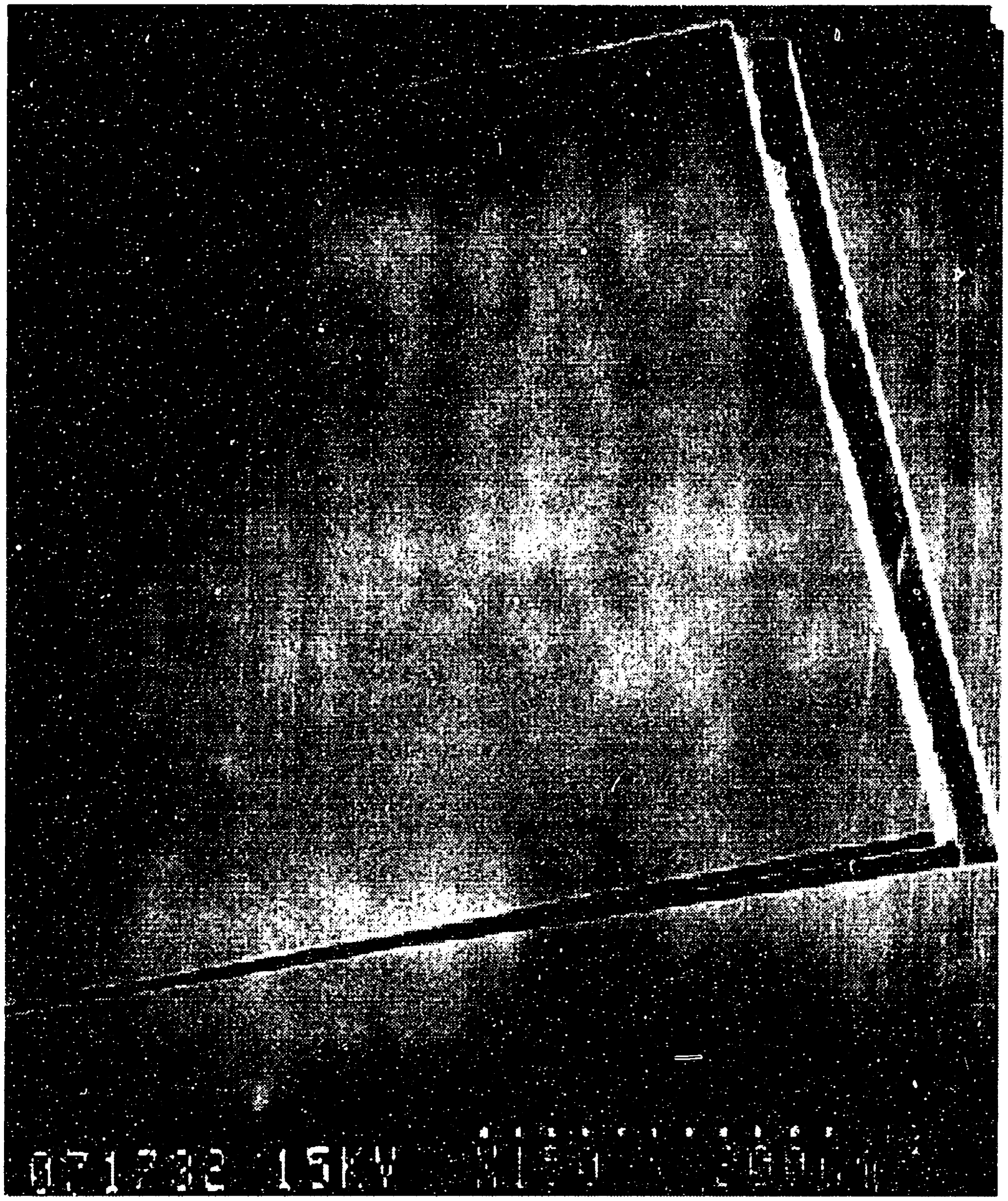

Figure 3-15: Cantilever-plate - before final oxide etch

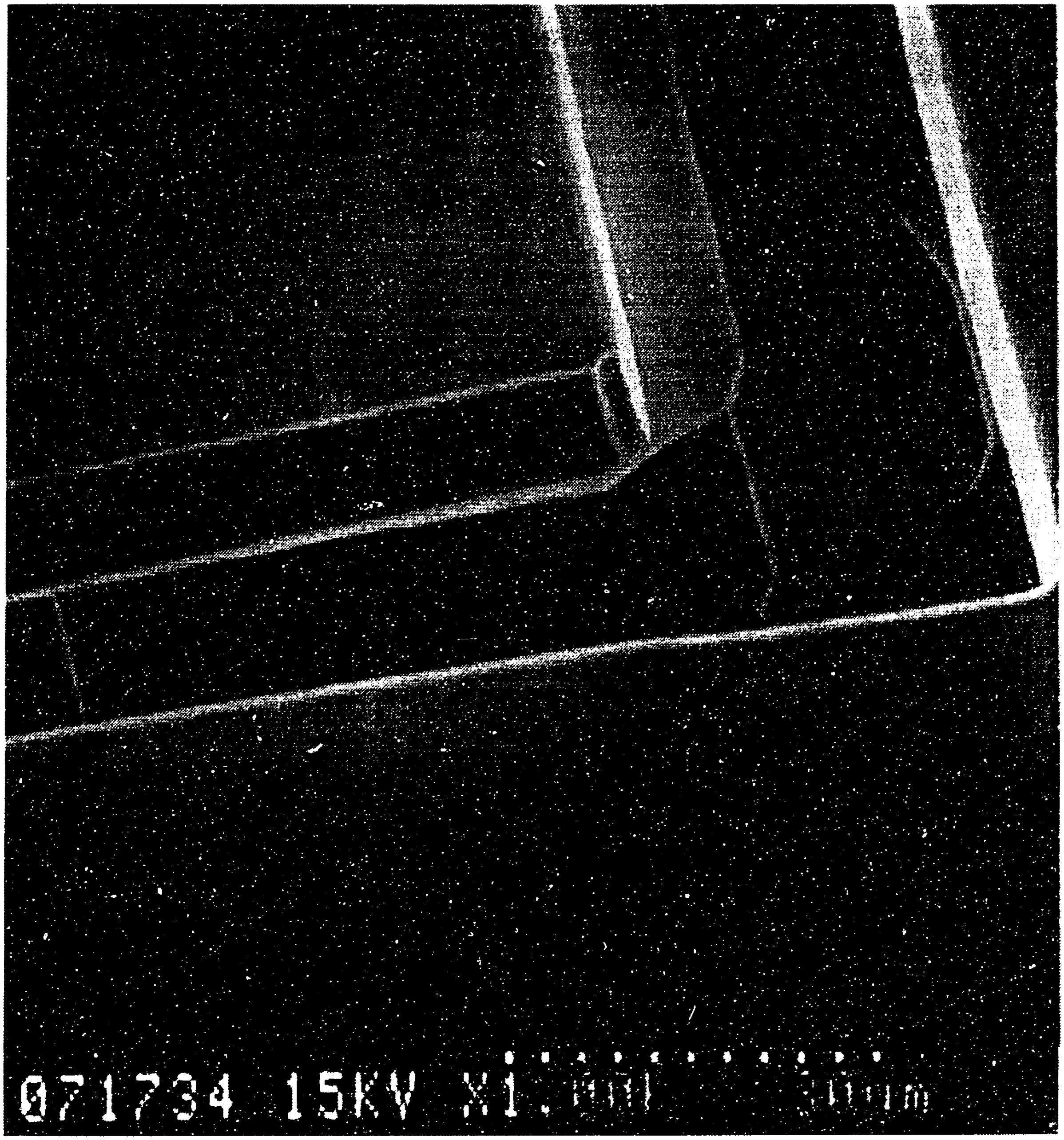

Figure 3-16: Cantilever-plate closeup showing oxide hanging from plate

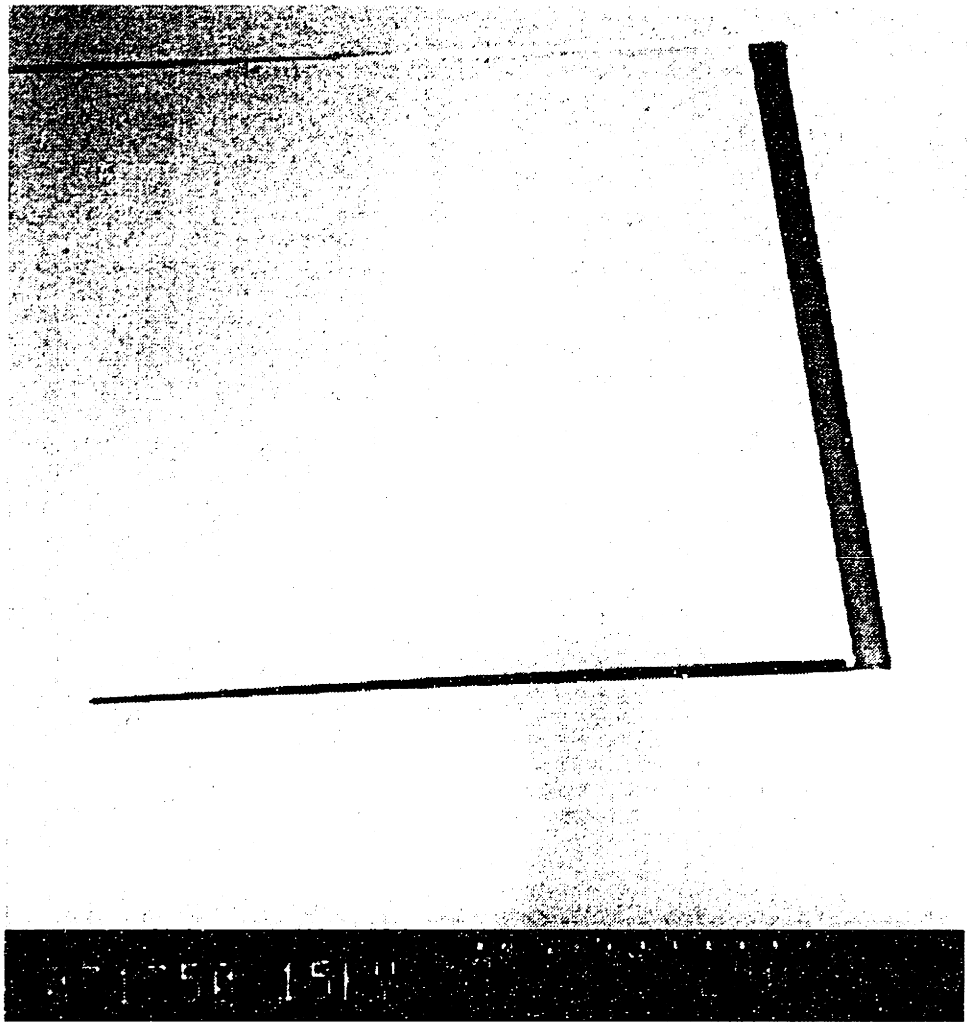

Figure 3-17: Cantilever-plate - final structure

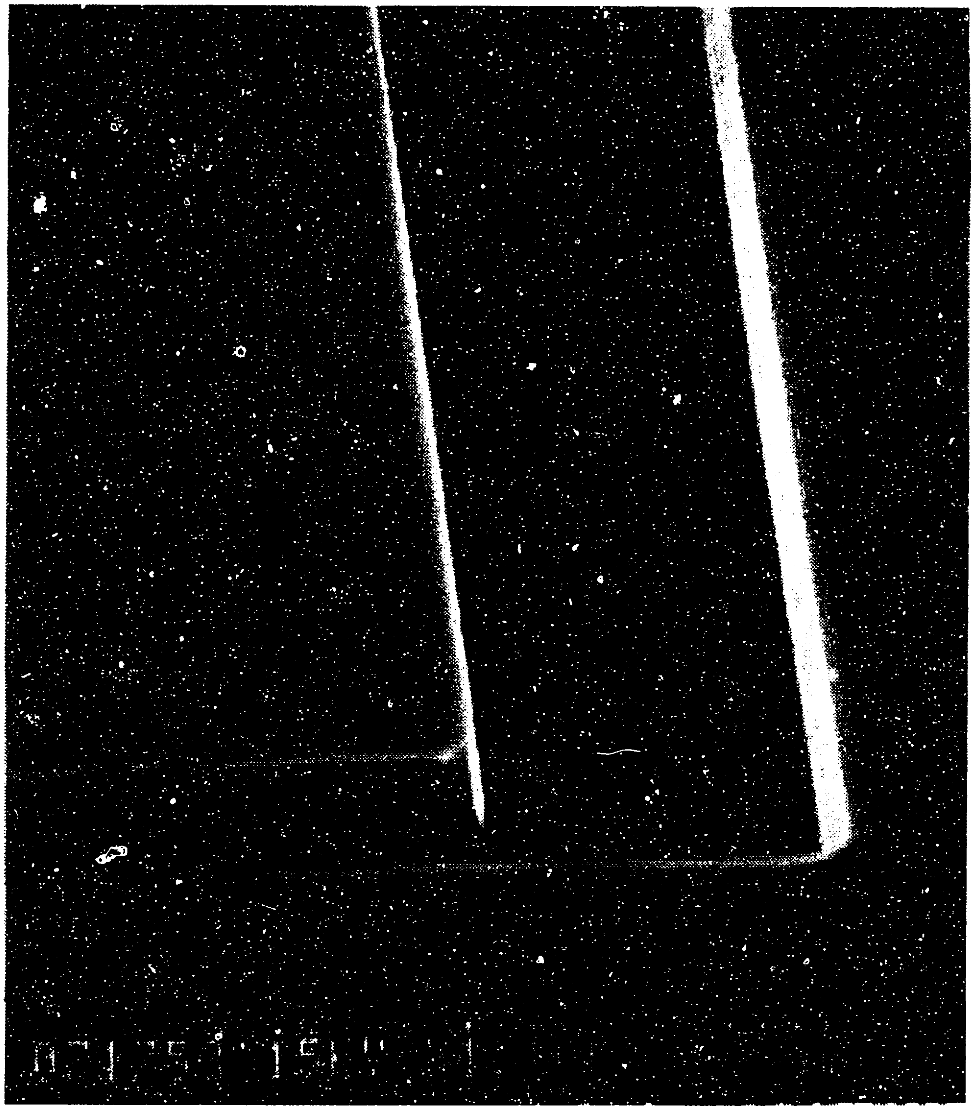

Figure 3-18: Cantilever-plate closeup - final structure

3.3 Glass Channel Etching

The glass etch subsequence involves the deposition of a masking material and its subsequent patterning, followed by etching of the glass. Etching the flow channels in the glass, while conceptually a simple problem, involves much characterization and process development. Care must be taken in the choice of masking material and etchant.

The are several requirements for the glass etching process. First, the process must be reproducible and controllable. The glass etch rate should not be too fast, or it will be difficult to control, nor too slow, or it will take too long. The bottom surface of the channels should be smooth, to minimize inhomogeneities in the flow. The sidewalls should be relatively free of defects and "bites" so that the channel width (and hence the local velocity field) remains constant.

The glass used for the flow channels is Corning 7740 glass, manufactured by Mooney Precision Glass [62] into four inch 500 µm thick wafers with a single flat. Corning 7740 glass is a borosilicate glass consisting of an SiO_2 network modified with various concentrations of B_2O_3, Na_2O, Al_2O_3, and K_2O [63,64,65]. Corning 7740 glass is used for several reasons. First, it has a relatively low overall concentration of mobile ions. This eases its introduction into the cleanroom environment. Because of it's mobile ions, though, it is not allowed in any high-temperature processing steps. Second, the mobile ions present in the glass allow it to be anodically bonded to the silicon, as described below. Third, the thermal expansion coefficient of Corning 7740 glass is relatively-well matched to that of silicon in the range from 300 to 400 °C, allowing anodic bonding without severe stress resulting. Fourth, the glass autofluorescences very little.

The choice of masking material and the conditions used to deposit it are perhaps the most crucial step of all. Several masking materials are potential candidates. The ideal mask would be single-crystal Si (c-Si), since silicon adheres well to glass and there are etchants which exhibit high selectivity between glass and silicon. While c-Si is ideal, it is difficult to implement in practice, since an amorphous substrate (glass) is being used. The next best mask is polysilicon, which adheres well to glass and is not etched in HF-based solutions (except at the grain boundaries) which etch glass. Unfortunately, deposition of polysilicon involves temperature ranges of 600 to 700 °C, which is not allowable for the glass, as explained above. Amorphous silicon is another possibility, and has been used by [66] as a mask to etch 20 µm channels in glass. Amorphous silicon was not attempted in this thesis. The final masking material candidate is a multlilayer metal film. The top layer serves as the etch mask, while the bottom layer serves as an adhesion layer between the top layer and the glass. In this thesis, a three-level mask is used. The process is similar to others reported elsewhere [28]. The bottom layer consists of 200 Å of chrome, topped by 2000 Å of gold, and capped by 1 µm of photoresist. The chrome serves as an adhesion intermediary between the gold and glass. The gold serves as the main masking material, having no etch rate in HF-based solutions and no native oxide. The photoresist serves as a masking material in the field, covering pinholes in the gold.

The integrity of the mask can be severely affected by the presence of surface organics on the glass wafer, destroying the adhesion between the chrome and the glass. There are several good references [67, 68, 69, 70] on the importance of clean glass surfaces for adhesion. From these references and experimentation, a three-part clean is undertaken. First, the glass wafers are detergent cleaned (Alconox) in a non-cleanroom environment to remove gross organics. Immediately following this, the wafers are Piranha cleaned in a cleanroom environment, to remove any remaining organics and particulates. Immediately following this, the wafers are placed in a UV-ozone cleaner, which uses ultraviolet light to generate O_3 radicals which react with organics on the surface of the wafer, forming vapor-phase products. Immediately following the UV-ozone clean, the wafers are placed under vacuum in the masking material deposition system. While the cleaning procedure may appear excessive, its validity has been proven, as samples etched with the three-part clean have smoother sidewalls (better adhesion) than those cleaned without the full three-part clean.

Figure 3-19 shows the glass etching process. The masking material is deposited (Figure 3-19a) under high vacuum (5e-7 torr) in an electron-beam deposition system. The chrome is deposited followed by the gold without breaking vacuum, which would allow a layer of chromium oxide (CrO) to form on the chrome surface, which would get etched in the glass etching solutions. Additional parameters are shown in Appendix A.

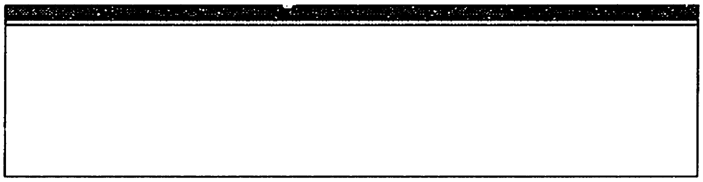

a) deposit metal mask

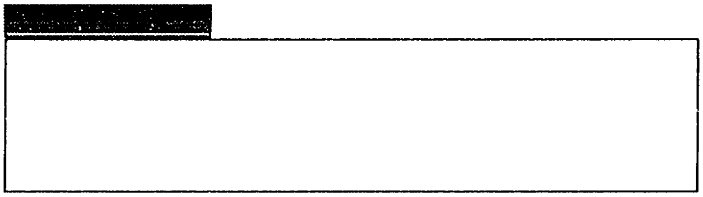

b) deposit andpattern photoresist

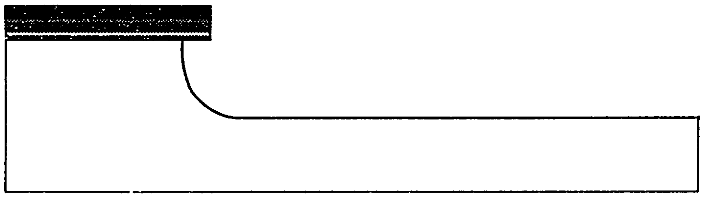

c) etch channels in glass

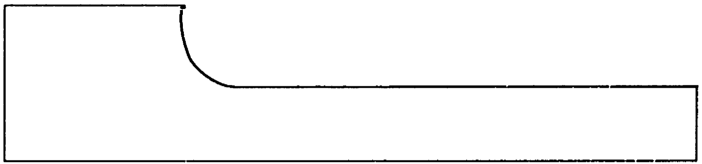

d) remove masking materials

Figure 3-19: Glass etching process

After the metal bilayer is deposited, standard photolithography is performed on the wafer (Figure 3-19b). The gold is etched in an aqua regia solution (3:1 HNO_3:HCl) for approximately 15 secs, until the chrome is visible underneath. Since aqua regia etches gold very quickly (15-30 µm/min), it is important to remove the wafer precisely when etching has completed, or else severe lateral underetching of the gold film may occur. A better solution would be to use a dilute solution of aqua regia (H_2O:HNO_3:HCl 10:1:8), but this was not used. The photoresist remains intact through this step, even in the presence of the nitric acid, most likely because the etch time is very short. The chrome is not etched in aqua regia.

Following the gold etching, the chrome is etched in CR7, a commercial chromium etchant. The 200 Å etches in approximately 20 secs. The CR7 does not appear to attack the gold or the photoresist on this timescale. After etching the chrome, a three-layer masking material is left (Figure 3-19b).

The next step is to etch the channel in the glass (Figure 3-19c). First, a glass etchant must be chosen. Plasma etching has been attempted by some groups [71, 72, 73], but has had poor success because of its slow etch rate (<1000 Å/min) and its inability to produce vapor-phase products of the impurities in the glass. All wet chemical etches of glass involve HF-based chemistries. Several papers describe the dissolution mechanics of various glasses in HF-based etchants. Good reviews are given in [74] and [75]. From these papers, and by experiment, several etchants were investigated. Dilutions of H_2O:HF were attempted, but these etch the glass poorly and peel the photoresist (Figure 3-20). BOE etches too slowly (0.1 µm/min). The etchant chosen is a solution of 66:14:20 H_2O:HF:HNO_3. The nitric acid leaches out the impurities in the glass, leaving a pure SiO_2 network which is etched by the HF. The H_2O:HF:HNO_3 solution etches at a reasonable rate (0.7 -0.8 µm/min) and does not peel the photoresist. The etchant has also been used by other researchers with success [75,28].

SEMs of glass cleaned with the three-part clean, masked with the three-layer mask, and etched with the three-part etchant are shown in Figure 3-21 and Figure 3-22. Although relatively clean, the sidewalls still suffer from occasional "bites". This is similar to a situation encountered by Harrison's group at the University of Alberta where they encountered poorly etched glass with many "bites" in the sidewalls, although their problem was much worse [28]. Their solution was to anneal the glass at 570 °C which, according to them, removed mechanical stresses which occurred during the polishing process. They obtained final results which look better than the SEMs shown here. It cannot be ascertained, though, if the annealing process actually removed mechanical stresses, or if the annealing process induced a different change such as removing microcracks [74] or inducing a phase separation [63,76]. Annealing was not attempted in this thesis.

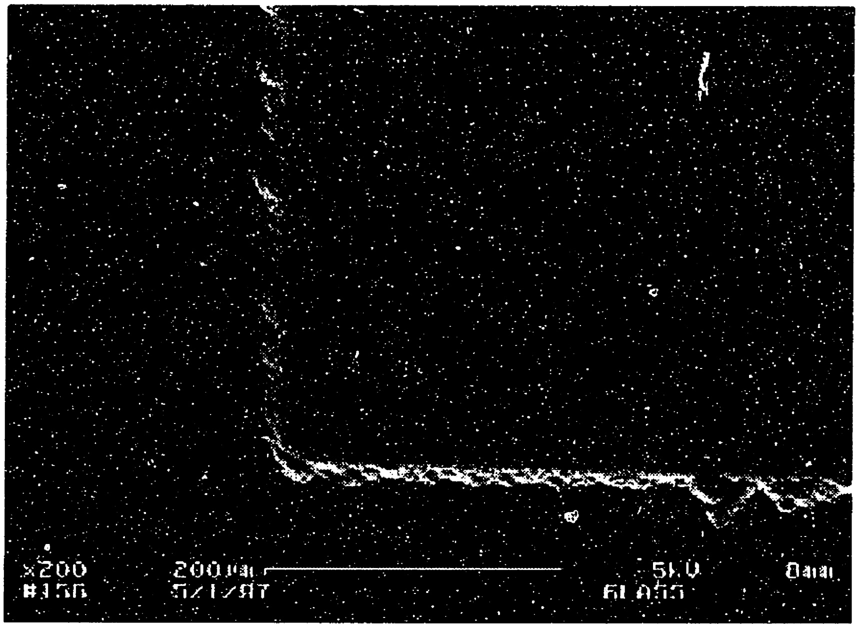

a) HF:HNO_3:HAc

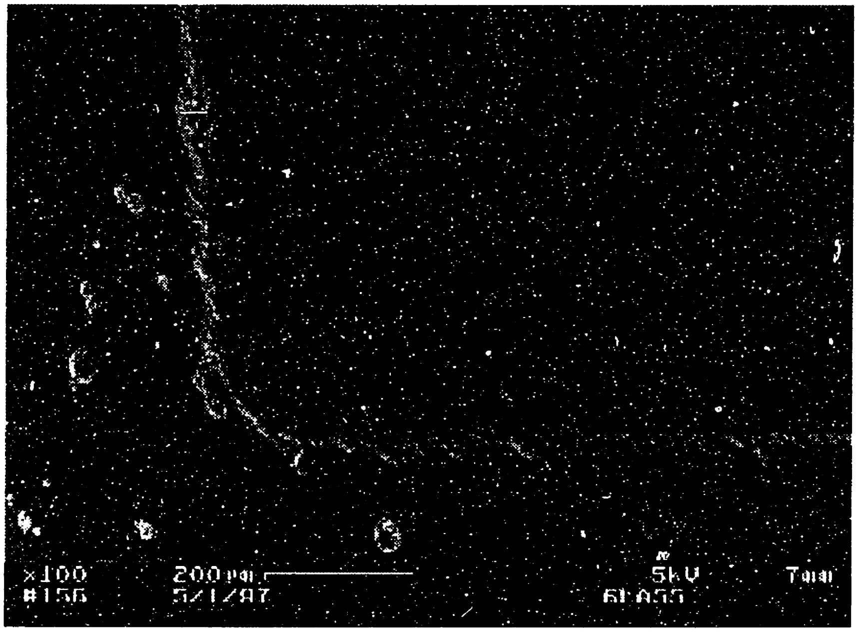

b) HF:H_2O

Figure 3-20: Glass etched under 2 different conditions

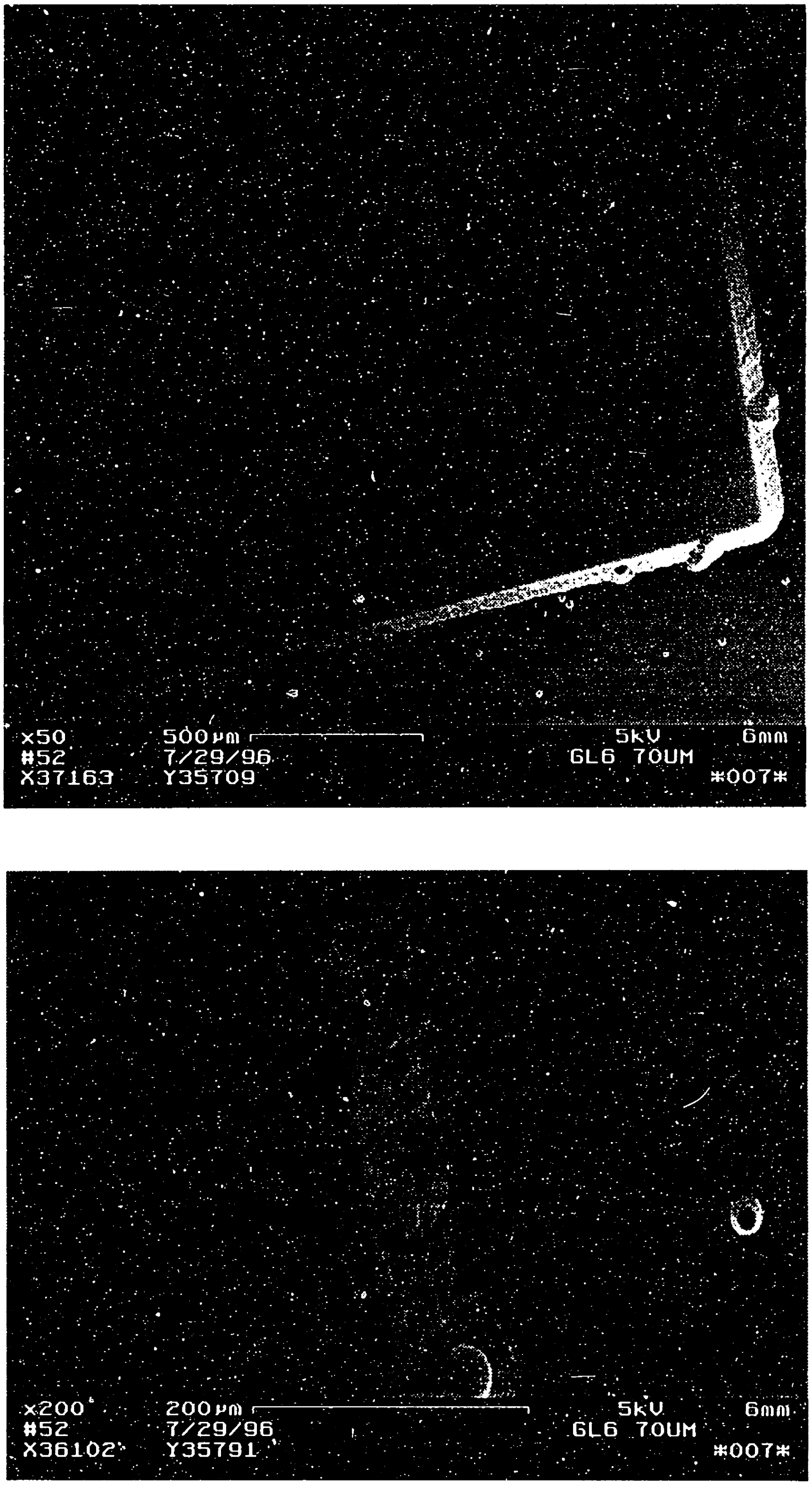

Figure 3-21: Glass etched under final conditions

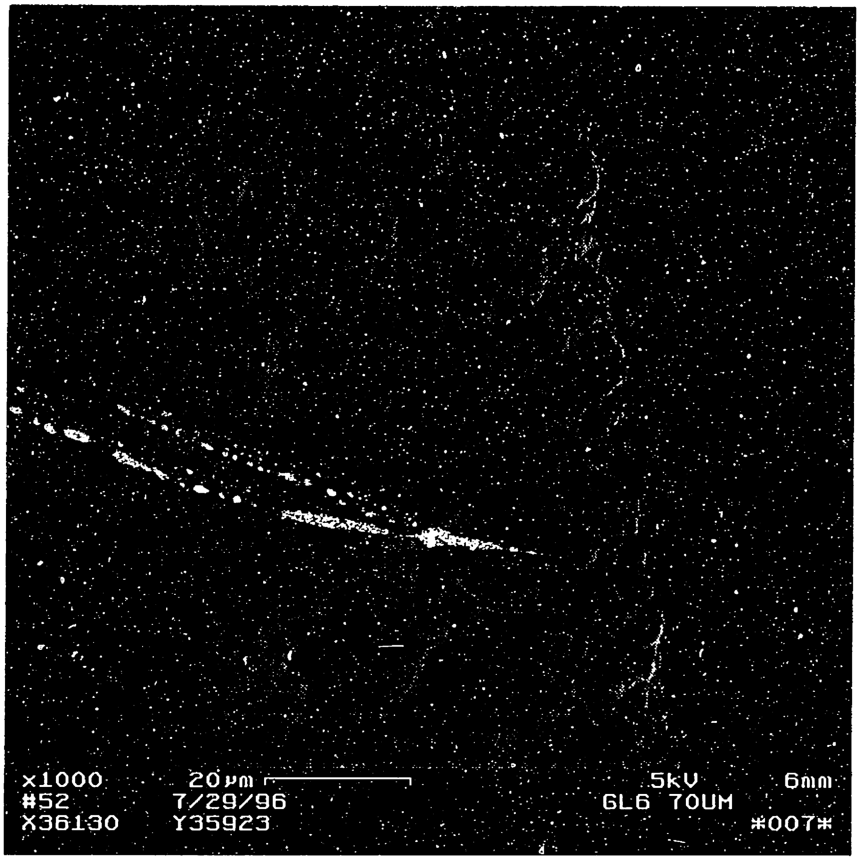

Figure 3-22: Glass etched under final conditions

Etching the glass takes around 120 minutes, because loading effects diminish the etch rate over time. The glass is etched with the features facing upwards, to prevent bubble trapping, and with the solution stirred, to improve uniformity. The wafers used in this process were not masked on the backside, which resulted in an enhanced loading effect and resulted in thin wafers (~ 400 µm). It would be wise in the future to mask the backside to prevent this from happening. The etch depths and dimensions were verified using an xyz-axis micrometer-equipped microscope. The results are

Table 3-2: Etched glass dimensions

Parameter	Wafer #1	Wafer #2	Wafer #3
Width of nominal 800 µm channel	851 µm	841 µm	839 µm
Width of nominal 1000 µm channel	1052 µm	1041 µm	1038 µm
Depth of channel	75 µm	71 µm	70 µm

These results indicate an anisotropy of 1.2 to 1.3, which is fairly close to isotropic and indicates relatively little mask pealing.

Following the glass etch, the masking layers are stripped in appropriate etchants (Figure 3-19d), and the wafers are ready for anodic bonding.

3.4 Anodic Bond and Diesaw

The final subsequence in the fabrication process is to anodically bond the glass and silicon wafer and diesaw them into chips. Anodic bonding is a process used since the 1960's [77] to form a hermetic seal between silicon and glass. Anodic bonding involves taking a glass and a silicon wafer, heating them up, and applying pressure and voltage across them. The heat increases the mobility of the ions in the glass, which move under the applied electric field into the silicon. This leaves a negatively charged layer in the glass and a positively charged layer in the silicon, as seen in Figure 3-23. This electric field helps keep the silicon and glass bonded. In addition, the heat causes a small layer of SiO_2 to grow between the glass and the silicon, aiding in the bonding process. These two factors result in a non-reversible bond between the silicon and the glass. The pressure applied helps to overcome any surface roughness and general non-planarity in the surfaces. Choice of temperature and pressure can be optimized [78] to achieve the desired bond.

Before the wafers are bonded, a piranha clean is performed to remove organics and gross particulates from the surfaces of both wafers. The wafers are placed facing each other in 25-wafer carriers until bonding to minimize air flow and hence particulate introduction.

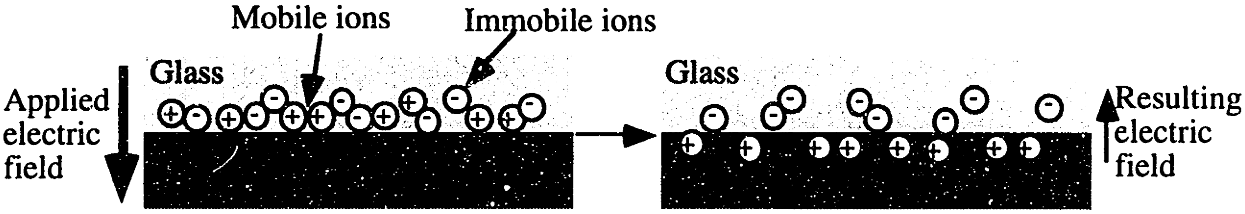

Figure 3-23: Anodic bonding mechanism

For this process, an aligned anodic bond is needed, because the channels in the glass wafer must be precisely aligned to the cantilever-plate and holes in the silicon wafer. The preferred way to do this bonding is using an aligner-bonder setup, such as the EV-450 (Electronic Visions, Inc.). The EV-450 first aligns the silicon wafer to machine alignment marks, then aligns the glass wafer to those same marks, indirectly aligning the wafers to each other. The wafers are then carried in a cassette to an anodic bonding setup which applies temperature, pressure, and voltage according to specifications. Alignment tolerances of 5 μm are quoted by the manufacturer. Unfortunately, this tool could not be used for this process because the aligned section requires that no through-holes be placed within 10 mm of the wafer edge (to be able to apply vacuum to the wafer), and the silicon wafer had through-holes (port holes) within 10 mm of the edge.

In order to align the two wafers, a jig fabricated by Howard Goldberg is (Figure 3-24). The jig fits into the standard photolithographic aligner as a mask would. A glass wafer is put into the jig and standard alignment can be performed. Once contact is made, the vacuum can be turned off, and the glass and silicon wafers will stay in intimate contact. A problem encountered in using this setup is that the vacuum applied to the silicon wafer during alignment will go through the port holes and suck the glass wafer onto the silicon wafer, thus preventing alignment. To counteract this, a scheme is implemented whereby a test silicon wafer is put face down on the standard chuck. A small amount of water is put on this wafer, and the device wafer is placed on top. Using this scheme, the vacuum holds the test wafer to the chuck, and the water holds the bonded pair (through capillary forces) onto the test wafer. This allows alignment to proceed. Additionally, a small amount of UV curable epoxy is put onto the silicon device wafer. After the silicon and glass are aligned and contacted, the wafer pair is exposed to ultraviolet light from the aligner for 220 seconds which cures the epoxy. The prevents the wafer pair from moving out of alignment during subsequent handling.

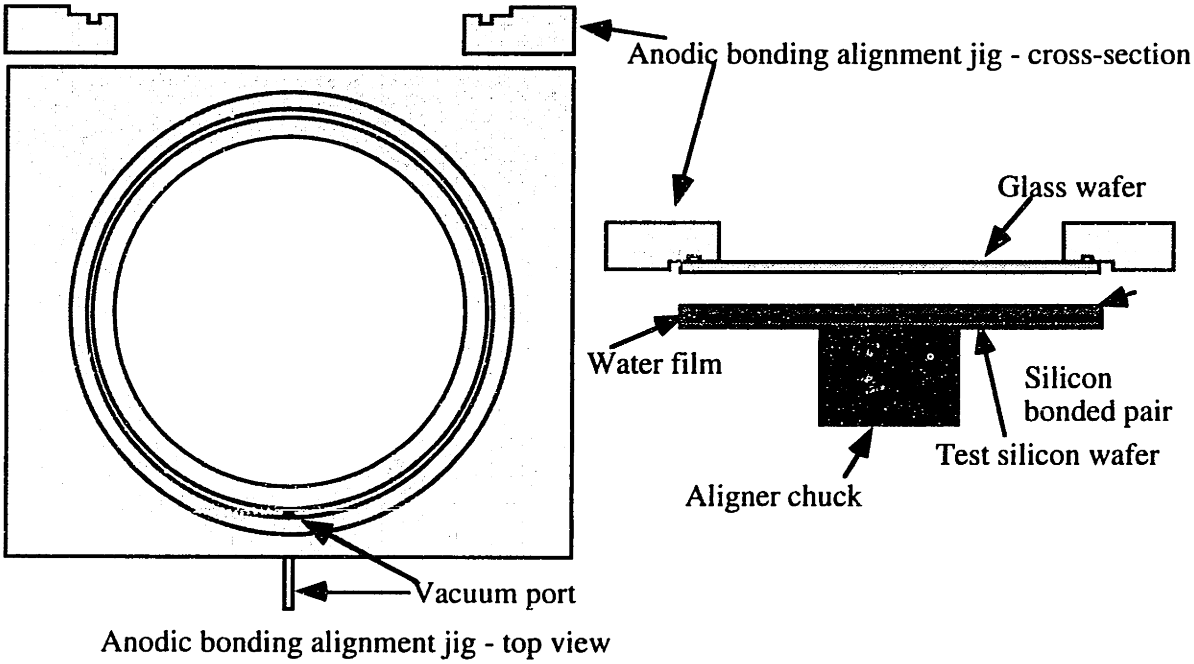

Figure 3-24: Anodic bonding alignment jig

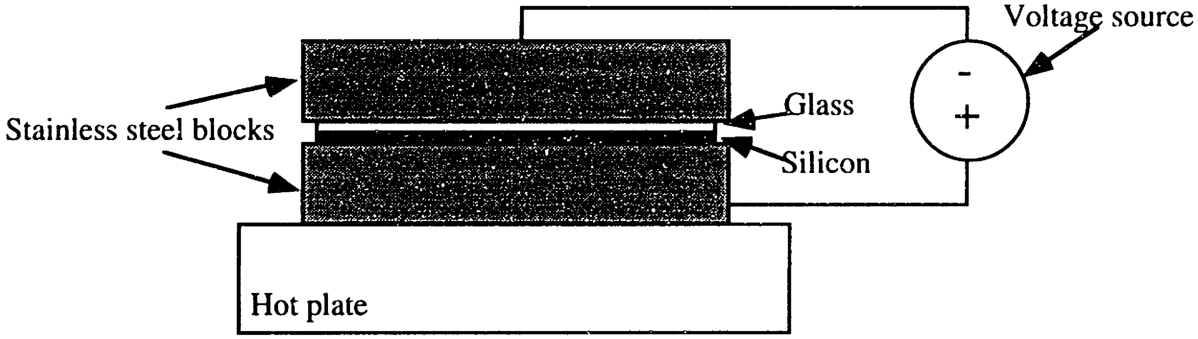

Figure 3-25: Anodic bonding jig

After being aligned, the glass/silicon pair is carefully put into the anodic bonding fixture and placed into the AB1 (Electronic Visions, Inc.) anodic bonding unit. An anodic bond is performed (see Appendix A for specifications). Unfortunately, the anodic bonding unit uses a needle electrode which does not apply an uniform field across the wafer. This prevents the whole wafer pair from bonding, leaving only about a 3x3 cm^2 bonded area. To bond the whole wafer pair, a plate electrode setup shown in Figure 3-25 is used. Using similar parameters as the previous bond attempt the wafers fully bond.

The final step in the process is to diesaw the wafers into chips. This is accomplished using a standard diesaw machine. During this step, the glass layer on a significant number of chips cracked as the diesaw passed. A previous anodically bonded test pair diesawed under the same conditions did not experience this cracking effect. This means that the process probably induced significant stress in the glass/silicon structure which was relieved during diesaw. The cause is probably a conglomeration of factors, including relatively high-anodic-bonding temperatures, weakness in the glass due to microcracks from etching and an overall thin glass structure due to one-sided masking, accentuated by a relatively fast diesaw speed. These factors can all be addressed in future implementations.

SEMs of the completed device are shown below.

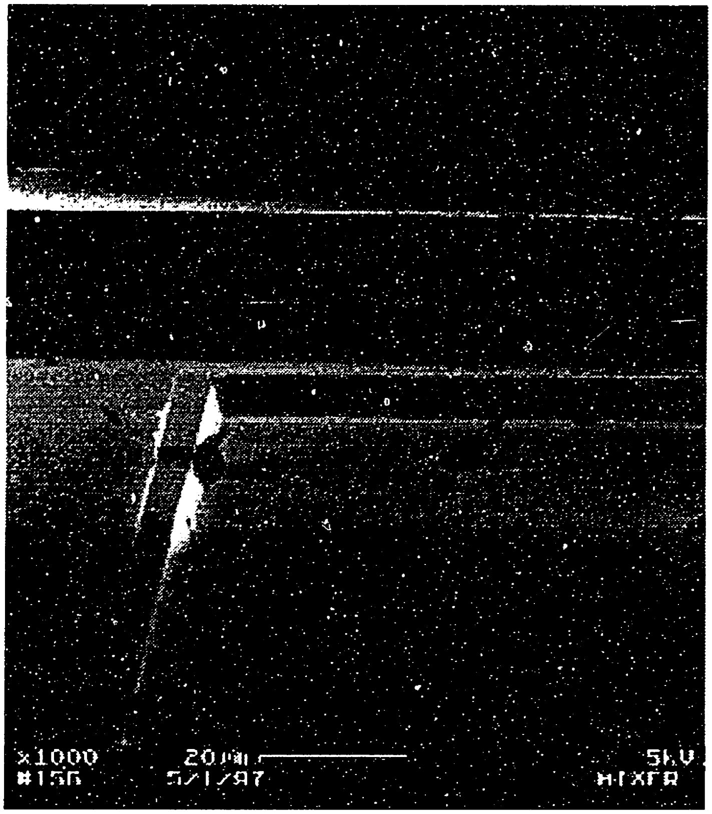

Figure 3-26: Closeup of flapper valve area

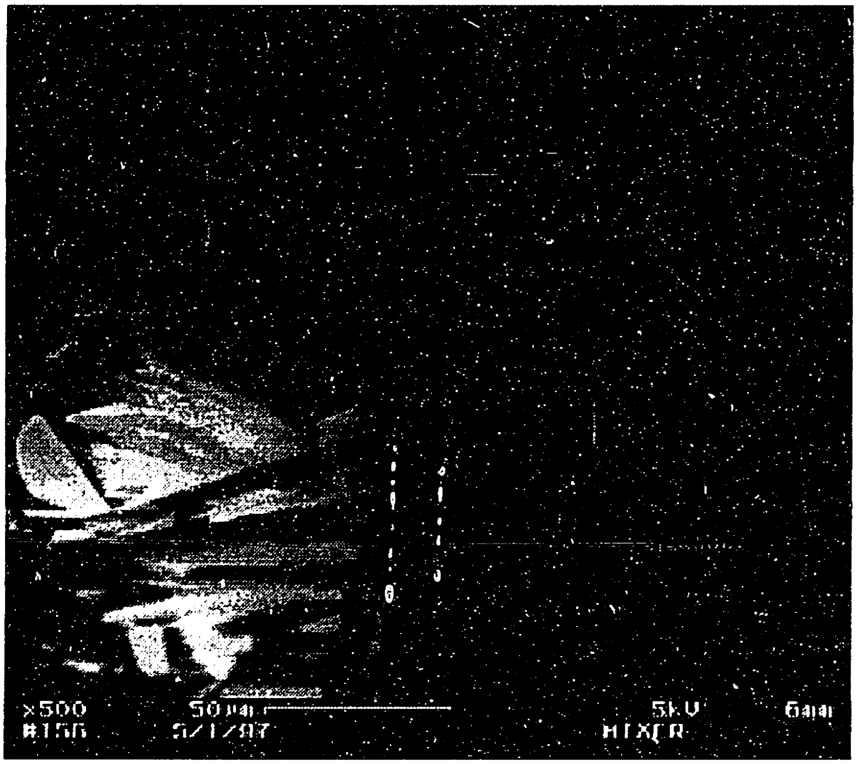

Figure 3-27: Closeup of cantilever-plate area

Chapter 4

Testing

This chapter details the testing of the microfabricated liquid mixer. Section 4.1 explains the various parts of the test setup. Section 4.2 explains the characterization of the testing apparatus. Section 4.3 details various experimental results obtained for the liquid mixer.

4.1 Test Setup

The test setup accomplishes four objectives. First, it connects the micro-world of the liquid mixer to the macro-world of standard test equipment. Second, it provides flow for the liquid mixer. Third, it measures relevant parameters such as flow rate and pressure. Lastly, the setup allows optical measurements to be made to characterize the liquid mixer.

4.1.1 Packaging

The package works in conjunction with the chip to provide flow in and out of the chip. A constraint is imposed in that there cannot be anything on top of the chip, as this would impair microscopy with short-working-distance objectives; the thickness of the glass wafer is already approximately 400 μm, and it would not be prudent to increase that distance. A two-tier approach is employed to solve the packaging problem, as shown in Figure 4-1. The dual-block system allows for a simply machined disposable unit and a complex permanent unit. The package is made of aluminum, because it is inexpensive and easy to work. The bottom block is the plumbing block. It has Tygon tubing epoxied to it to connect to the fluid system (detailed in the next section). The fluid goes in the side holes and makes a 90 degree turn to emerge on the top surface of the block. Side inlet holes are used because this allows the block to be mounted on a three-axis rotation stage, which is used to complement the x-y-z stage of a microscope, allowing the chip to be properly orthogonalized to the x-y-z stage. The plumbing block is connected with screws to a replaceable top attachment block. Three o-rings prevent leakage between the blocks. The chip itself is epoxied to the attachment block and three channels direct the liquid between the chip and the plumbing block.

The blocks are attached to the 3-axis rotation stage and it is attached to an inverted microscope stage (Figure 4-2). This allows for use of the inverted microscope (described more fully in section 4.1.4) with epi-illumination (illumination that is reflected off the substrate, as opposed to transmitted).

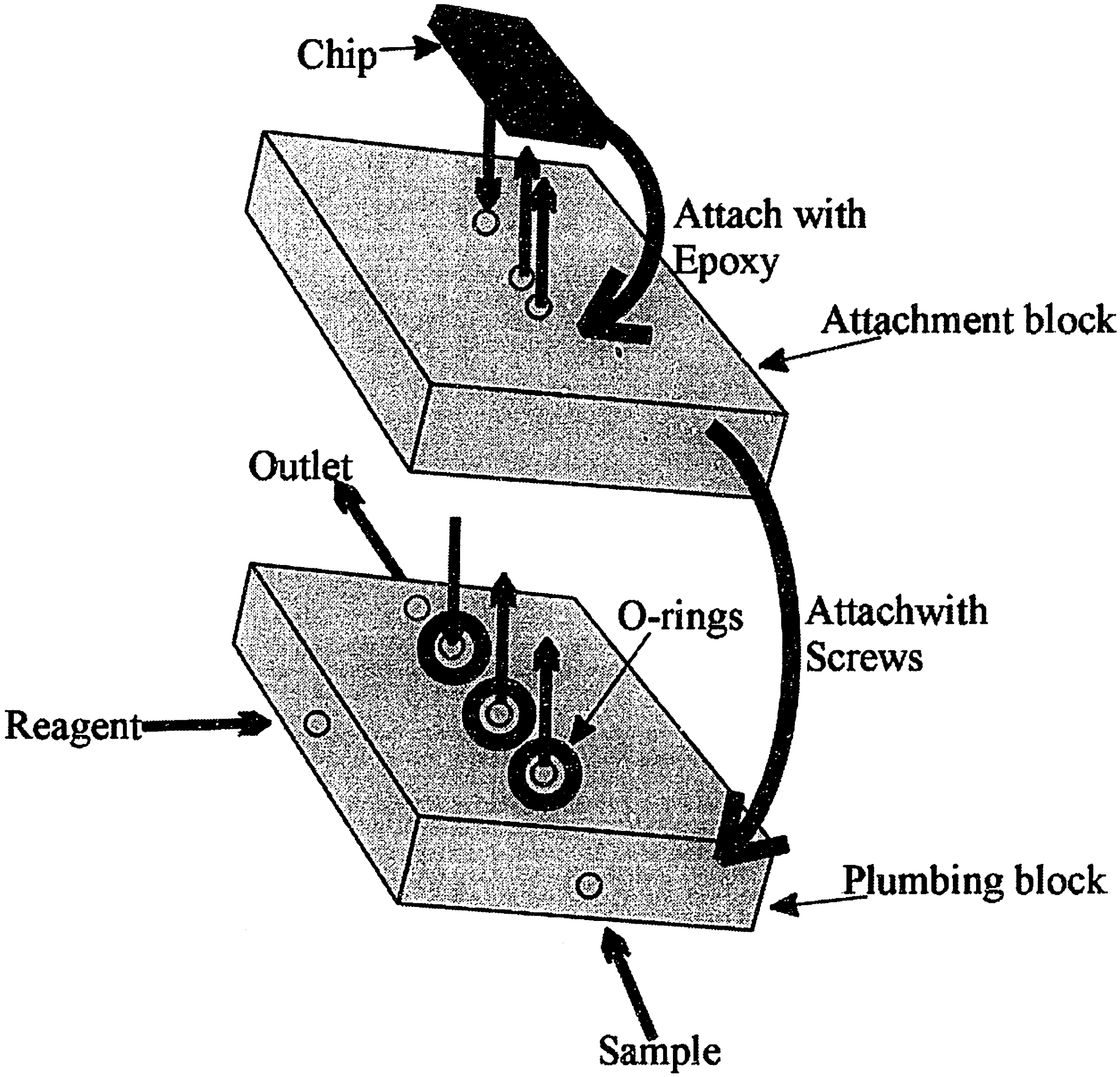

Figure 4-1: Liquid mixer package

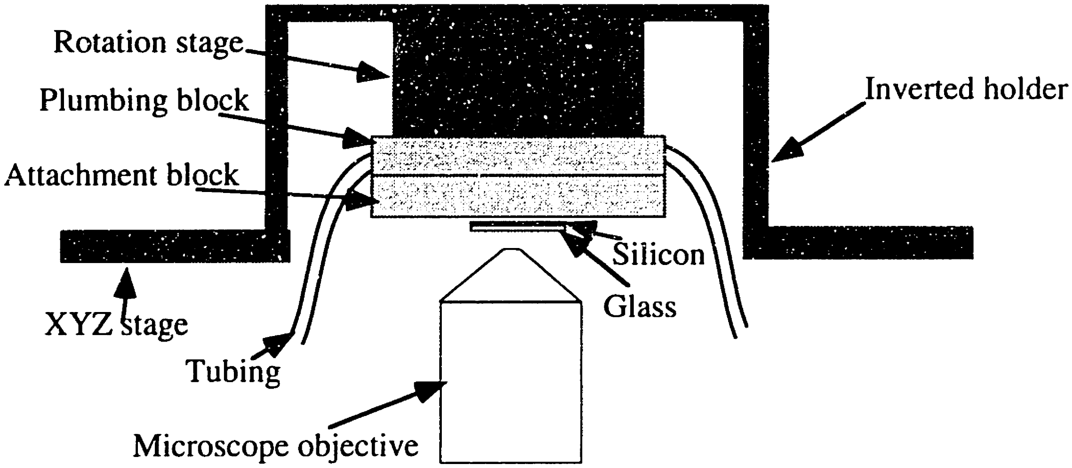

Figure 4-2: Packaging setup

4.1.2 Fluidic Setup

The fluidic setup provides flow for liquid mixer. As detailed in Figure 4-3, the setup consists of the several elements. Since the setup is mostly symmetrical, it is only necessary to detail one-half of the setup. The only point of non-symmetricality are the two syringe pumps, which are made by different manufacturers (Orion Research and KD Scientific). The Orion Research syringe pump is used to drive the sample flow, while the KD Scientific syringe pump is used to drive the reagent flow. The syringe pumps use an electrically-actuated drive screw to deliver a user-set flow rate, up to a given back pressure. They are akin to current sources in electrical engineering. It is important to note that the two syringe pumps differ remarkably in ability, as will be shown in Section 4.2. For most of the experiments, 1 mL glass Hamilton syringes were used in the syringe pumps, because of their high inner-diameter accuracy and precision. On occasion, Becton-Dickinson plastic syringes were used, and this will be noted in the text. The output of the syringe pumps are filtered with 0.45 μm disposable nylon syringe filters (Micron Separations, Inc.) and feed into a 3-way stopcock which allows pressure driven flow (detailed below). Following the stopcock, the flow goes through a T-connector which provides a pressure port for pressure measurement. The flow then goes into a 25s gauge needle (Hamilton) and into the Tygon tubing in the package (previous section). All the fluidic connections are made with luer lock connectors (except between the needle and the Tygon tubing, which are press-fitted together).

One important item concerns the pressure sensing with the pressure transducer in the T-adapter. Ideally, pressure taps for static pressure measurement should be negligible in area in order to not disturb the flow [79]. Since the pressure tap is quite large in this case, it could disturb the flow, causing vortices to be shed at the T-adapter and causing a flow-dependent pressure error. To ensure that this is not a problem, computational fluid dynamics (CFD) simulations were run. These are detailed in Appendix C, with the result being that the error due to the large opening is negligible for the flowrates of interest.

As it may be desirable to have pressure-driven flow, to allow purging, etc., a pressure subsystem is included in the fluidics. It consists of a helium tank which drives a pressure vessel. The pressure vessel output feeds into a 0.5 μm filter (Nupro) and connects through 1/8" tubing to the stopcock describe above.

After the liquid streams mix in the mixer, they are fed through Tygon tubing into a container in an electronic balance. The scale sends the weight via a parallel port to a Macintosh LCII.

4.1.3 Electrical Setup

The electronics in the experimental setup do all the transduction of the measurands. Three quantities are measured - reagent inlet pressure, sample inlet pressure, and total weight. The total weight is measured with the mass scale described in the previous section.

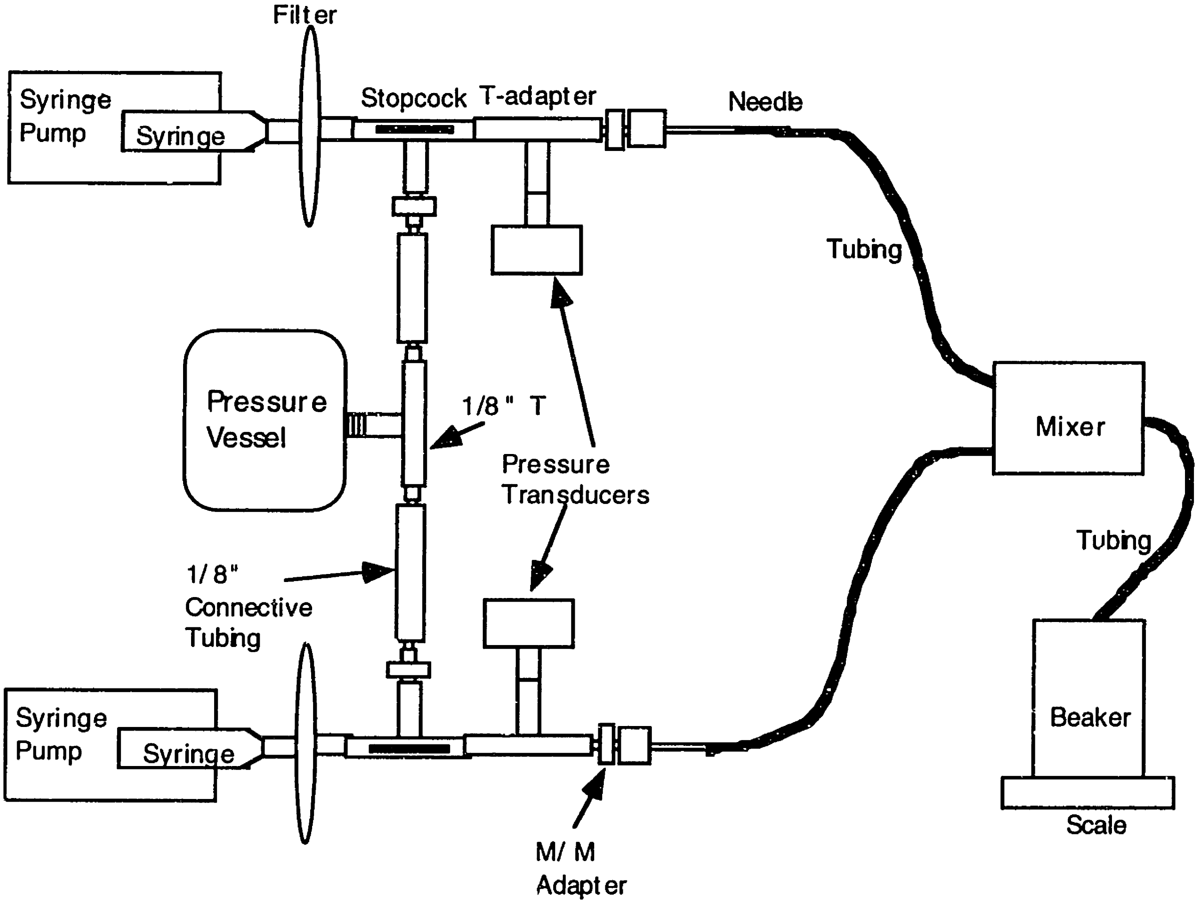

Figure 4-3: Fluidics setup

The pressures are measured via pressure transducers tee-d into the fluidics. The pressure transducers are silicon micromachined piezo-resistive pressure sensors (Microswitch). The pressure is transduced via a wheatstone bridge, as shown in Figure 4-4. The output of the pressure sensor is amplified and converted from differential to single-ended with an instrumentation amplifier (Analog Devices AD624). The output of the instrumentation amplifiers is low-pass filtered to reduce the noise bandwidth. The signal then goes into a data acquisition board (National Instruments Lab-NB) which buffers the signal and converts it into a 12-bit digital representation. The board is in the same Macintosh LCII that the electronic balance signal feeds into. The two pressures and weight (from the scale) are recorded with a LabView program (National Instruments). With this setup, the noise floor of the system is less than 1 bit of the A/D, which is 2.44 mV. This corresponds to a pressure change of 0.004 psi.

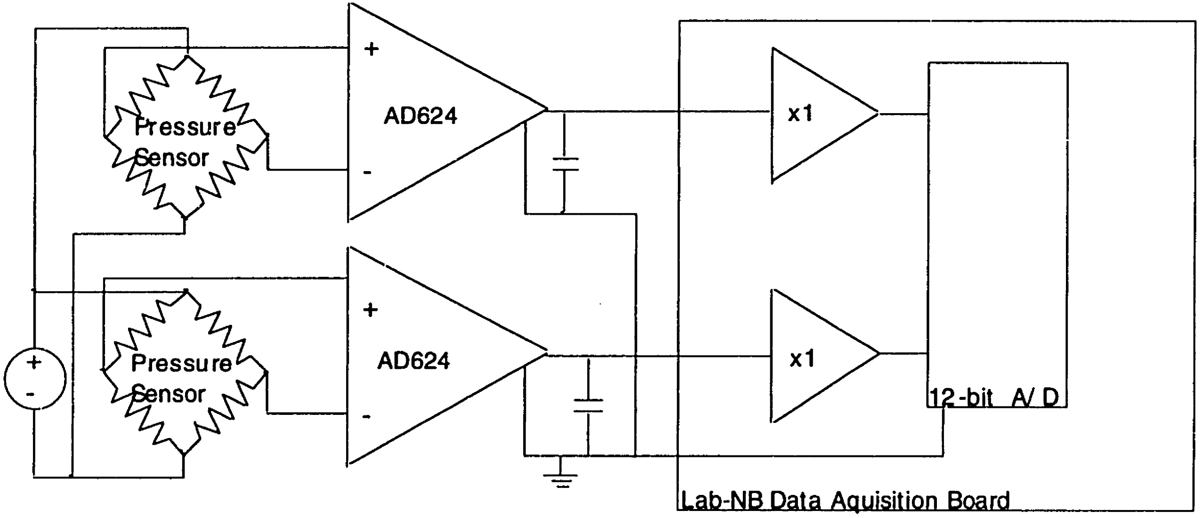

Figure 4-4: Electronics setup

The maximum bias errors quoted for the pressure sensors are given as

Error	Relative to full-scale output	Absolute error
Linearity	± 0.2 % F.S.O.	± 0.03 psi
Stability over one year	± 0.5 % F.S.O.	± 0.075 psi

The above table does not include offset errors because they subtract out of the relative measurements that are being made. While the experiments are not being carried out for a year, the temporal spectrum of the stability error is not known, and it is safer to assume the maximum error. Using the root-sum-square (RSS) method [80], this leads to a bias error of

$$\text{Total Error} = \sqrt{0.2^2 + 0.5^2}$$
$$= \pm 0.54\% \text{ F.S.O.}$$

This corresponds to ±0.08 psi, which is significantly larger than the resolution. The precision errors are quoted as typically ±0.2 % F.S.O. which accounts for repeatability and hysterysis. The precision errors for pressure transduction in this setup will be experimentally determined in section 4.2.

4.1.4 Optical Setup

The optical setup consists of a microscope, assorted optics, and optical-image capture hardware (Figure 4-5). The microscope is a Nikon Diaphot 300 equipped with for fluorescence imaging. The mercury arc light goes through the excitation wavelength filter to select the 488 nm line. The light then excites the fluorophore in the liquid mixer and the emission wavelength is selected out by the emission filter. The light feeds into a silicon intensified target (SIT) camera (Hamamatsu C2400) which feeds the signal through signal conditioning circuitry and into a Macintosh Quadra which captures the images.

4.1.5 Reagents

The fluorophore used in these experiments is fluorescein sodium salt, or uranine [81,82,83]. It is a water-soluble form of fluorescein with a molecular weight of 376.28 g/mol. It has a maximum absorption at approximately 490 nm and an fluorescence emission maximum at approximately 520 nm, depending on the solvent. It is used at 10 μM concentrations at a pH of 10, unless otherwise noted.

All acids used in the experiments are made by mixing 1 M HCl with deionized and filtered water until the correct pH is obtained. All bases are made similarly, except that 1 M NaOH is used.

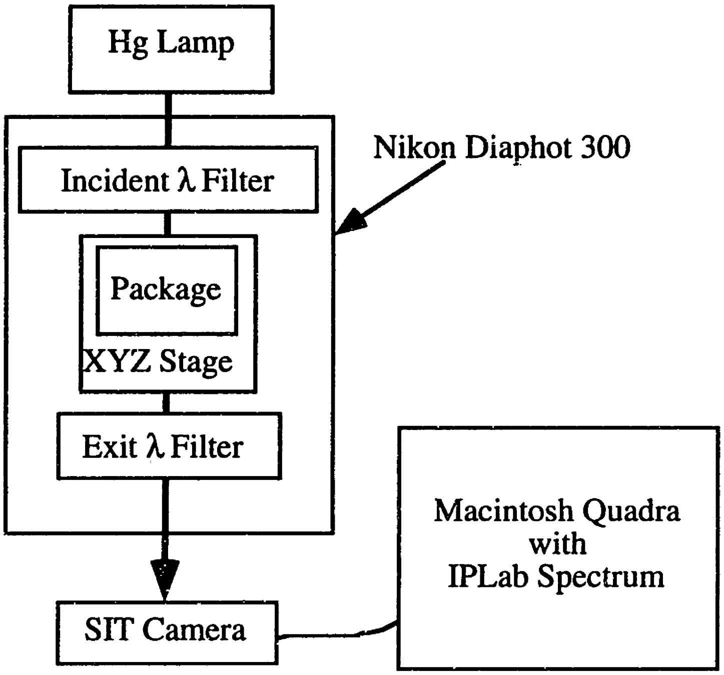

Figure 4-5: Optical setup

4.2 Apparatus Characterization

With the apparatus set up, it is necessary to characterize the system so that the various errors can be determined and to ensure that it is stable and reliable. A calculation of the nominal flow resistances in the fluid path is shown in Figure 4-6. The resistances in the chart and all the flow resistances detailed in this chapter are defined as the ratio of the pressure to the flow rate

$$R = \frac{\Delta P}{Q} \qquad (4.\ 1)$$

Since the pressure is given in psi and the flow rate in µl/min, the unit of resistance is defined as

$$1\,\Omega = 1\ \frac{\text{psi}}{\text{ul/min}} \qquad (4.\ 2)$$

Figure 4-6 shows that besides the liquid mixer, the needle and the tubing have a non-negligible flow resistance. The figure does not include the flow resistance of the cantilever plate because it is nonlinear and flow-rate dependent. In order to characterize the liquid mixer test setup, it is necessary to determine these resistances.

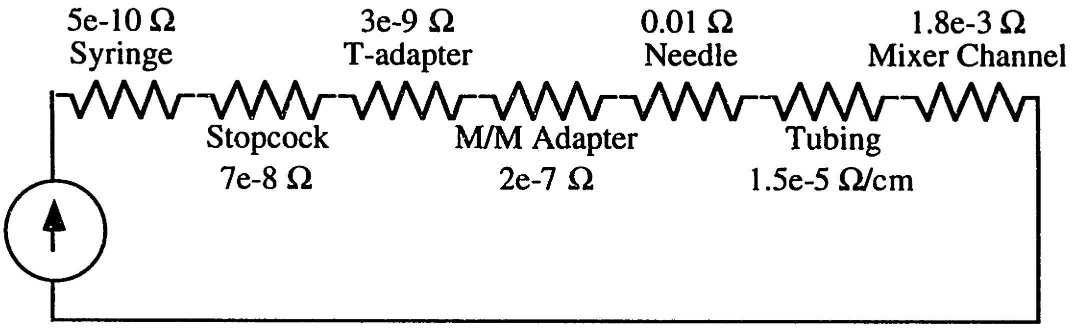

Figure 4-6: Flow resistances in fluid circuit

4.2.1 Protocols

All the experiments in this section use DI water at room temperature (T = 25-26 °C). For the experiments in this section, syringe filters were not used, since they are not important for the measurements.

The first step is to purge the system using the pressure vessel. Water is flown through the system at high pressure (~10-15 psi) for 30 minutes. This dislodges all bubbles in the tubing and fluidic setup. A visual inspection is also performed to ensure that no bubbles are present in the setup. While the system is being purged of bubbles, the electronics (power supplies, sensors, computers, scale) are turned on and left to warm up for 30 minutes. After 30 minutes, the pressure vessel is turned off and syringe flow is initiated for the remainder of the experimental period.

4.2.2 Reagent Syringe Pump and Needle Calibration

The main purpose of these measurements is to determine the reagent syringe pump (KD Scientific) experimental errors and to calibrate the syringe needle. Since the reagent syringe pump is more accurate and repeatable than the sample syringe pump, these measurements will also calibrate the tubing flow resistances.

The flow rates used in these experiments are the stated flow rates given by the reagent pump itself, without any closed-loop monitoring. This is because the stated flow rate is more accurate than the measurable flow rate. The reagent pump is a stepper-controlled syringe pump with a rated accuracy and precision of ±0.2 % . The other errors in the volume flow rate are due to syringe variations. The manufacturer (Hamilton) does not disclose such specifications for its syringes, but the bias error on the syringe cross-sectional area can be estimated from product literature as ±1.0 %. This gives a total bias error for the flowrate of ±1.0%. As will be discussed shortly, this is much better than using the electronic balance to determine volume flow.

Figure 4-7 shows typical raw data from a run with the reagent syringe pump. As can be seen, the output is very uniform and constant. The noise in the figure is due to pressure fluctuations in the pump.

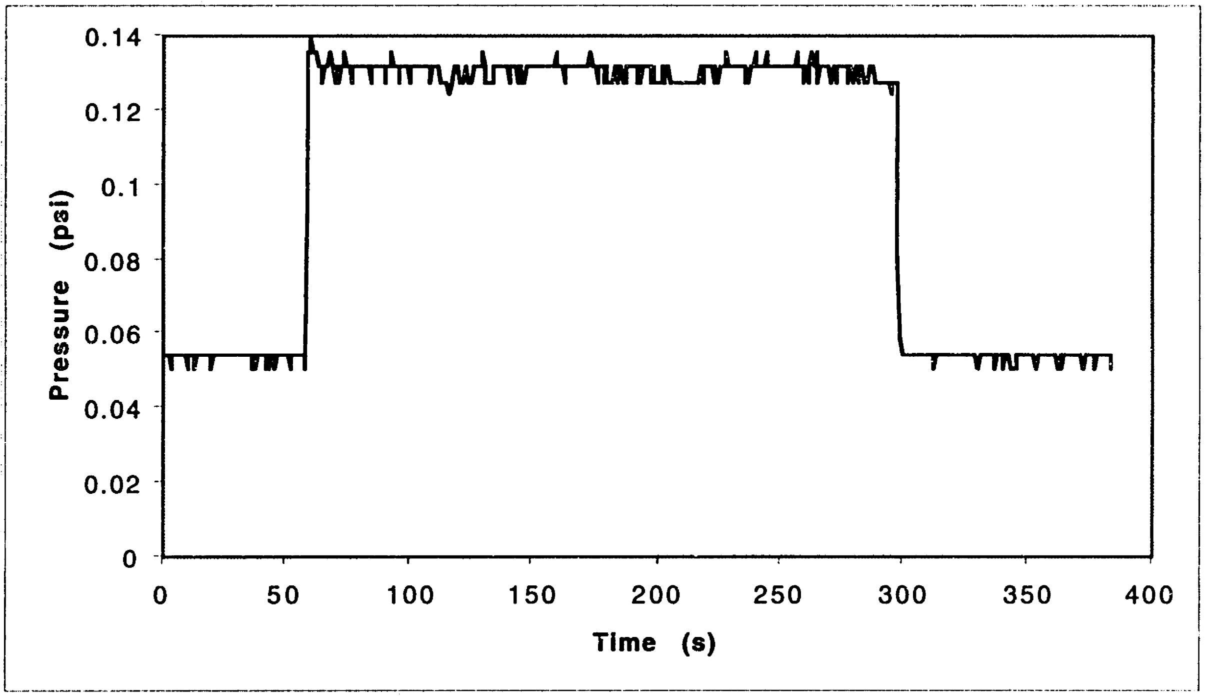

Figure 4-7: Reagent syringe-needle calibration (raw data)

To determine the flow resistances of the tubing and reagent needle, the pump is run at different flow rates with two different tubing lengths. The situation is then as depicted in Figure 4-8.

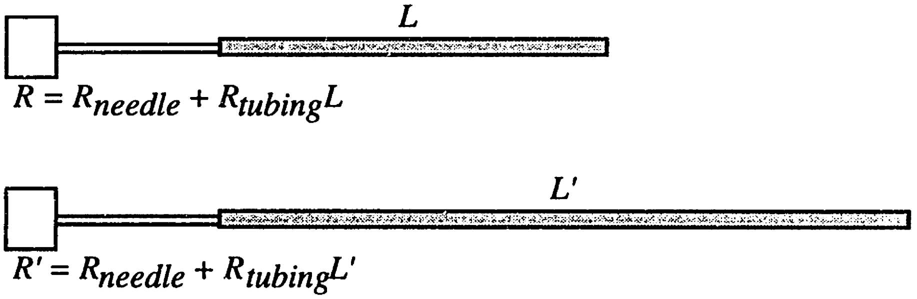

Figure 4-8: Relation between measured and fundamental resistances

Since *R* and *R'* are measured and the lengths of tubing are known, the tubing resistance (per cm) can be determined as

$$R_{tubing} = \frac{R' - R}{L' - L} \tag{4. 3}$$

From this, the needle resistance can be determined accordingly.

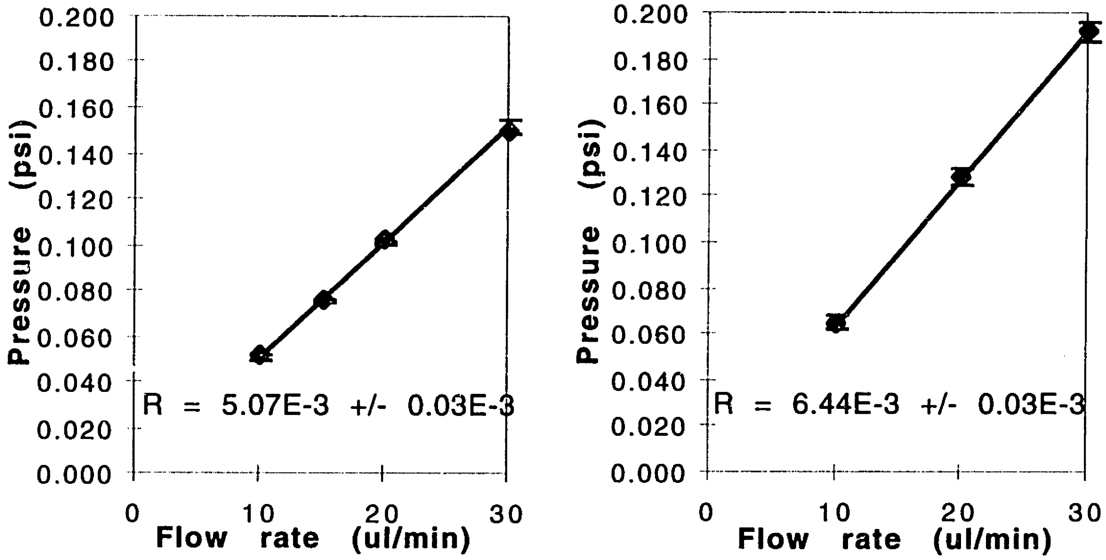

Figure 4-9: Reagent-needle pressure-flow relationship with two different tubing lengths

The distilled experimental data is shown in Figure 4-9 for two different tubing lengths. The pressure sensor bias errors of ±0.08 psi are not shown in the plots. From this, the fluid resistance of the needle is determined to be 4.74e-3 psi/(µl/min) with a total error of ±0.03e-3 psi/(µl/min). The tubing resistance (per cm) is determined to be 1.8e-5 psi/(µl/min) with an error of ±0.06e-5 psi/(µl/min).

4.2.3 Sample Syringe Pump and Needle Calibration

To calibrate the sample-inlet needle the flow rate must be determined from the mass balance. The electronic balance must be used because the reading from the sample syringe pump (Orion Research) has a rated accuracy of ±10% and a rated precision of ±15%, in contrast with the reagent syringe pump. To reduce these errors, the flow rate is computed by taking the mass flow per unit time and converting it to a volume flow rate corrected for the ambient temperature of the room.

Typical raw data for these experiments is shown in Figure 4-10. In comparison to the reagent syringe pump (KD Scientific), it is evident that the sample syringe pump (Orion Research) is much noisier. In addition, there is a pressure pulse when it is turned on and off.

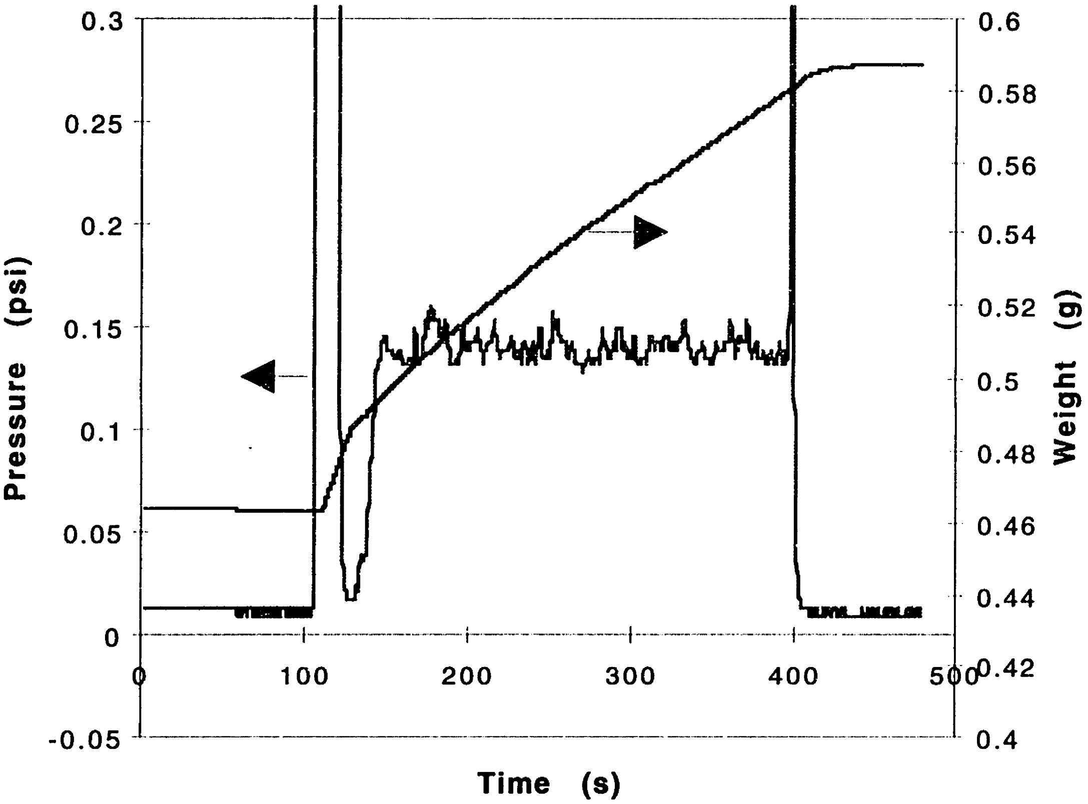

Figure 4-10: Sample needle calibration (raw data)

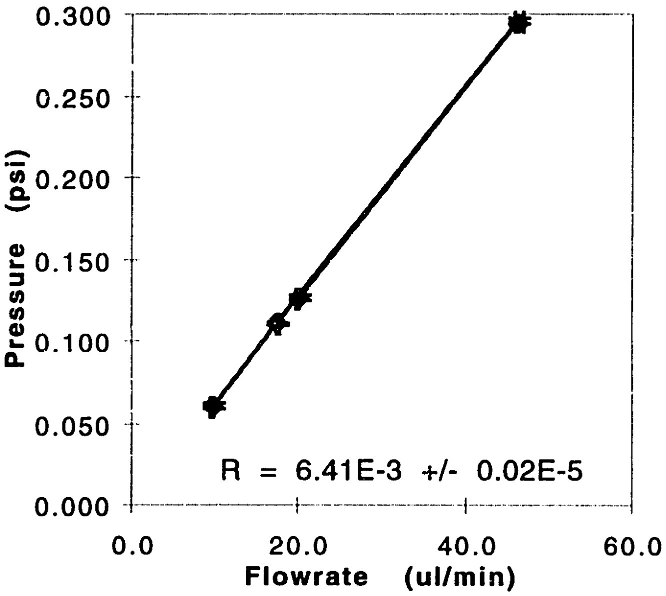

Figure 4-11: Sample needle pressure-flow relationship

Using this setup, flow rate and pressure are measured at 4 different flow rates 4 time each, with at least 200 points for each measurement. From the raw data the needle characterization data can be distilled into Figure 4-11, which has not been corrected for tubing resistance. Again, the bias errors in the pressure transducers are not shown. Using the distilled data and accounting for the tubing resistance, the sample needle resistance is determined to be 4.73e-3 psi/(μl/min) with an error of ±0.05e-5 psi/(μl/min).

4.3 Liquid Mixer Results

Once the test setup has been characterized and verified, it is possible to test the liquid mixer. Three sets of experiments are undertaken to verify its performance. The first is an optical study showing that the mixer is operating and mixes. The second set of experiments determine the pressure-flow relationships for the liquid mixer. Finally, the last set of experiments involve fluorescence studies to determine mixing lengths for the liquid mixer.

All the pictures in this section are fluorescent images depicting the area surrounding the cantilever-plate. To be able to better understand them, Figure 4-12 shows a representative picture with a line drawing beside it explaining what the picture shows.

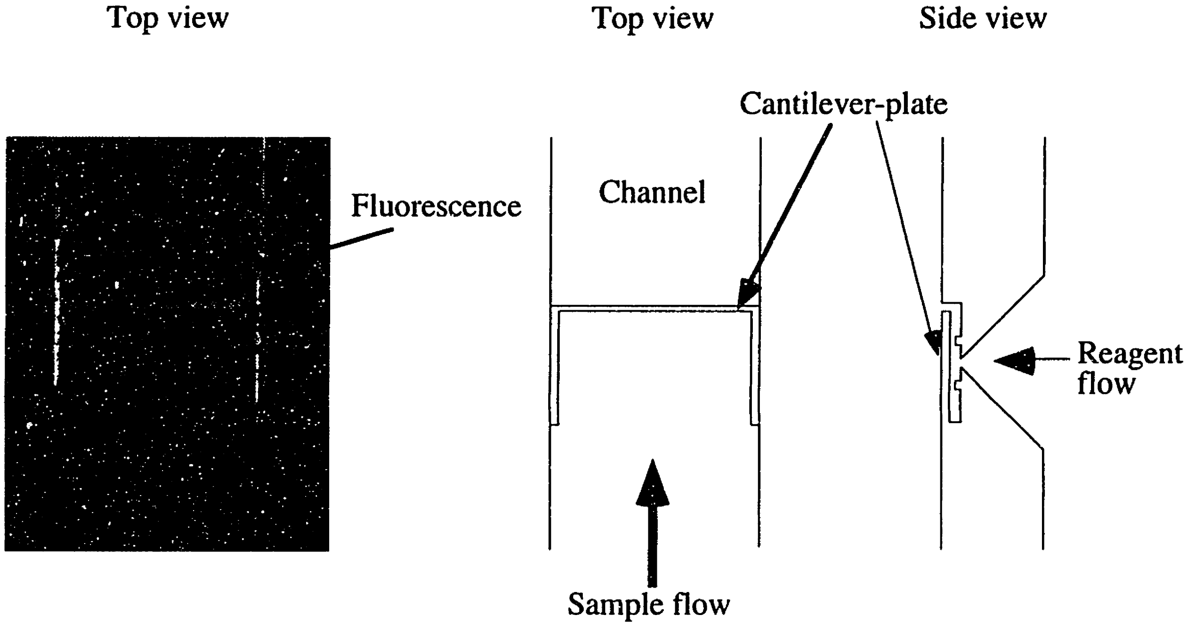

Figure 4-12: Explanation of pictures

4.3.1 Mixer Operation

These first experiments verify that the cantilever-plate flapper valve allows reagent to merge with the sample stream. The is accomplished by mixing water (sample) with fluorescein (reagent). The pictures are shown in Figure 4-13. As can be seen, the mixer works. The striations in the fluorescent flow are due to particles on the edge of the plate which disturb the flow. These particles are thought to be due to the epoxy used in attaching the liquid mixer chip to the attachment block. The epoxy is somehow entering into solution with the water and coming out of solution preferentially around the edge of the cantilever plate, attaching itself to the plate.

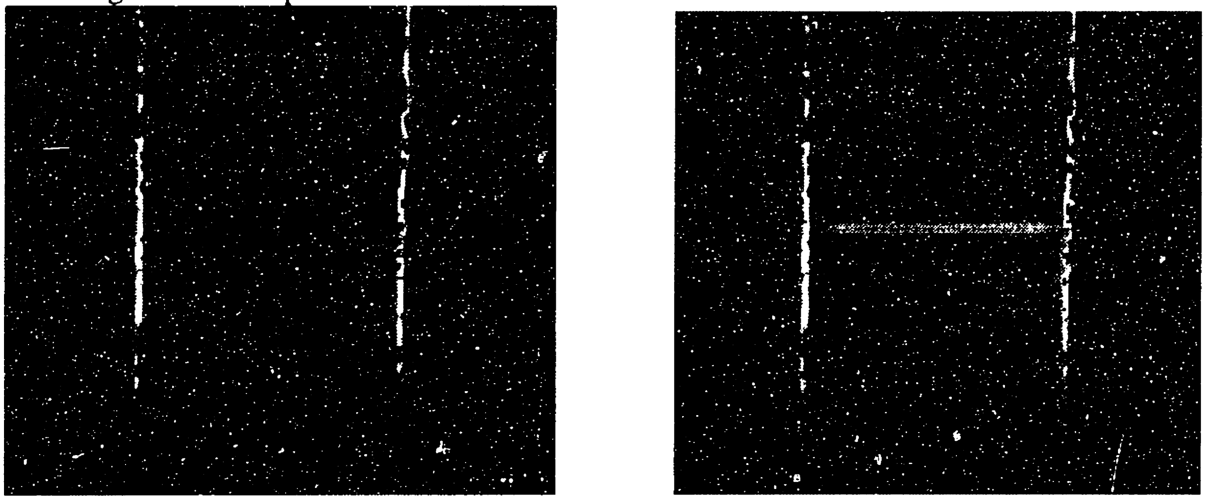

a) No flow

b) Flow initiated

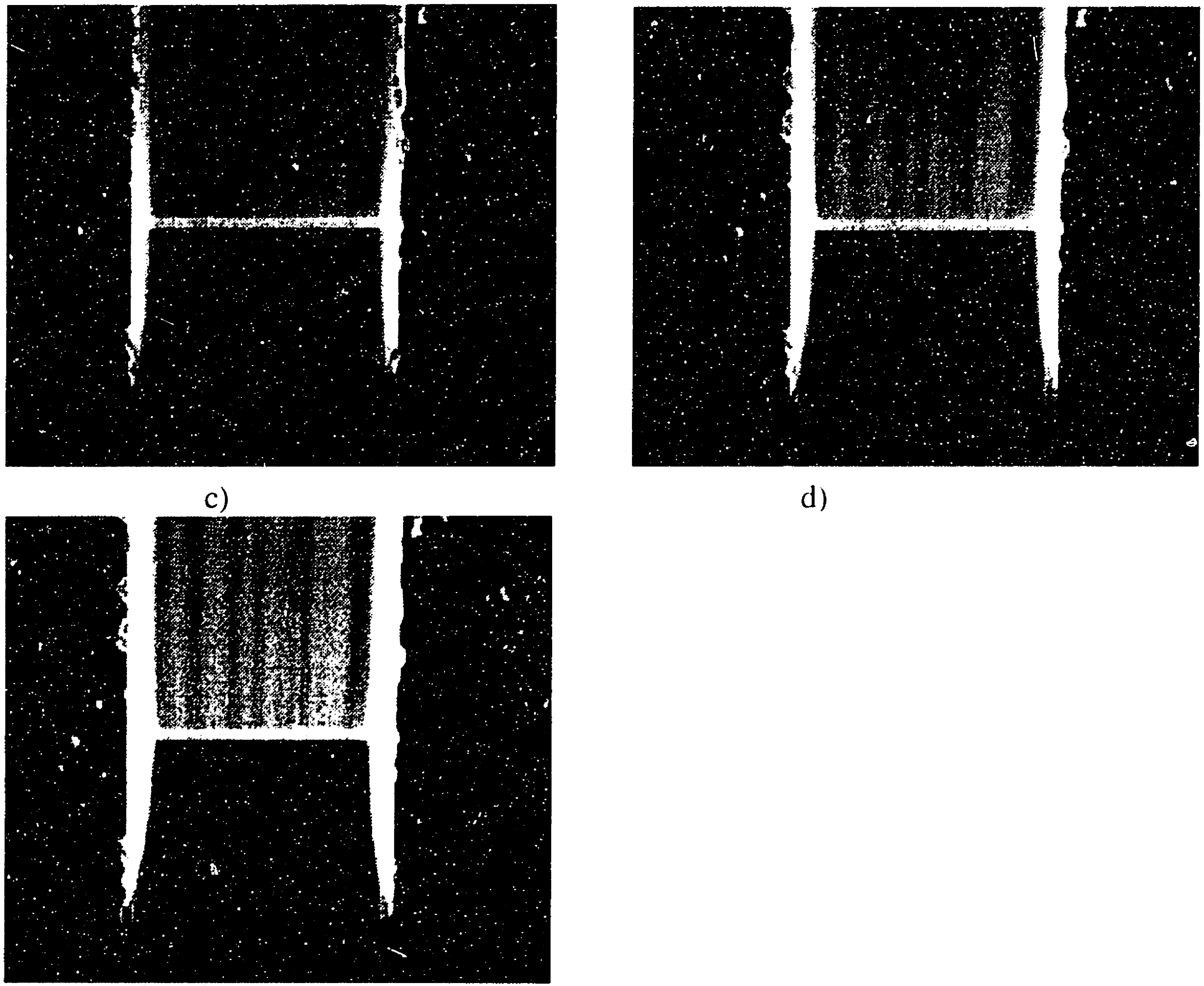

c)

d)

e) Steady-state

Figure 4-13: Mixer operation

As is evident from Figure 4-13, a significant fraction of the reagent stream (fluorescent dye) enters the sample stream from the sides of the cantilever-plate. This effect is unwanted, and results in a poorly mixed cylinder of fluid on the sides of the channel down its full length. This should be remedied in future designs by directing more of the flow out of the end of the cantilever-plate.

4.3.2 Pressure-Flow Relationship

Even though the liquid mixer is being flow-actuated in these experiments, it might be advantageous to pressure-actuate it in some circumstances. In addition, the pressure-flow relationships give important insight into the operation of the liquid mixer. This gives an impetus for measuring the pressure-flow relationship of the liquid mixer.

There are four variables in the pressure-flow relationships - the sample pressure, sample flowrate, reagent pressure, and reagent flowrate. To understand the interrelationships among the variables, the following measurement scheme is adopted. The sample flowrate is set, and the reagent flowrate varied. This is repeated for four different sample flowrates. Within these four sample flowrates, the reagent flowrate is varied between no reagent flow and a mixing ratio (sample:reagent) of one. The pressures and flow rates are measured for both sample and reagent at each point. From this data, the needle and tubing resistances are removed. Thus, the pressures described in this section are the pressures at the input of the ports with respect to the output of the outlet port.

Before viewing the results, it is useful to discuss what is expected. For zero reagent flowrate, the sample pressure should increase linearly with the sample flowrate, since all the fluid resistances in that path are linear. As the reagent flow is increased, though, the cantilever plate should open up, and for given sample and reagent flowrates, the pressures should reflect the hydromechanical equilibrium set up between the two flows and the cantilever plate. Since the measured pressures reflect this coupled hydromechanical system, and since the coupling between the two systems will most likely be nonlinear, the pressure-flow relationships themselves should be nonlinear.

Figure 4-14 shows the distilled data for one of the four sample flow rates. As can be seen, the reagent and sample pressures rise with reagent flow rate for a given sample flow rate.

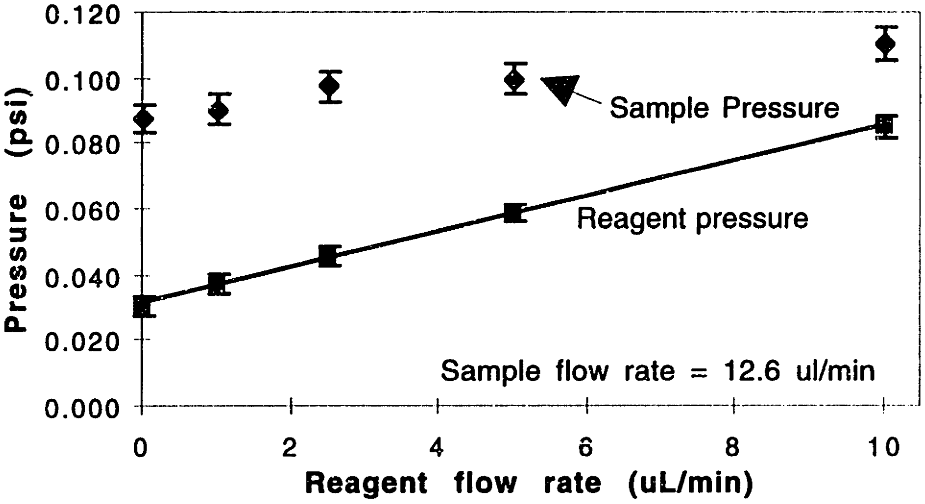

Figure 4-14: Pressure-flow relationship at one sample flowrate

Another way to view the data is to plot the sample pressure and reagent pressure versus mixing ratio (sample:reagent) for different reagent flow rates. Since the mixing ratio includes a point at infinity (zero reagent flowrate), the inverse of the mixing ratio is plotted. Plots of this are given in Figure 4-15 and Figure 4-16.

The sample pressures show little variation with reagent flow rate, although a small increasing trend is observed. This initially seems odd, since at a mixing ratio of one the sample pressure would be expected to be twice what it is at a mixing ratio of zero because the total flow rate is twice as high. This discrepancy can be related to the previously mentioned one, and it too will be explained below.

The reagent pressures increase linearly with the inverse of the mixing ratio, with different slopes depending on the sample flow rate. The fact that the relationship is linear is unexpected, since the plate mechanics and fluid mechanics are nonlinear. It indicates that one of two things are happening. First, the coupling between the two domains could be such that a linear relationship develops, possibly because both domains are in their linear regimes. A second possibility is that the cantilever-plate is not moving at all, but that it is acting like a fluid resistor. The first possibility can only be determined by modeling the coupled system. The second possibility will be discussed below.

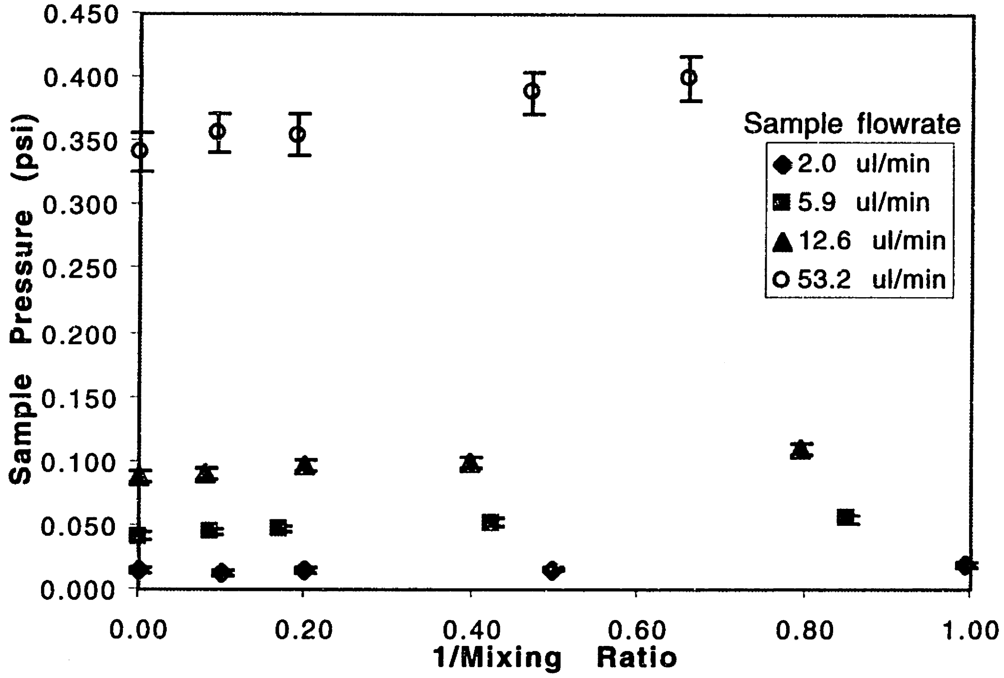

Figure 4-15: Sample pressure for different mixing ratios and sample flowrates

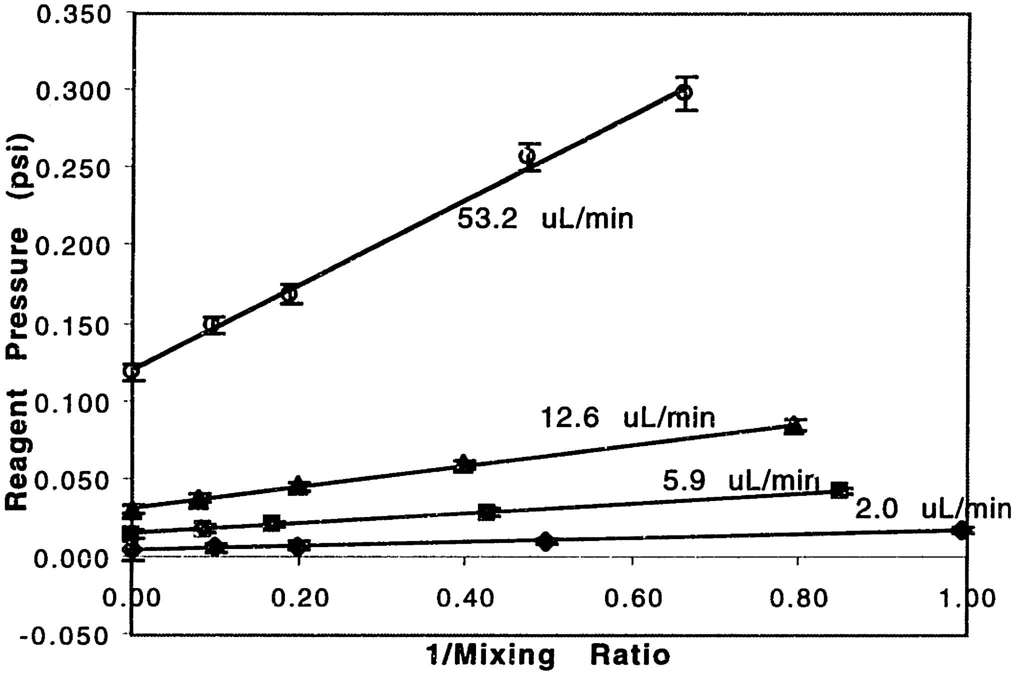

Figure 4-16: Reagent pressure for different mixing ratios and sample flowrates

A final observation with the pressure-flow relationships concerns the region where the inverse of the mixing ratio is zero (the mixing ratio is infinity). This is the y-intercept of the plots in Figure 4-15 and Figure 4-16. Since the mixing ratio is defined as the ratio of sample to reagent, this is the situation where the reagent flow is zero and the sample flow is varied. As the cantilever plate does not provide a perfect seal between the reagent inlet port and the channel, the pressure sensed by the reagent pressure transducer will be related to the pressure in the channel at the cantilever plate via some fluid resistance. And since there is no reagent flow between the reagent pressure sensor and the cantilever plate, there will be no pressure drop between the reagent pressure sensor and the cantilever plate, and the reagent pressure sensor will sense the pressure in the channel at the cantilever plate due to the sample flow. Thus, a plot of the pressures when there is no reagent flowing would give the pressure at the beginning of the channel (sample pressure) and part-way down the channel (reagent pressure), lending insight into the fluid resistances of the liquid mixer. This plot is shown in Figure 4-17. As can be seen, the sample inlet has a higher resistance than the reagent inlet. This is to be expected, since the reagent pressure is sensed downstream of the sample pressure. The sample pressure-flow relationship has a slope (resistance) of 6.5e-3 ±0.08e-3 psi/(µl/min). This is compared to a calculated resistance for the channel and two ports (sample inlet and mixed outlet) of 1.9e-3 psi/(µl/min). The discrepancy between these two values will be explained below.

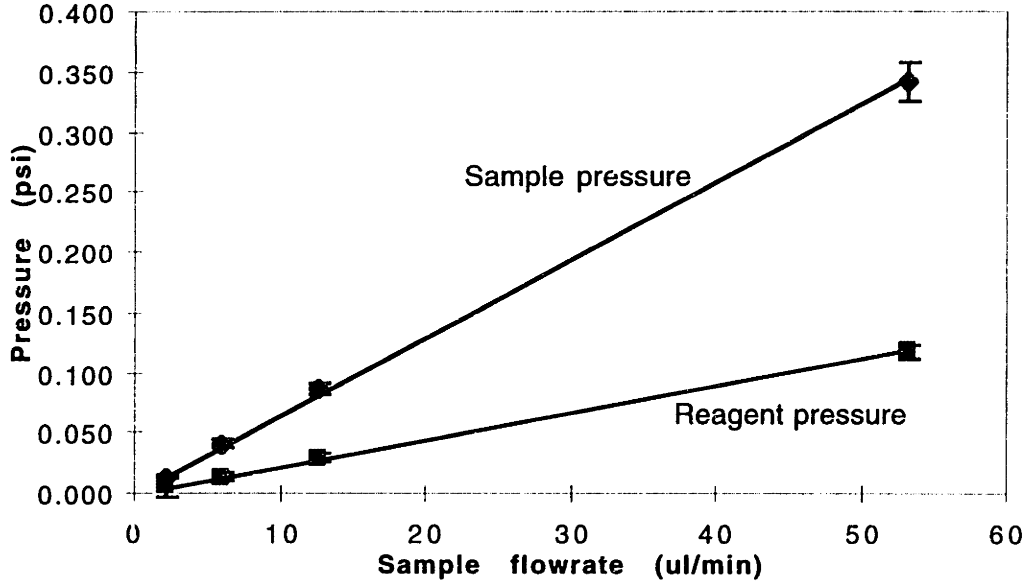

Figure 4-17: Pressure-flow relationship when no reagent is flowing

In order to explain the small sample pressure change for different mixing ratios, the discrepancy between the observed and calculated channel resistance, and to determine if the cantilever plate is indeed acting as a resistor (without moving), the following model is used. As Figure 4-18 explains, the liquid mixer can be thought of in terms of an equivalent circuit. The values for R_1 and R_2 can be determined from Figure 4-17 by noting that when the reagent flow is zero, the sample pressure is proportional to R_1+R_2, and the reagent pressure is proportional to R_2. When the reagent flow is turned on, the reagent pressure is proportional to R_2+R_3, allowing a determination of R_3. The calculated values for the resistances are given in the figure. The data in Figure 4-15 and Figure 4-16 can be fitted to this model, with the results shown in Figure 4-19 and Figure 4-20. As the figures show, the model fits well. This means that the cantilever-plate is acting as a fluid resistor. Also, as the equivalent circuit shows, the channel resistance is only a fraction of R_1 and R_2 and so is less than the 0.0065 Ω quoted above. In addition, since the reagent port resistance is 0.0032 Ω, and since the sample port resistance should be similar to that, the channel resistance could be much closer to the predicted value (0.0019 Ω). Thus, the model explains all the discrepancies listed above and shows that the cantilever plate is not moving as expected.

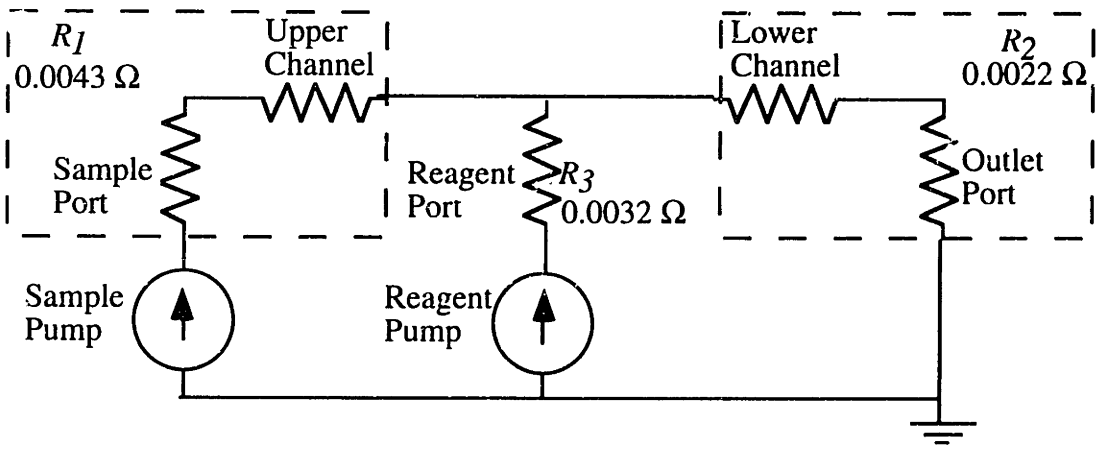

Figure 4-18: Liquid mixer equivalent circuit

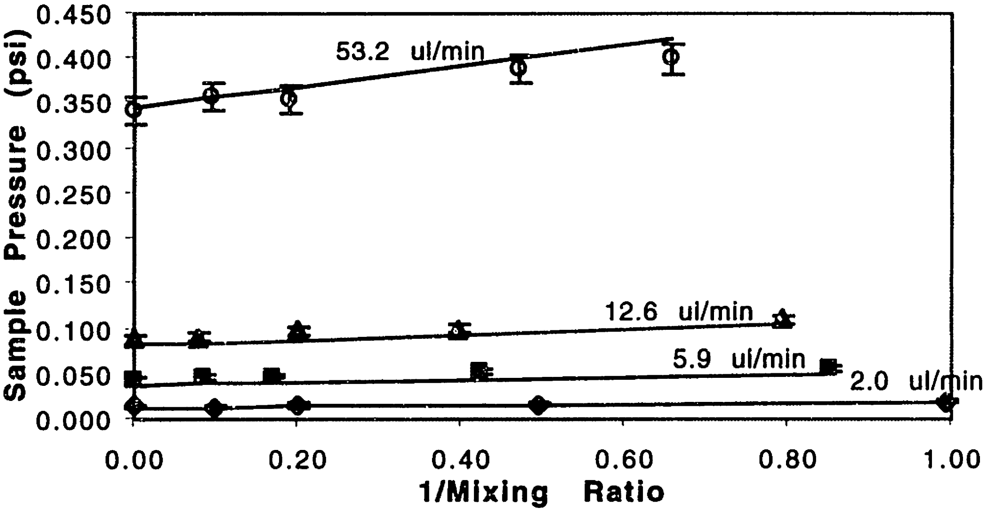

Figure 4-19: Sample pressure for different mixing ratios fitted to resistor model

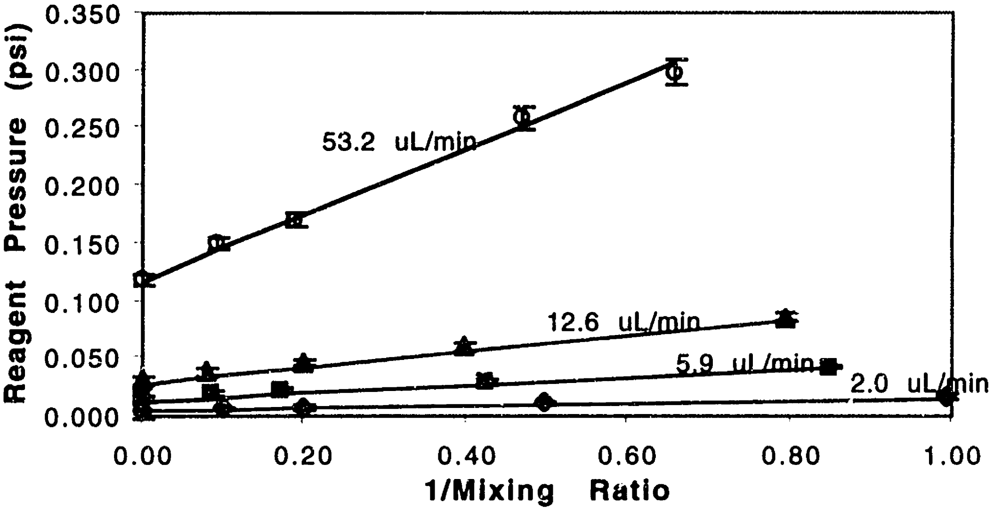

Figure 4-20: Reagent pressure for different mixing ratios fitted to resistor model

In order to determine if the pressure-flowrate relationships are linear even at high flowrate, an experiment was undertaken with a sample flowrate of 218 µl/min, using plastic syringes to be able to achieve the high flowrates. The results are shown in Figure 4-21. As can be seen, the relationship is linear with a slight nonlinearity entering at high flowrates. This means that the cantilever-plate is not moving much during operation, but instead acts like a resistor. This can be corrected in future implementations by making the cantilever plate less rigid.

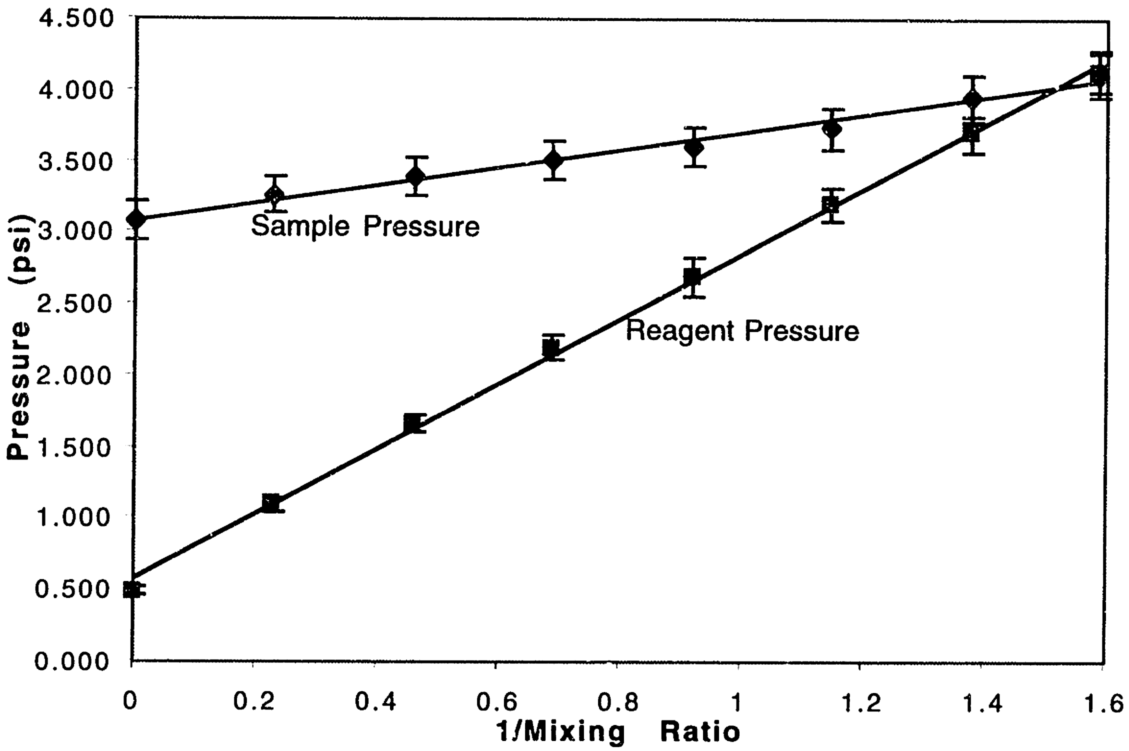

Figure 4-21: Pressure versus mixing ratio at high sample flowrates

4.3.3 Mixing Length Measurements

There are several ways to measure the mixing length of the reagent in the sample. All of the methods considered here utilize a fluorescent marker in the reagent stream and no marker in the sample stream. The first way is to use a confocal microscope to image z-slices of the channel and recreate the 3-dimensional flow profile. With the proper calibrations, quantitative data about the fluorophore concentration (and hence the degree of mixing) at every point could be determined. This method was not adopted here for lack of a confocal microscope, and because such a procedure would give much more data than needed.

A second method would use a wide-field microscope but would use high N.A. objectives with image threshholding to remove out-of-plane fluorescence and capture z-slices. This is the method used by Sobek [12] in his flow characterization studies. This method could not be used here because: 1) the fluorescence intensity is not constant in the sample (due to mixing), and 2) the very-high N.A. objectives needed could not be used due to large working distances needed.

A third method, and the one used, takes advantage of the pH dependence of fluorescein's fluorescence quantum yield [84,85,86]. The fluorescence quantum yield of fluorescein varies from 0.93 at a pH of ~7.4 to 0.37 at a pH of ~3.3. Thus, all things being equal, the fluorescence intensity of the reagent stream will vary from bright at high pH to dim at low pH. This means that by mixing a basic solution of fluorescein with an acidic solution, information can be learned about the mixing length. This has been used before to study the turbulent mixing of fluids[87,88,89].

It is important to note that a method such as this will not measure the mixing length directly. The pH of a solution is equal to the negative logarithm of the hydrogen-ion concentration, not equal to the concentration itself. This means that mixing a basic mixture of fluorescein with an acid and measuring the fluorescence intensity "shut-off" length (where the intensity goes from bright to dim) will give the length needed to reach a pH of approximately 3.3. This may or may not be the length where the fluorescein is mixed, depending on the mixing ratios and acid and base concentrations.

In order to try to correlate the fluorescence "shut-off" length with the mixing length, diffusion simulations were undertaken. The domain is the same as in the simulations for Chapter 2, but now a 3-component diffusion (acid, base, fluorescein) with a reaction (acid+base) needs to be simulated. Because of the neutralization reaction, the concentrations of the acid and base diminish in time, and an analytical solution to the problem is not readily apparent. In order to simulate the problem, an implicit finite-difference scheme is adopted to simulate the time-dependent diffusion of the hydrogen ions (acid) and hydroxyl ions (base). The diffusion coefficient for H^+ is taken as 9.3e3 $\mu m^2/s$ and OH^- as 5.3e3 $\mu m^2/s$ [90]. The simulation solves the problem by calculating the concentration profiles for a time-step, reacting the acid and base, and using the new concentration profiles for the next time-step. When the concentration profiles of the acid and base have been determined for all time, the program finds the pH of the solution for all x and t. It then uses the pH to determine the fluorescence quantum yield of the solution, using a linear approximation to the quantum yield relationship for fluorescein. With the fluorescence quantum yield and the analytical solution to the fluorescein diffusion relationship, the fluorescence intensity of the solution is determined by integrating the concentration and the fluorescence quantum yield through the depth of the solution. The absorbance of the solution is neglected since the absorption coefficient is estimated to be much less than 10%. The results show that the fluorescence intensity of the solution "shuts off" before the solution is mixed. In addition, the "shut-off" length increases with decreasing mixing ratio until the mixing ratio reaches approximately 0.1, which is different from the mixing length characteristic (Figure 2-10) which peaks at a mixing ratio of one.

In order to test the simulation, experiments were carried out with fluorescein in 0.1 mM base and a 1 mM acid. Pictorial results at different mixing ratios are given in Figure 4-

22 and Figure 4-23. The total flowrate for these experiments was 100 μl/min, which allowed for a reasonable distance between the plate and fluorescence turn-off. In order to extract quantitative data from the pictorial results, the pictures were first corrected for spatial illumination variations, and then the pixel values (corresponding to the fluorescence intensity) in a region approximately 200 μm wide directly left of the center of the cantilever plate were averaged across the channel. This one-dimensional data was then scaled to fit a span of one (arbitrary) intensity unit. The final results are plotted in Figure 4-24 against the simulated intensities (scaled to a span of one intensity unit) to allow for comparison. The results agree with the simulation in that the "shut-off" length increases with decreasing mixing ratio past a mixing ratio of one. This indicates that the simulation is fundamentally correct. The shapes of the measured intensity curves differ from the simulation results and the "shut-off" lengths for the simulation are shorter than experimentally derived, partially due to the spatial averaging used in the experimental results and partially due to three simplifications made in the simulation.

The three major simplifications used in the simulation are: one, the simulation assumes that all the reagent flow exits from the end of the cantilever plate. In actuality, a non-negligible portion exits from the sides of the cantilever plate. This causes the mixing ratio in the center of the channel to be higher than at the edges, since less reagent than intended is in middle of the channel. This thus changes the mixing length significantly. Two, only a one-dimensional problem is considered, so that the flow rate of the reagent is constant across of the width of the channel. This is not true, since the reagent port hole underneath the cantilever plate does not span the full width of the channel and edge effects introduce a two-dimensional flow profile. Three, the simulations (and also Chapter 2) neglect convection. Convection will change the kinetics of the mixing because the convection of the fluorophore (and H^+ and OH^- ions) will change the concentration profile, thus changing the diffusion characteristics; the coupled convection-diffusion problem must be solved to better understand the system. These assumptions could be modeled in future simulations.

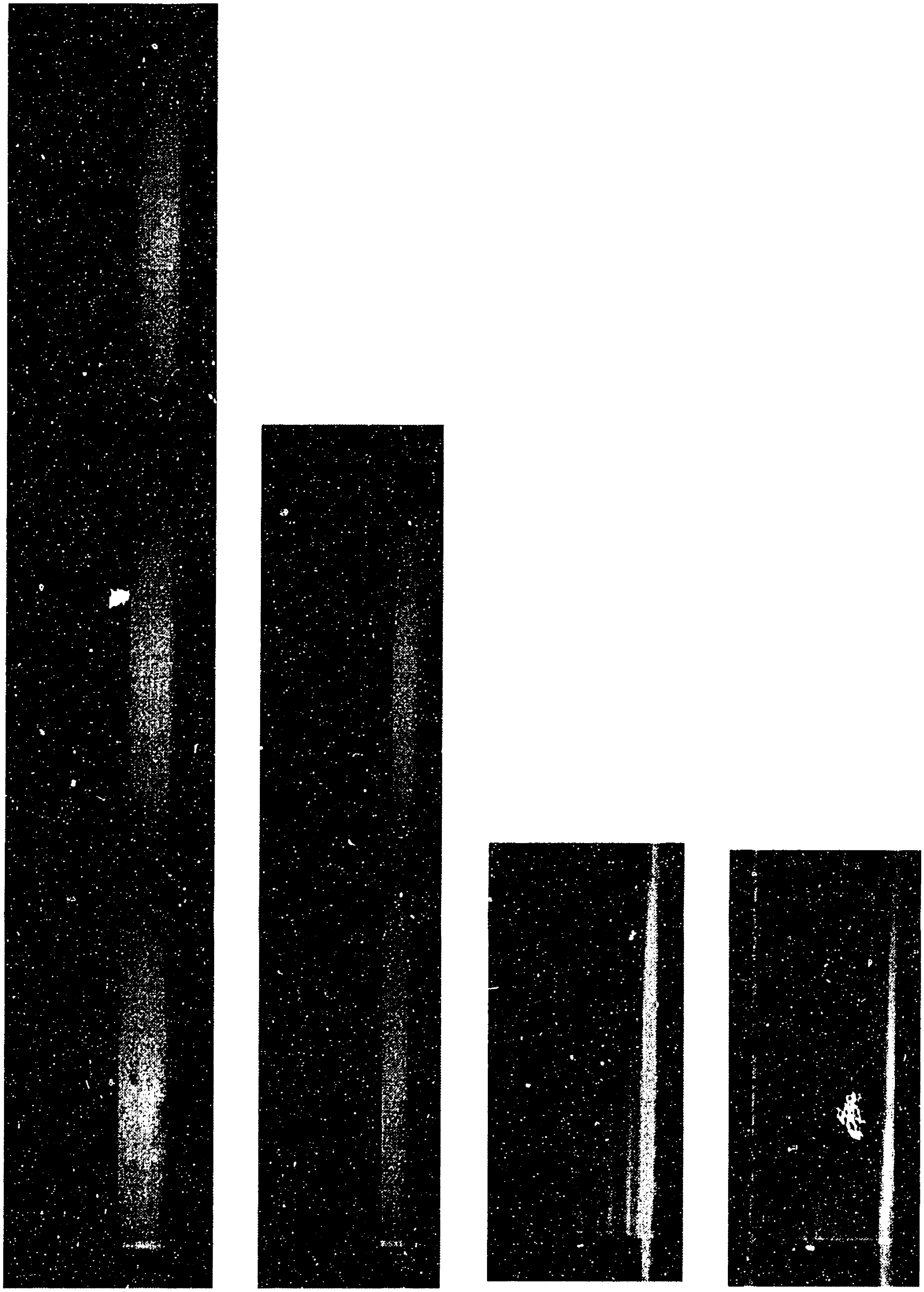

a)1:10 b) 1:5 c) 1:2 d) 1:1

Figure 4-22: Fluorescence images at different mixing ratios

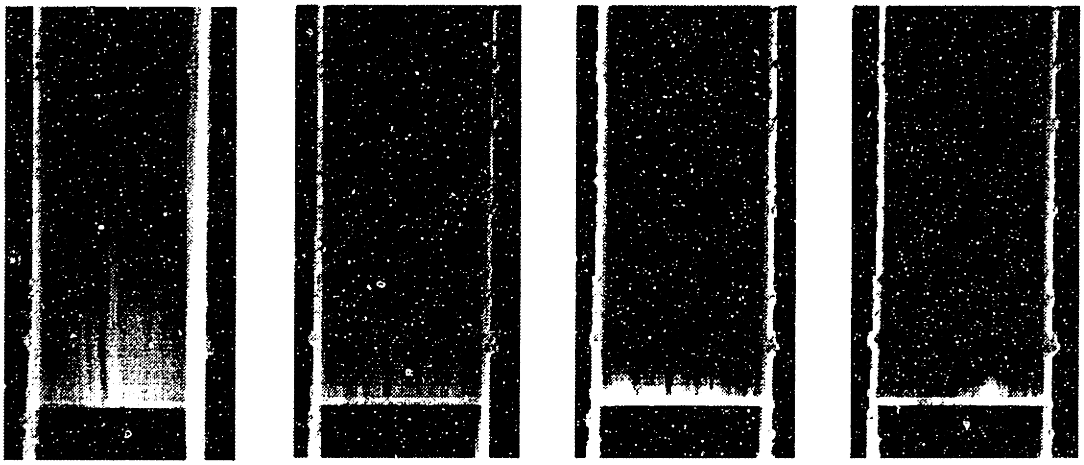

a) 1:1 b) 2:1 c) 5:1 d) 10:1

Figure 4-23: Fluorescence images at different mixing ratios

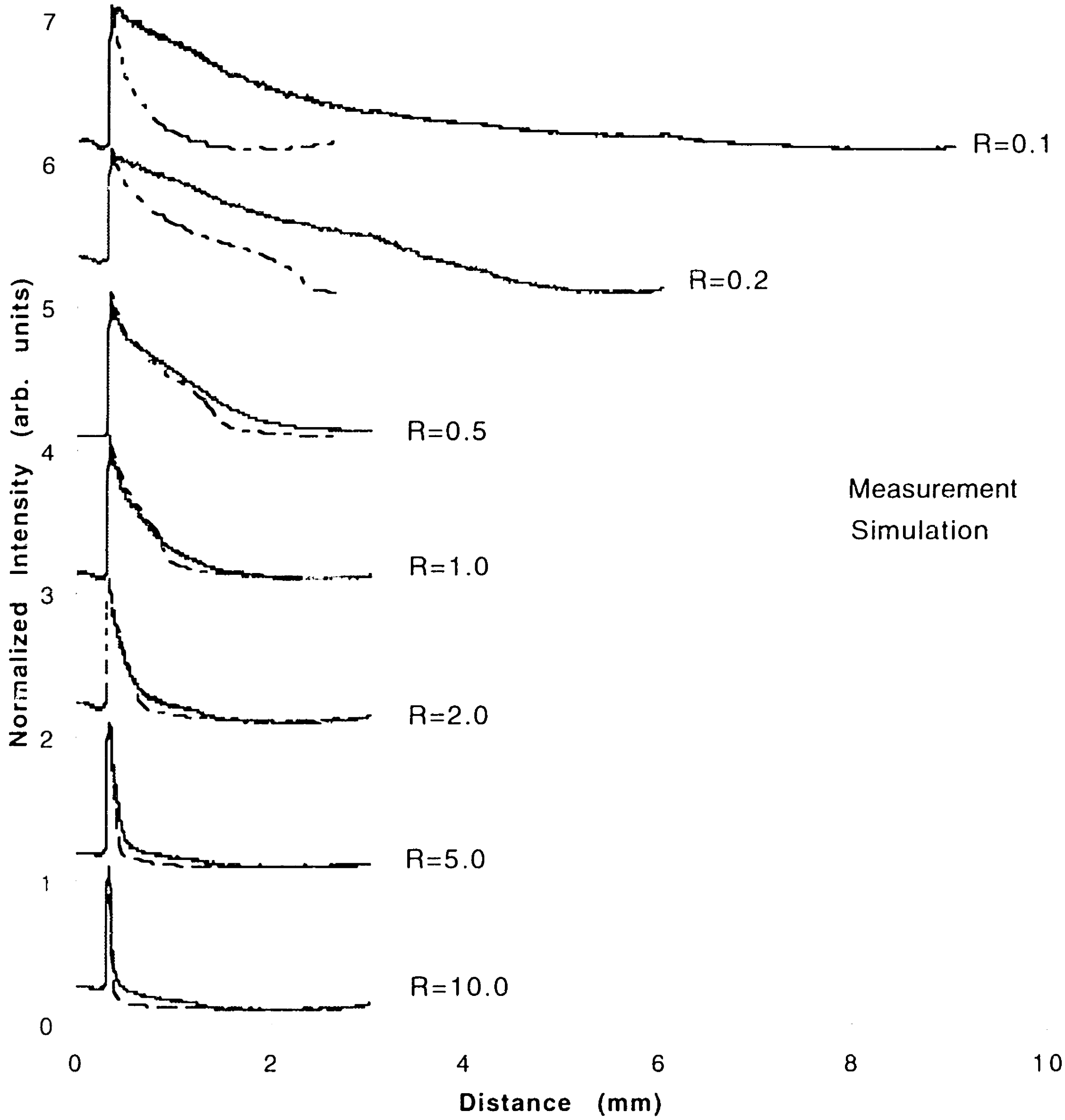

Figure 4-24: Fluorescence intensity profiles for different mixing ratios

Chapter 5

Conclusions

The main achievement of this work was the development of a device capable of handling and mixing small volume of liquids. While the device as-is suffers from several problems (to be discussed shortly), there were achievements made on several fronts.

In the process development area, the first achievement was that a chemomechanical polish process was developed that could smooth etched-silicon surfaces to a quality high enough to anodically bond to. This should allow for less reliance on SOI technology and polishing services to thin-back wafers. Second, a glass-channel etching methodology was developed that should allow for the etching of deep channels in glass with smooth sidewalls. Future work in this area would include the use of alternative masks (polySi and aSi) and optimizing the cleaning process to ensure a highly adherent mask.

This thesis also reported on the first microfabricated liquid mixer using a cantilever-plate flapper valve to achieve non-continuous mixing. The device was capable of handling the liquids of interest without failing. The liquid mixer did possess several shortcomings, however. First, there was much fluid leakage out of the sides of the cantilever plate, instead of the end. Second, the flapper valve did not seal well at the pressures and flowrates of interest. Third, the liquid mixer did not operate well at the flowrates of interest; the cantilever plate did not bend adequately.

To counteract these problems in future implementations, several areas need to be redesigned. The most important redesign would be to make the cantilever plate more flexible, so that it operated well at the pressures of interest. Second, the channel resistance could be increased to create a larger pressure drop, which would make measurement easier and would actuate the cantilever plate better.

A second major area of redesign would be to incorporate more packaging function into the liquid mixer chip. This could be done by micromachining channels for the syringe needles directly into the chip, reducing the packaging complexity, the latent fluid volume, and the size of the chip. Also, the channels could be formed in a polymer such as poly (dimethyl siloxane) (PDMS). This would allow for more vertical channel sidewalls (because of the cast method with which they are produced) and would remove the anodic bond, as PDMS sticks well to silicon. In addition, a PDMS gasket could be produced to attach the chip to the attachment block, removing the necessity for adhesive which tends to disrupt the flow.

Other areas of redesign include fabricating the valve seat on the bottom of the cantilever-plate, instead of on the handle wafer. This would be done with an aligned fusion bond. An alternative glass method would be to etch the channels with a deep reactive-ion etcher (RIE) in a silicon wafer which would be thinned and bonded to the handle wafer. A glass channel would be anodically bonded on top of this. This would allow for more rectangular channels and eliminate the difficult (and weakening) glass etch. Finally, the valve could be fabricated vertically instead of horizontally, using deep RIE.

In terms of packaging and testing, a fluorescence testing method was developed which used the pH dependence of a fluorescent dye to allow the studying of mixing in two fluids. This could be supplemented in the future with a confocal microscopy system to allow for cross-sectional imaging of the fluid streams

Appendix A

Detailed Process Flow

The following is the process flow used to fabricate the liquid mixer. The **Wafer** column refers to the material being processed in that step, be it the handle wafer (H), the device wafer (D), the bonded pair (B), or the glass wafer (G). The **Lab** refers to the laboratory where the step is performed.

Wafer	Step	Lab	Process Step
H	1	TRL	Piranha clean, 10 min 50:1 HF dip, 15 sec
H	2	TRL	HMDS Coat PR - standard recipe (0.5 krpm coat, 0.75 krpm spread, 4.0 krpm spin) Prebake - 30 min, 90 C Align and Expose - KarlSeuss1, 1.5 sec exposure (Mask DP) Develop - OCG934 3:2 developer, 90 sec Postbake - 30 min, 120 C
H	3	ICL	Descum, 3 min - in asher BOE dip, 15 sec - to clear native oxide Etch 1.2 um Si - Etcher 1, Recipe 19 (SF_6/CCl_4), P=50W
H	4	ICL	Piranha strip resist, 10 min 50:1 HF dip, 15 sec

H	5	TRL	HMDS Coat PR - standard recipe Prebake - 5 min, 90 C Coat PR - standard recipe (2nd coat) Prebake - 30 min, 90 C Align and Expose - KarlSeuss1, 2.8 sec exposure (Mask VS) Develop - OCG934 1:1, 60 sec Postbake - 30 min, 120 C
H	6	ICL	Etch 3.8 um Si - Etcher 1, Recipe 19 (SF_6/CCl_4), P=100W
H	7	ICL	Piranha strip resist, 10 min + HF dip
H	8	ICL	Piranha clean, 10 min (2x) 50:1 HF dip, 15 sec (2x) Deposit nitride - 1500 A, VTR (Si-rich) or LPCVD (Tube A5, Recipe 410)
H	9	TRL	HMDS Coat PR - frontside, standard recipe Prebake - 10 min, 90 C Coat PR - backside, AZ5214 IR resist, standard recipe (2nd coat) Prebake - 30 min, 90 C Align and Expose - KarlSeuss1, backside, infrared alignment, 1.8 sec (Mask PRT) Postbake - 60 sec, 120 C on plate Expose - KarlSeuss1, backside, 60 sec flood exposure Develop - AZ422 MIF, 90 sec Postbake - 30 min, 120 C
H	10	ICL	Etch nitride - Etcher 1, Recipe 15 (SF_6), P=250W
H	11	ICL	BOE dip, 1 min
H	12	RGL	KOH etch - port holes, 1.5 L of 20% KOH at 90 C w/ surfactant

H	13	TRL	Post-KOH clean - Piranha clean, 15 min 3x dump rinse 50:1 HF dip, 1 min 3x dump rinse RCA clean
H	14	ICL	BOE dip, 15 sec - to clear oxynitride before nitride strip Strip nitride - H3PO4, 180 C, 40 min
H	15	ICL	BOE dip, 1 min
H	16	TRL	RCA clean
H+D = B	17	TRL	Bond wafers in ambient
B	18	ICL	Bond anneal - Tube A3, Recipe 224, 1100 C wet O2 to grow 1.1um oxide (2:20 min)
B	19	TRL	Coat edge of wafers with standard photoresist Postbake - 20 min, 120 C HF vapor etch - 49% HF, frontside, ~20 min, in beaker
B	20	RGL	Acetone/methanol/isopropanol - to strip resist
B	21	RGL	BOE dip - 15 sec KOH etch - thin SOI, 3 L of 20% KOH at 60 C w/ surfactant, use caranuba wax to protect backside
B	22	TRL	Post-KOH clean - Piranha clean, 15 min 3x dump rinse 50:1 HF dip, 1 min 3x dump rinse RCA clean
B	23	TRL	Strip oxide - BOE, 12 min

B	24	TRL	HMDS Coat PR - front, standard recipe (except 2.5 krpm spin) Prebake - 10 min, 90 C Coat PR - front, standard recipe (except 2.5 krpm spin) - 2nd coat Prebake - 30 min, 90 C Align and Expose - KarlSeuss1, infrared alignment, 2.8 sec exposure (Mask PLT) Develop - OCG934 1:1, 90 sec Postbake - 30 min, 120 C
B	25	ICL	Etch 10 um Si - Etcher 1, Recipe 19 (SF_6/CCl_4), P=100W
B	26	ICL	Ash - 60 min
B	27	ICL	BOE dip, 11 min - strip oxide from plates
G	28	RGL	Detergent clean - Alconox, 20 min, w/ ultrasonic
G	29	TRL	Piranha clean - 10 min 50:1 HF dip, 15 sec
G	30	TRL	UV ozone clean - 60 min
G	31	TRL	ebeam Cr - P=5e-7, 200A at 2 A/s ebeam Au - P=5e-7, 1000A at 5 A/s
G	32	TRL	HMDS - gold Coat PR - gold, front, standard recipe Prebake - gold, 30 min, 90 C Align and Expose - gold, KarlSeuss2, 2s expose 4s wait - repeat 16x (Mask GLS) Develop - gold, OCG934 3:2, 120 sec Postbake - gold, 30 min, 120 C
G	33	TRL	Aqua Regia (3:1 $HCl:HNO_3$), 25 sec - etch Au

G	34	TRL	CR7, 20 sec - etch Cr
G	35	TRL	Etch Glass - 660:140:200 H_2O:HNO_3:HF stirred (etch rate = ~0.8 um/min)
G	36	RGL	Acetone/methanol/isopropanol rinse - strip PR
G	37	RGL	Aqua Regia (3:1 HCl:HNO3), 10 sec - strip Au
G	38	RGL	CR7, 20 sec - strip Cr
G	39	RGL	DI rinse, 10 min
B	40	TRL	Piranha clean, 10 min, blow dry
G		TRL	Nanostrip clean, 15 min, blow dry
B+G	41	TRL	Align - KarlSeuss2 (w/ UV epoxy) or EV1
B+G	42	TRL	Anodic Bond - 400C, 600 V, P = 10 lbs, 7 min
B+G	43	other	Die saw

Appendix B

Derivation of Mixing Length

This section derives the concentration profile and mixing time used in Chapter 2. First, the assumptions used in the analysis are stated. Then the problem is stated, followed by its governing differential equation and the domain. Finally, the differential equation is solved using the initial condition and the boundary conditions.

For the analysis in this section the following assumptions are made. First, convection is neglected; transport and mixing occur only through diffusion. Second, dilute concentrations are assumed. This allows the neglection of center-of-mass changes in the diffusing species. Third, the curvature of the channel is neglected; a perfectly rectangular channel is assumed. Fourth, concentration variations along the width of the channel are neglected; the problem is assumed to be one-dimensional.

The problem is to find the concentration profile of a diffusing species in a rectangular domain given a starting concentration profile. For this problem, and with the assumptions stated above, the relevant differential equation involved is the one-dimensional time-dependent diffusion equation with a concentration independent diffusivity [90]. It is

$$\frac{\partial C(x,t)}{\partial t} = D\frac{\partial^2 C(x,t)}{\partial x^2} \tag{B.1}$$

where D is the diffusivity of the solute in the solvent and C is the concentration of the solute. The equation describes the situation in Figure B-1, where a given amount of solute (determined by the mixing ratio) is injected into the channel at time t=0 and diffuses into the sample at later times. The initial condition for this particular problem is the initial reagent concentration, given by

$$\begin{aligned} C &= C_0 \text{ for } 0 < x < d \\ C &= 0 \text{ for } d < x < h \end{aligned} \tag{B.2}$$

where d is the height of the reagent and h is the height of the channel. The boundary conditions for this problem are

$$\frac{\partial C}{\partial x} = 0 \text{ at } x = 0 \text{ and } x = h \tag{B.3}$$

which states that no solute goes past the walls of the channel.

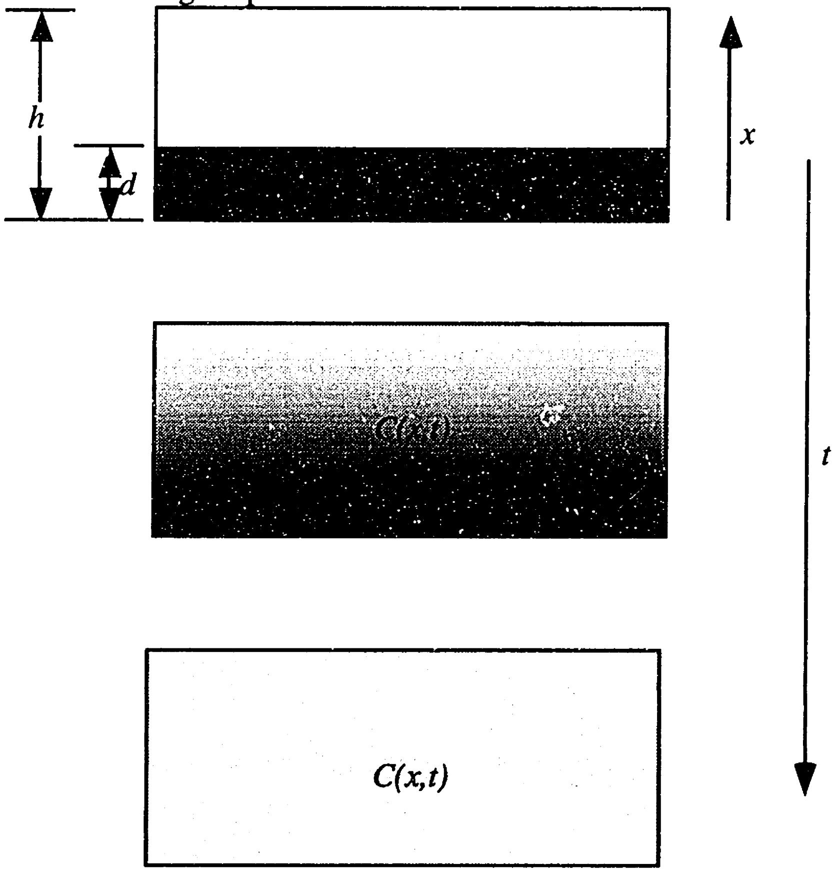

Figure B-1: Diffusion simulation

Equation B.1 can be solved by separation of variables. First, a solution is assumed of the form

$$\begin{aligned} C(x,t) &= X(x)T(t) \\ &= (A\sin\lambda x + B\cos\lambda x)e^{-\lambda^2 Dt} \end{aligned} \tag{B.4}$$

where the dependence on x and t. has been separated.

Next, the boundary conditions at time t=0 are imposed

$$\begin{aligned} \left.\frac{\partial C}{\partial x}\right|_{x=0} &= e^{-\lambda^2 Dt}(A\cos\lambda x - B\sin\lambda x) \\ &= e^{-\lambda^2 Dt}A \\ &= 0 \Rightarrow A = 0 \end{aligned} \tag{B.5}$$

$$\left.\frac{\partial C}{\partial x}\right|_{x=h} = e^{-\lambda^2 Dt} B\sin\lambda x$$

$$= e^{-\lambda^2 Dt} B\sin\lambda h \tag{B.6}$$

$$= 0 \Rightarrow \lambda h = n\pi \text{ or } \lambda = \frac{n\pi}{h} \text{ for } n = 1,2,3...$$

Now that A and λ have been determined, the concentration can be written as

$$C(x,t) = \sum_{n=1}^{\infty} B_n \cos(\frac{n\pi x}{h}) e^{-\left(\frac{n\pi}{h}\right)^2 Dt} \tag{B.7}$$

Next, the initial condition is used to find B_n

$$C_0 = \sum_{n=1}^{\infty} B_n \cos(\frac{n\pi x}{h}) \text{ for } 0 < x < d \text{ and } t = 0 \tag{B.8}$$

This is a Fourier cosine series. Taking the inverse transform gives

$$B_n = \frac{2}{h}\int_0^d C_0 \cos\left(\frac{n\pi x}{h}\right) dx$$

$$= \frac{2}{h} C_0 \sin\left(\frac{n\pi x}{h}\right)\Bigg|_0^d \left(\frac{h}{n\pi}\right) \tag{B.9}$$

$$= \frac{2}{n\pi} C_0 \sin\left(\frac{n\pi d}{h}\right) \text{ for } n = 1,2,3,...$$

Therefore, the concentration is

$$C(x,t) = \sum_{n=1}^{\infty} \frac{2}{n\pi} C_0 \sin\left(\frac{n\pi d}{h}\right) \cos\left(\frac{n\pi x}{h}\right) e^{-\left(\frac{n\pi}{h}\right)^2 Dt} \tag{B.10}$$

To determine the mixing time, the time when the concentration difference across the channel is less than 1% needs to be determined. Since the reagent starts out in the region between *0* and *d*, the greatest difference will be at the ends of the channel, between x=o and $x=h$. Mathematically, this means

$$\begin{aligned}\Delta C_{\max} &= C(0,t) - C(h,t)\\ &= \sum_{n=1}^{\infty} \frac{2}{n\pi} C_0 \sin\left(\frac{n\pi d}{h}\right) e^{-\left(\frac{n\pi}{h}\right)^2 Dt} \left[1 - \cos(n\pi)\right]\\ &= \sum_{n=1}^{\infty} \frac{2}{n\pi} C_0 \sin\left(\frac{n\pi d}{h}\right) e^{-\left(\frac{n\pi}{h}\right)^2 Dt} \left[1 - (-1)^n\right]\\ &= \sum_{n=1,3,5}^{\infty} \frac{4}{n\pi} C_0 \sin\left(\frac{n\pi d}{h}\right) e^{-\left(\frac{n\pi}{h}\right)^2 Dt}\end{aligned} \tag{B.11}$$

where use is made of an identity in the second equation and where it is realized that the elements of the sum in the third equation are nonzero only for odd *n*.

The terms in the sum of equation B.11 decrease rapidly with increasing *n* and *t*. Thus, for large times only the first term is needed. Therefore

$$\Delta C_{\max} \approx \frac{4}{\pi} C_0 \sin\left(\frac{\pi d}{h}\right) e^{-\left(\frac{\pi}{h}\right)^2 Dt} \tag{B.12}$$

Setting Δc_{max}=0.01 (for 99% mixing) and solving for the time gives

$$T_m \approx \frac{h^2}{\pi^2 D} \ln\left[\frac{400}{\pi} C_0 \sin\left(\frac{\pi d}{h}\right)\right] \tag{B.13}$$

where T_m is the mixing time.

It is important to note that this is smaller than the standard “decaying pulse” approximation for the mixing time, which is

$$T_m = \frac{h^2}{D} \tag{B.14}$$

Thus, the finite boundaries decrease the mixing time.

Appendix C

FIDAP Simulations

This appendix details the FIDAP simulations used to verify the integrity of the pressure measurement scheme. The issue is whether vorticity shedding in the T-adapter where the pressure transducer is housed is contributing to a velocity-dependent pressure error. A diagram of the T-adapter is shown in Figure C-1. To model the vorticity, the commercial computation fluid dynamics package FIDAP (Fluid Dynamics International) is used. A two dimensional approximation to the problem is used to simplify the simulation. As will be shown later, the pressure sensor error is so small that the simplification of using a 2-dimensional model can neglected.

Using FIDAP, 2-dimensional non-linear analyses of the Navier-Stokes equations are performed, with boundary conditions of no flow out the bottom of the T and no-slip on the walls. Figure C-2 and Figure C-3 show the velocity contour and Reynolds number contour plot for a flow rate of 100 µl/min. The contour plots for the other simulated flow rates have the same shapes as these, except that the scales are different. All the numbers on the plot should have a period before the first digit; a value of 1205E-03 is actually 0.1205E-03. The simulations show that Reynolds numbers and speeds of the flow scale linearly with the flow rate, which is to be expected. But, even though the Reynolds number and velocities are small, vortices are still being shed at the middle of T, as seen in Figure C-4 which is for a flow rate of 5 µl/min. The magnitude of the vorticities is small, but scales with the flow rate.

By plotting the pressure in the T-adapter and taking the difference between the pressure at the bottom of the T-adapter (where the pressure sensor is) and the middle of the T adapter (where the flow is), the relative pressure error at a given flowrate can be determined. The simulations show that this error is linear in flowrate and is less than 0.1% for flowrates less than 50 µl/min.

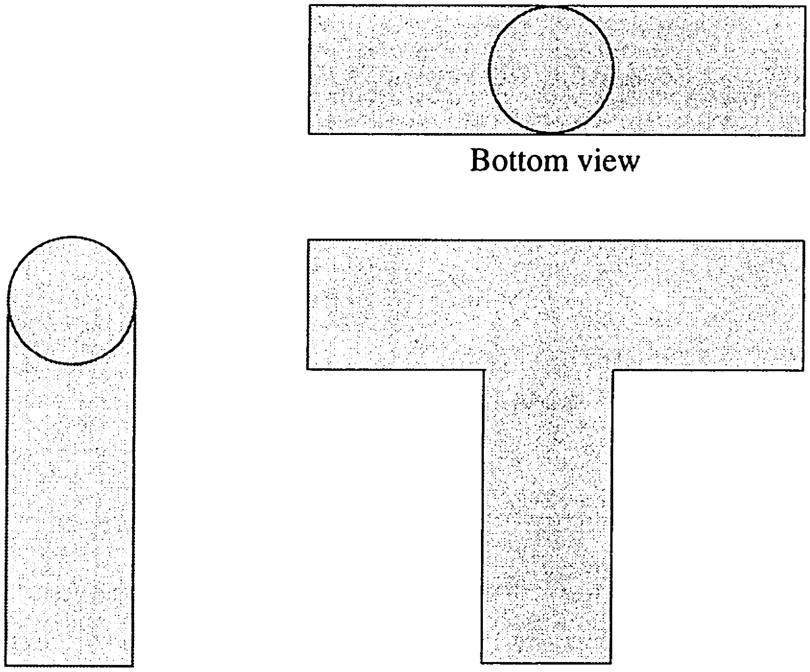

Figure C-1: T-adapter

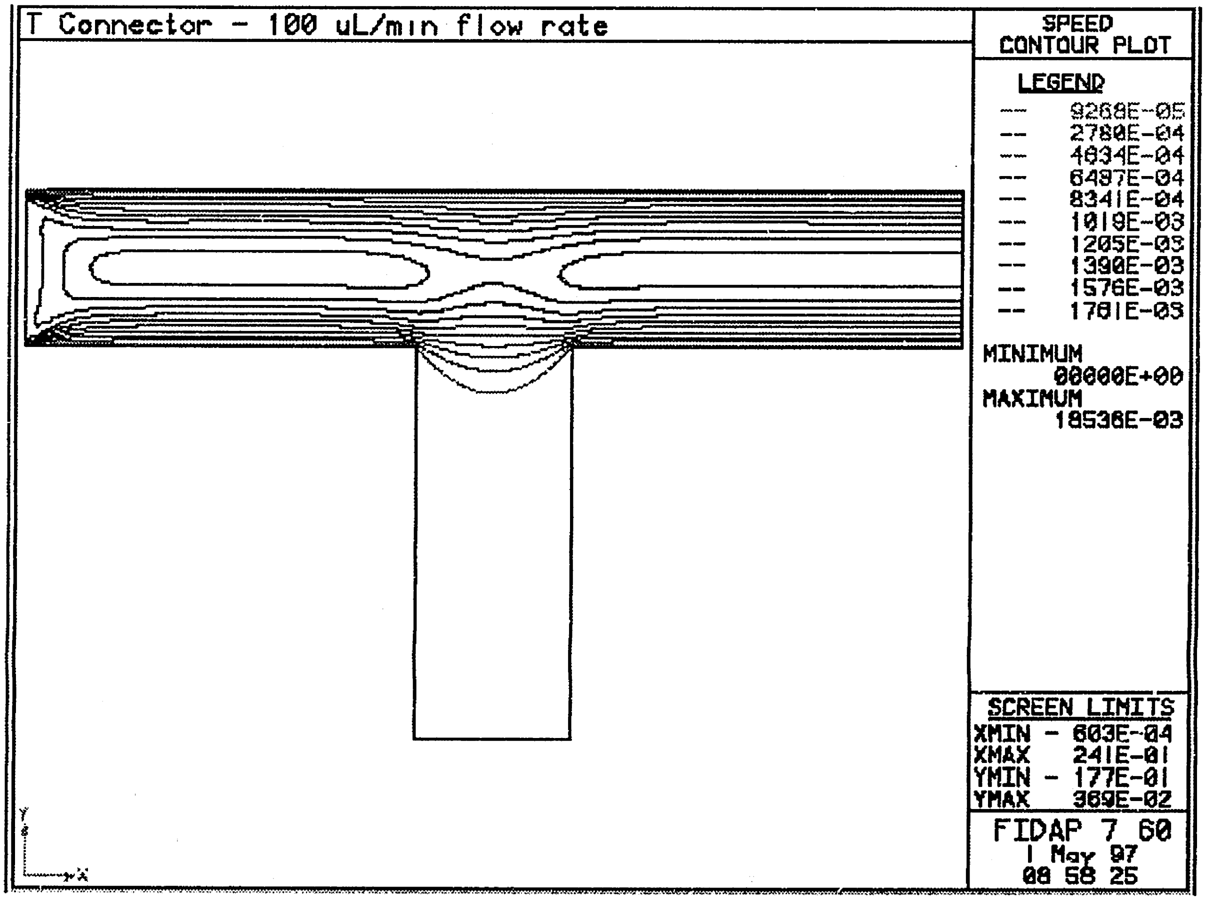

Figure C-2: Velocity contour plot

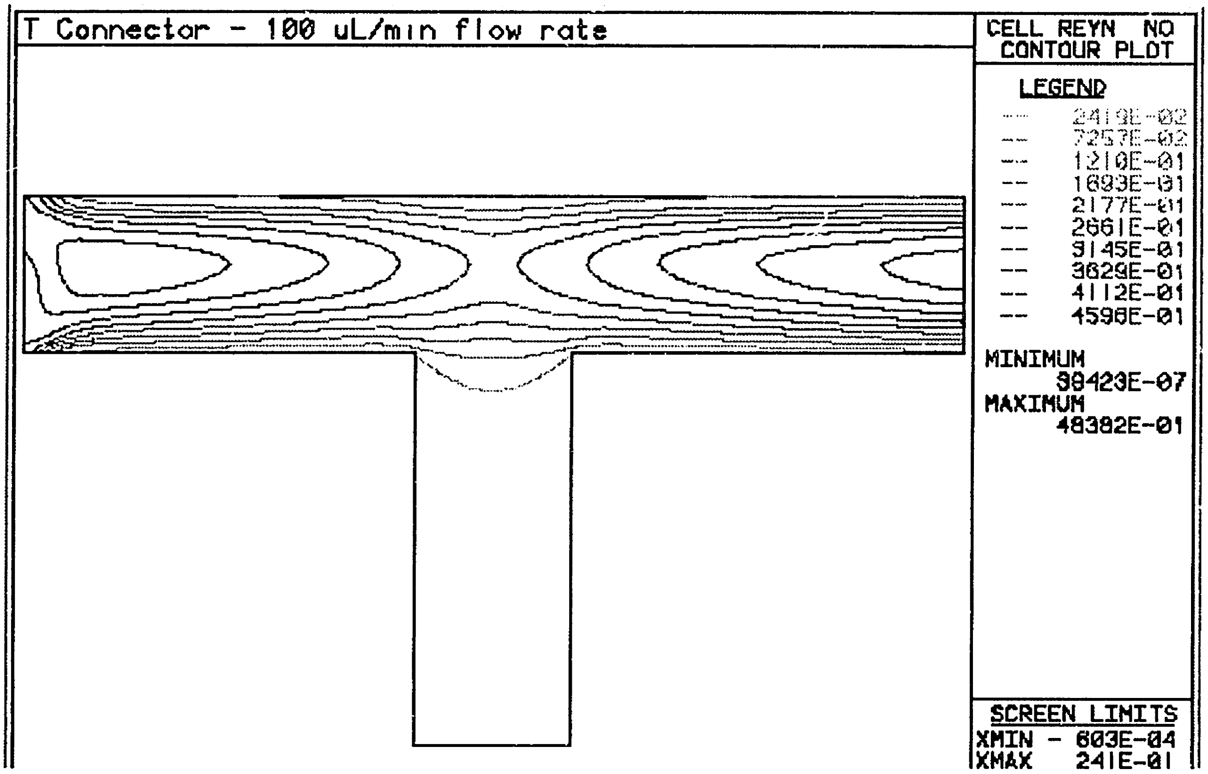

Figure C-3: Reynolds number contour plot

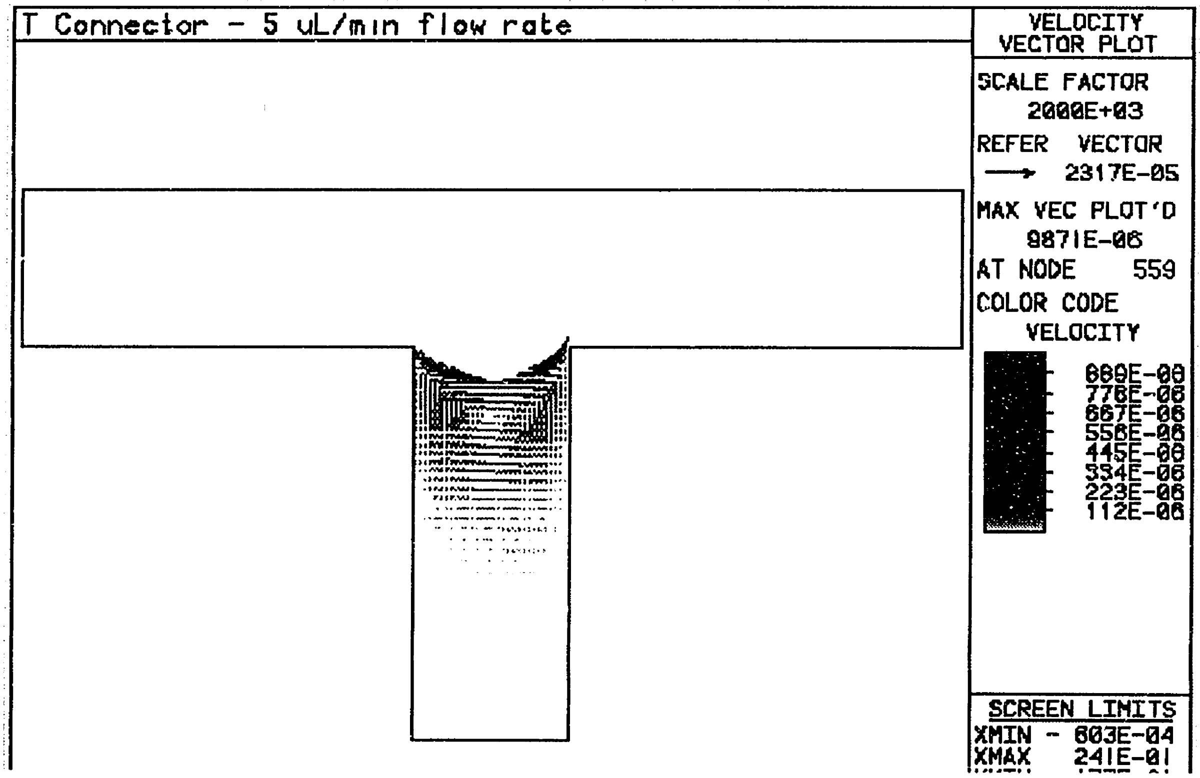

Figure C-4: Velocity vector plot

References

[1] W. D. Frobenius, A. C. Sanderson, H. C. Nathanson, "A microminiature solid state capacitive blood pressure transducer with improved sensitivity," *IEEE Transactions on Biomedical Engineering*, BME-20, pp. 312-314, 1973.

[2] L. Bousse, R. J. McReynolds, G. Kirk, T. Dawes, P. Lam, W. R. Bemiss, J. W. Parce," Micromachined Multichannel Systems for the Measurement of Cellular Metabolism," *Transducers '93 - 7th International Conference on Solid-State Sensors and Actuators*, pp. 916-919, 1993.

[3] M. A. Northrup, M. T. Ching, R. M. White, R. T. Watson, "DNA Amplification with a Microfabricated Reaction Chamber," *Transducers '93 - 7th International Conference on Solid-State Sensors and Actuators*, pp. 924-926, 1993.

[4] H. Shapiro, *Practical Flow Cytometry*, New York: Wiley-Liss, 1995.

[5] S. H. Ip, C. W. Ritterhaus, K. W. Healey, C. C. Struzziero, R. A. Hoffman, P. W. Hansen, "Rapid Enumeration of T Lymphocytes by a Flow-Cytometric Immunofluorescence Method," *Clinical Chemistry*, vol. 28, pp. 1905-1909, 1982.

[6] L. W. M. M. Terstappen, H. Meiners, M. R. Loken, "A rapid sample preparation technique for flow cytometric analysis of immunofluorescence allowing absolute enumeration of cell subpopulations," *Journal of Immunological Methods*, vol. 123, pp. 103-112, 1989.

[7] H. Ohki, R. Miyake, I. Yamazaki, T. Kaneko, "Flow Chambers with Low Pressure Loss," *Proceedings of the 2nd International Symposium on Fluid Control, Measurement Mechanics, and Flow Visualization*, pp. 245-249, 1988.

[8] H. Ohki, R. Miyake, I. Yamazaki, R. Yabe, "Three-Dimensional Flow Characteristics of Micro Flow Chamber," *Proceedings of the 3rd International Symposium on Fluid Control, Measurement, and Visualization*, pp. 125-129, 1991.

[9] R. Miyake, H. Ohki, I. Yamazaki, R. Yabe, " A Development of Micro Sheath Flow Chamber," *Proceedings of the IEEE Workshop on Micro Electro Mechanical Systems*, pp. 259-264, 1991.

[10] D. Sobek, A. M. Young, M. L. Gray, S. D. Senturia, "A Microfabricated Flow Chamber for Optical Measurements in Fluids," *Proceedings of the IEEE Workshop on Micro Electro Mechanical Systems*, pp. 219-224, 1993

[11] D. Sobek, S. D. Senturia, M. L. Gray, "Microfabricated Fused Silica Flow Chambers for Flow Cytometry," in *Proceedings of the IEEE Solid-State Sensor and Actuator Workshop*, pp. 260-263, 1994.

[12] D. Sobek, *Microfabricated Fused Silica Flow Chambers for Flow Cytometry*, Ph.D. thesis, Massachusetts Institute of Technology, 1996.

[13] D. A. Finney, L. A. Sklar, "Ligand/Receptor Internalization: A Kinetic, Flow Cytometric Analysis of the Internalization of N-Formyl Peptides by Human Neutrophils," *Cytometry*, vol. 4, pp. 54-60, 1983.

[14] G. M. Omann, W. Coppersmith, D. A. Finney, L. A. Sklar, " A Convenient On-Line Device for Reagent Addition, Sample Mixing, and Temperature Control of Cell Suspensions in Flow Cytometry," *Cytometry*, vol. 6, pp. 69-73, 1985.

[15] A. Pennings, P. Speth, H. Wesels, C. Haanen, "Improved Flow Cytometry of Cellular DNA and RNA by On-Line Reagent Addition," *Cytometry*, vol. 8, pp. 335-338, 1987.

[16] K. Kelley, "Sample Station Modification Providing On-Line Reagent Addition and Reduced Sample Transit Time for Flow Cytometers," *Cytometry*, vol. 10, pp. 796-800, 1989.

[17] K. Kelley, "Very Early Detection of Changes Associated with Cellular Activation Using a Modified Flow Cytometer," *Cytometry*, vol. 12, pp. 464-468, 1991.

[18] J. F. Dunne, "Time Window Analysis and Sorting," *Cytometry*, vol. 12, pp. 597-601, 1991.

[19] W. Lindberg, J. Ruzicka, G. D. Christian, "Flow Injection Cytometry: A New Approach for Sample and Solution Handling in Flow Cytometry," *Cytometry*, vol. 14, pp. 230-236, 1993.

[20] W. Lindberg, L. D. Scampavia, J. Ruzicka, G. D. Christian, "Fast Kinetic Measurements and On-Line Dilution by Flow Injection Cytometry," *Cytometrty*, vol. 16, pp. 324-330. 1994.

[21] L. D. Scampavia, G. Blankenstein, J. Ruzicka, G. D. Christian, " A Coaxial Jet Mixer for Rapid Kinetic Analysis in Flow Injection and Flow Injection Cytometry," *Analytical Chemistry*, vol. 67, pp. 2743-2749, 1995.

[22] A. Manz, "Miniaturized Chemical Analysis Systems Based on Electroosmotic Flow," *Proceedings of IEEE Workshop on Micro Electro Mechanical Systems*, pp. 14-18, 1997.

[23] A. Manz, J. C. Fettinger, E. Verpoorte, H. Lüdi, H. M. Widmer, D. J. Harrison, "Micromachining of monocrystalline silicon and glass for chemical analysis systems," *Trends in Analytical Chemistry*, vol. 10, no. 5, pp. 144-148, 1991.

[24] D. J. Harrison, A. Manz, P. G. Glavina, "Electroosmotic Pumping Within a Chemica Sensor Integrated on Silicon," *Transducers '91 - 6th International Conference on Solid-State Sensors and Actuators*, pp. 792-795, 1991.

[25] A. Manz, D. J. Harrison, J. C. Fettinger, E. Verpoorte, H. Lüdi, H. M. Widmer, "Integrated Electroosmotic Pumps and Flow Manifolds for Total Chemical Analysis Systems," *Transducers '91 - 6th International Conference on Solid-State Sensors and Actuators*, pp. 939-941, 1991.

[26] D. J. Harrison, A. Manz, Z. Fan, H. Lüdi, H. M. Widmer, "Capillary Electrophoresis and Sample Injection Systems Inegrated on a Planar Glass Chip," *Analytial Chemistry*, vol. 64, pp. 1926-1932, 1992.

[27] D. J. Harrison, P. G. Glavina, A. Manz, "Towards miniaturized electrophoresis and chemical analysis systems on silicon: an alternative to chemical sensors," *Sensors and Actuators B*, vol. 10, pp107-116, 1993.

[28] Z. Fan, D. J. Harrison, "Micromachining of Capillary Electrophoresis Injectors and Separators on Glass Chips and Evaluation of Flow at Capillary Intersections," *Analytical Chemistry*, vol. 66, pp. 177-184, 1994.

---

[29] D. J. Harrison, K. Fluri, N Chiem, T. Tang, Z. Fan, "Micromachining Chemical and Biochemical Analysis and Reaction Systems on Glass Substrates," *Transducers '95 - 8th International Conference on Solid-State Sensors and Actuators*, pp. 752-755, 1995.

[30] D. J. Harrison, N Chem, "Immunoassay Flow Systems On-Chip," *IEEE Solid-State Sensor and Actuator Workshop*, pp. 5-8, 1996.

[31] Z. Liang, N. Chiem, G. Ocvirk, T. Tang, K. Fluri, D. J. Harrison, "Microfabrication of a Planar Absorbance and Fluorescence Cell for Integrated Capillary Electrophoresis Devices," *Analytical Chemistry*, vol. 68, pp. 1040-1046, 1996.

[32] D. E. Rayomond, A. Manz, H. M. Widmer, "Continuous Sample Preparation using Free-Flow Eelctrophoresis on a Silicon Microstructure," *Transducers '95 - 8th International Conference on Solid-State Sensors and Actuators*, pp. 760-763, 1995.

[33] E. Verpoorte, A. Manz, H. M. Widmer, B. van der Schoot, N. F. de Rooij, "A Three-Dimensional Micro Flow System for a Multi-Step Chemical Analysis," *Transducers '93 - 7th International Conference on Solid-State Sensors and Actuators*, pp. 939-942, 1993.

[34] M. A. Northrup, C. Gonzalez, D. Hadley, R. F. Hills, P. Landre, S. Lehew, R. Saiki, J. J. Sninksy, R. Watson, R. Watson Jr., "A MEMS-Based Miniature DNA Analysis System," *Transducers '95 - 8th International Conference on Solid-State Sensors and Actuators*, pp. 764-767, 1995.

[35] R. Miyake, K. Tsuzuki, T. Takagi, K. Imai, "A Highly Sensitive and Small Flow-Type Chemical Analysis System with Integrated Absorptiometric Micro-Flow Cell," *Proceedings of IEEE Workshop on Micro Electro Mechanical Systems*, pp. 102-107, 1997.

[36] R. Miyake, T. S. J. Lammerink, M. Elwenspoek, J. H. J. Fluitman, "Micro Mixer with Fast Diffusion," *Transducers '93 - 7th International Conference on Solid-State Sensors and Actuators*, pp. 248-253, 1993.

[37] N. Schwesinger, T. Frank, H. Wurmus, "A modular microfluid system with an integrated micromixer," *Journal of Micromechanics and Microengineering*, vol. 6, pp. 99-102, 1996.

[38] J. Branebjerg, P. Gravesen, J. P. Krog, C. R. Nielsen, "Fast Mixing by Lamination," *Proceedings of IEEE Workshop on Micro Electro Mechanical Systems*, pp. 441-446, 1996.

[39] J. Evans, D. Liepmann, A. P. Pisano, "Planar Laminar Mixer," *Proceedings of IEEE Workshop on Micro Electro Mechanical Systems*, pp. 96-101, 1997.

[40] J. Tirén, L. Tenerz, G. Hök, "A batch-fabricated non-reverse valve with cantilever beam manufactured by micromachining of silicon," *Sensors and Actuators*, vol. 18, pp. 389-396, 1989.

[41] T. Ohnstein, T. Fukiura, J. Ridley, U. Bonne, "Micromachined Silicon Microvalve," *Proceedings of IEEE Workshop on Micro Electro Mechanical Systems*, pp. 95-98, 1990.

[42] A. Emmer, M. Jansson, J. Roeraade, U. Lindberg, B. Hök, "Fabrication and characterization of a silicon microvalve," *Journal of Microcolumn Separations*, vol. 4, pp. 13-15, 1992.

---

[43] J. Ulrich, H. Füller, R. Zengerle, "Static and Dynamic Flow Simulations of a KOH-Etched Micro Valve," *Transducers '95 - 8th International Conference on Solid-State Sensors and Actuators*, pp. 17-20, 1995

[44] M. Koch, A. G. R. Evans, A. Brunnschweiler, "Coupled FEM simulation for the characterization of the fluid flow within a micromachined cantilever valve," *Journal of Micromechanics and Microengineering*, vol. 6, pp. 112-114, 1996.

[45] J. Ulrich, R. Zengerle, "Static and dynamic flow simulation of a KOH-etched microvalve using the finite-element method," *Sensors and Actuators A*, vol. 53, pp. 379-385, 1996.

[46] A. L. Landay, K. A. Muirehead, "Procedural Guidelines for Performing Immunophenotyping by Flow Cytometry," *Clinical Immunology and Immunopathology*, vol. 52, pp. 48-60, 1989.

[47] M. M. Denn, *Process Fluid Mechanics*. Englewood Cliffs, New Jersey: Prentice-Hall, Inc., 1980.

[48] W. A. Nash, "Several Approximate Analyses of the Bending of a Rectangular Cantilever Plate by Uniform Normal Pressure," *Journal of Applied Mechanics*, vol. 74, pp. 33-36, 1952.

[49] F. V. Rohde, "Large Deflections of a Cantilever Beam with Uniformly Distributed Load," *Quarterly of Applied Mathematics*, vol. 11, pp. 337-338, 1953.

[50] A. E. Seames, H. D. Conway, "A Numerical Procedure for Calculating the Large Deflections of Straight and Curved Beams," *Journal of Applied Mechanics*, vol. 79, pp. 289-294, 1957.

[51] R. B. Hopkins, *Design Analysis of Shafts and Beams (A Practical Approach), 2nd Edition*. Malabar, Florida: Robert E. Krieger Publishing Company, 1987.

[52] F. R. Archibald, "Load Capacity and Time Relations for Squeeze Films," *Transactions of the ASME*, vol. 78, pp. A-231-245, 1956.

[53] P. Gravesen, J. Branebjerg, O. S. Jensen, "Microfluidics - a review," *Journal of Micromechanics and Microengineering*, vol. 3, pp. 168-182, 1993.

[54] I. Ali, S. R. Roy, G. Shim, "Chemical-mechanical polishing of interlayer dielectric: A review," *Solid State Technology*, Oct., pp. 63-70, 1994.

[55] H. Fusstetter, A. Schnegg, D. Gräf, H. Kirshner, M. Brohl, P. Wagner, "Impact of Chemomechanical Polishing on the Chemical Composition and Morphology of the Silicon Surface," *Materials Research Society Symposium Proceedings*, vol. 386, pp. 97-108, 1995.

[56] Semiconductor Processing Company, 12 Channel St. Boston, MA 02210.

[57] H. Seidel, L. Csepregi, A. Heuberger, H. Baumgärtel, "Anisotropic Etching of Crystalline Silicon in Alkaline Solutions, I. Orientation Dependence and Behaviour of Passivation Layers," *Journal of the Electrochemical Society*, vol. 137, pp. 3612-3626, 1990.

[58] M. Spak, D. Mammato, S. Jain, D. Durham, "Mechanism and Lithographic Evaluation of Image Reversal in AZ® 5214 Photoresist," *Seventh International Conference on Photopolymers*, Ellenville, NY.

[59] L. Ristic, *Sensor Technology and Devices*, Norwood, MA: Artech House, 1994.

[60] H. Robbins, B. Schwartz, "Chemical Etching of Silicon, II. The System HF, HNO_3, H_2O, and $HC_2H_3O_2$," *Journal of the Electrochemicl Society*, vol. 107, pp. 108-111, 1960.

[61] B. Schwartz, H. Robbins, "Chemical Etching of Silicon, III. A Temperature Study in the Acid System," *Journal of the Electrochemical Society*, vol. 108, pp.365-372, 1961.

[62] Mooney Precision Glass Company, 4300 Terrace Avenue, Huntington WV, 25705.

[63] D. R. Uhlmann, A. G. Kolbeck, "Phase separation and the revolution in concepts of glass structure," *Physics and Chemistry of Glasses*, vol. 17, pp. 146-158, 1976.

[64] V. J. Brzozowski, C. T. Brooks, "Ceramics, glasses and diamonds," in *Electronic Materials and Processes Handbook*, C. A. Harper, R. N. Sampson, Eds. New York: McGraw-Hill, Inc., 1994, pp. 3.19-3.46.

[65] D. C. Boyd, D. A. Thompson, "Glass," in *Kirk-Othmer: Encyclopedia of Chemical Technology, Volume 11, Third Edition*, New York: John Wiley, pp. 807-880, 1980.

[66] G. R. Cokelet, R. Soave, G. Pugh, L. Rathbun, "Fabrication of *in Vitro* Microvascular Blood Flow Systems by Photolithography," *Microvascular Research*, vol. 46, pp. 394-400, 1993.

[67] P. B. Adams, "Bibliography on Clean Glass," *Journal of Testing and Evaluation*, vol. 5, pp. 53-57, 1977.

[68] D. E. Campbell, P. B. Adams, "Bibliography on Clean Glass: Supplement I," *Journal of Testing and Evaluation*, vol. 14, pp. 260-265, 1986.

[69] M. L. Hair, "The Nature of Leached Glass Surfaces," in *Clean Surfaces: Their Preparation and Characterization for Interfacial Studies*, G. Goldfinger, Ed. New York: Marcel Dekker, 1970, pp. 269-284.

[70] L. Holland, *The Properties of Glass Surfaces*, London: Chapman and Hall, 1964, chap. 5.

[71] J-C. Liu, R. J. Mattauch, "Plasma Etching of Borosilicate Glass," *Conference Proceedings of IEEE SOUTHEASTCON 84*, pp. 13-16, 1984.

[72] Y. Kuo, J. R. Crowe, " Reactive Ion Etching of a Multicomponent Glass Substrate," *Proceedings of SPIE Advanced Processing of Semiconductor Devices II*, vol. 945, pp. 103-110, 1988.

[73] Y. Kuo, J. R. Crowe, "Factors Affecting Reactive Ion Etching of Corning 7059 Glass," *Proceedings of SPIE Monitoring and Control of Plasma-Enhanced Processing of Semiconductors*, vol. 1037, pp. 103-107, 1988.

[74] G. A. C. M. Spierings, "Review: Wet chemical etching of silicate glasses in hydrofluoric acid based solutions," *Journal of Materials Science*, vol. 28, pp. 6261-6273, 1993.

[75] W. Kern, C. A. Deckert, "Chemical Etching," in *Thin Film Processes*, J. L. Vossen, W. Kern, Eds. New York: Academic Press, pp.401-496, 1978.

[76] M. Tomozawa, T. Takamori, "Effect of Phase Separation on HF Etch Rate of Borosilicate Glasses," *Journal of the American Ceramic Soiciety*, vol. 60, pp. 301-304, 1977.

[77] G. Wallis, D. I. Pomerantz, "Field Assisted Glass-Metal Sealing," *Journal of Applied Physics*, vol. 40, pp. 3946-3949, 1969.

[78] T. Rogers, J. Kowal, "Selection of glass, anodic bonding conditions and material compatibility for silicon-glass capacitive sensors," *Sensors and Actuators A*, vol. 46-47, pp. 113-120, 1995.

[79] R. P. Denedict, *Fundamentals of Temperature, Pressure, and Flow Measurements*, New York: John Wiley, 1969.

[80] H. W. Coleman, W. G. Steele, *Experimentation and Uncertainty Analysis for Engineers*, New York: John Wiley, 1989.

[81] E. Gurr, *Encylcopaedia of Microscopic Stains*, Baltimore: Williams and Wilkins, 1961.

[82] R. D. Lillie, *H. J. Conn's Biological Stains, 8th Edition*, Baltimore: Williams and Wilkins, 1969.

[83] E. Gurr, *Synthetic Dyes in Biology, Medecine and Chemistry*, London: Academic Press, 1971.

[84] M. M. Martin, L. Lindqvist, "The pH Dependence of Fluorescein Fluorescence," *Journal of Luminescence*, vol .10, pp. 381-390, 1975.

[85] J. Yguerabide, E. Talavera, J. M. Alvarez, B. Quintero, "Steady-State Fluorescence Method for Evaluating Excited State Proton Reactions: Application to Fluorescein," *Photochemistry and Photobiology*, vol. 60, pp. 435-441, 1994.

[86] R. Sjöback, J. Nygren, M. Kubista, "Absorption and fluorescence properties of fluorescein," *Spectrochimica Acta Part A*, vol. 51, pp. L7-L21, 1995.

[87] M. M. Koochesfahani, P. E. Dimotakis, "Mixing and chemical reactions in a turbulent liquid mixing layer," *Journal of Fluid Mechanicsi*, vol. 170, pp. 83-112, 1986.

[88] D. A. Walker, "A fluorescence technique for measurement of concentration in mixing liquids," *Journal of Physics E*, vol. 20, pp. 217-224, 1987.

[89] J. A. Bellerose, C. B. Rogers, "Measuring Mixing and Local pH through Laser Induced Fluorescence," *Laser Anemometry - 1994, Advances and Applications*, FED-Vol. 191, pp. 217-220, 1994.

[90] E. L. Cussler, *Diffusion - Mass transfer in fluid systems*, Cambridge: Cambridge University Press, 1984.